CHARACTERIZATION OF COMPOSITIONAL VARIATION AND SOLIDIFICATION CONDITION ON RAPID SOLIDIFICATION BEHAVIOR OF BETA STABILIZED TITANIUM

by

CHRISTOPHER J. WILLIAMSON

DR. LUKE N. BREWER, COMMITTEE CHAIR
DR. LAURENTIU NASTAC
DR. MARK WEAVER
DR. ANDY DEAL
DR. ROBIN FOLEY

A DISSERTATION

Submitted in partial fulfillment of the requirements
for the degree of Doctor of Philosophy
in the Department of Engineering
in the Graduate School of
The University of Alabama

TUSCALOOSA, ALABAMA

2024

UUR
NSC-614-6252
June 2024

Copyright Christopher Jacob Williamson, 2024
ALL RIGHTS RESERVED

UUR
NSC-614-6252
June 2024

ABSTRACT

Rapid solidification (RS) is a field of study that has increased in importance due to the rise of additive manufacturing (AM) techniques. The breakdown of equilibrium at the solid-liquid interface results in an inability to use traditional solidification models that have been applied to great success in casting. As such, there is a current need for a high-throughput testing method to screen alloys at rapid solidification conditions without the significant cost for powder atomization. In this work, twin hammer splat quenching (SQ) is utilized and theoretically developed as a technique uniquely placed to test alloy systems for AM applications. Using analytical thermal spray models and numerical heat transfer simulations, the cooling rate and solidification conditions of splat quenching are compared across several parameters to evaluate the key parameters for generating cooling rates relevant to AM process. Once a framework for the cooling rates and relevancy of SQ are developed, SQ was used to process alloy compositions in the Ti-5553 alloy space (AMS 7026) to study the formation of detrimental secondary phases occurring upon rapid quenching from the melt. A martensitic phase is found to occur at the lower end of the standard, but the composition listed in the standard were found to be safe. Finally, the rapid solidification behavior of Ti-5553 is evaluated by comparing splat quenching, laser welding, and plasma atomization that offer a wide window of solidification conditions. The segregation and solidification structure are analyzed and compared to models to provide a deeper understanding of the solidification behavior of beta stabilized titanium alloys.

DEDICATION

This dissertation is dedicated to my wife, Mary, who has been with me as a constant source of love and encouragement. And to my parents who sacrificed for me to succeed and pushed me to heights I would not have achieved otherwise.

LIST OF ABBREVIATIONS AND SYMBOLS

Al_{eq}	Aluminum equivalency
AM	Additive Manufacturing
APT	Atom probe tomography
b	Burger's vector
BCC	Body centered cubic crystal structure
Bo	covalent bond order
c_0	Impact coefficient
C_0	Nominal composition
CALPHAD	CALculated PHAse Diagram
CET	Columnar to equiaxed transition
Cs	Composition of solid phase
d	Splat half thickness
DED	Directed energy deposition
D_i	Diffusional coefficient
EBAM	Electron beam additive manufacturing
EBSD	Electron back scatter diffraction
EDM	Electrical discharge machining
EDS	Energy dispersive spectroscopy
G	Thermal Gradient
h	Heat transfer coefficient
HCP	Hexagonal close packed crystal structure
IPF	Inverse pole figure
Iv(Pe)	Ivantsov function
k	Partition coefficient
k_e	Equilibrium partition coefficient
kw	Thermal conductivity
LPBF	Laser powder bed fusion
m	Liquidus slope
Md	average mean d-Orbital energy level
Moeq	Molybdenum equivalency
M_s	Martensitic start temperature
N_0	Nucleation sites
Pe	Peclet number

PREP	plasma rotating electrode process
QEDS	Quantitative energy dispersive spectroscopy
R	Solid-liquid perturbation size
Ra	Surface asperity
RS	Rapid solidification
S(θ)	Shape factor
SEM	Scanning electron microscopy
TEM	Transmission electron microscopy
TL	Liquidus temperature
Tm	Melting temperature
TRIP	TRansformation Induced Plasticity
Ts	Solidus temperature
V	Solidification velocity
v	Velocity of laser
V0	Platen velocity
Vd	Velocity diffusional limit
XRD	X-ray diffraction
α	Titanium HCP phase
α"	Orthorhombic martensite
β	Titanium BCC Phase
Γ	Gibbs-Thomson coefficient
δ	Interface width
ΔG_{het}	Gibbs energy to heterogeneously nucleate
ΔG_{homo}	Gibbs energy to homogeneously nucleate
ΔT_c	Compositional undercooling
ΔT_n	Nucleation undercooling
ρ	Density
σ	Surface tension
ω	Titanium omega phase
μ	Shear modulus

ACKNOWLEDGEMENTS

I would also like to express my gratitude to my advisor, Dr. Luke Brewer, for his guidance and support as I have grown as a researcher and scientist under his direction. I am also supremely thankful for the numerous other faculty members at the University of Alabama that have helped develop me through discussion and mentoring. Dr. Brian Jordon for providing me the opportunity to enter into his research group as an undergraduate and help develop an interest into the world of Material Science that has profoundly changed my life. Dr. Mark Weaver for his continued friendship, insight, and book recommendations throughout my entire career in graduate school. And only through the collective help and guidance of my entire committee is this dissertation possible.

Additionally, this research would not be possible without funding and support from Kansas City National Security Campus. Support from Ben Brown and Dr. Andy Deal has been instrumental in both my work in this dissertation as well as my growth as a material scientist. Finally, the culmination of work is only possible through the support of the many friends that I have had throughout graduate school including Dr. Ryan Kinser, Dr. Micheal Pavel, and Dr. Christopher Roper as well as technical support from the members of the Central Analytical Facility.

This work is funded by the Department of Energy's Kansas City National Security Campus, operated by Honeywell Federal Manufacturing & Technologies, LLC, under contract number DE-NA0002839.

UUR
NSC-614-6252
June 2024

CONTENTS

LIST OF TABLES

LIST OF FIGURES

CHAPTER 1 : INTRODUCTION

1.1.0 Motivation

Titanium alloys are a relatively new alloy system with the first commercial use of the material in the 1950s as the need for a high temperature structural alloy in aviation was unable to be met by other structural alloy systems such as aluminums or steels [1]. The buy to fly ratio, ratio of billet weight to finished component weight, for several aerospace components was reported to be in the range of 6-20:1 as such in the best case scenario over 73% of the material purchased is machined off with some components removing 95% of the initial mass of the billet [2]. In light of these difficulties, research has been ongoing for techniques that allow for the creation of complicated components that need the excellent properties of the titanium alloy systems but with minimal post-processing or material loss. Traditional casting of titanium has seen use due to the ability for techniques such as investment casting to create near-net shape components without the need for significant material waste [3]. The downside of these techniques is that the lower solidification rates can lead to excess segregation especially in beta stabilized allots and increased beta grain size as well as resulting in defects such as alpha case hardening and inclusions from the mold walls[4,5]. Investment casting also has difficulties with physical limitations of casting such as material flow into thin walls, controlling the titanium reaction with the mold material, and inhomogeneous microstructure due to varying cooling rates. The process can be highly usable for large or routinely created components, but the developing field of additive manufacturing offers the ability to rapidly create newly designed components

without significant development costs such as mold design as well as having solidification rates high enough to avoid the segregation concerns of slower solidifying processes.

Additive manufacturing (AM) is a class of manufacturing techniques that successively join material to create components. This additive building of components can be done by a melt based technique that use a heat source such as an electron beam or laser as well as solid-state by frictional mixing or impact [6]. Among these techniques the fusion-based techniques such as directed energy deposition (DED), laser beam powder bed (LPBF), and electron beam additive manufacturing (EBAM) have demonstrated significant promise due to reduction in material waste, near-net shaping capability, and flexibility to process a wide range of feedstock materials. In addition to the material saving benefits, AM techniques also allow for freeform designs that are unachievable by traditional processes[7]. Clearly with the potential to lower component waste and allow for advanced component designs, titanium alloys are an area of interest in AM research as a way to widen the use cases of the material system by the free form nature of the AM processes.

As AM of titanium becomes an increasing area of interest for commercial use, the lack of characterization and understanding of rapid solidification on the titanium material system are areas in need of address. The additive manufacturing of titanium has cooling rates of roughly 10^3 - 10^8 K/s in processes such as DED and LPBF that can produce microstructures incomparable to wrought or cast components with extend solubility of solute, reduction in segregation, and differences in solidification structures and phases [8–11]. A focus is placed on the solidification microstructure resulting from these additive processes as rapid solidification routinely results in differences in the properties and structures that have been well established and can be predicted

in wrought and cast titanium alloys. As the process is further developed, specialty alloys designed for the process are likely to develop with key microstructural features in mind.

However, the current process necessary to develop a prototype alloy is extensive with the atomization of titanium requiring significant industrial and energy resources to produce the necessary kilograms of powder needed to create a single batch of AM components for microstructural study. The current method used to create high quality and low impurity titanium powder is plasma atomization or plasma rotating electrode process (PREP) both processes require the creation of high quality feedstock or wire [12]. The inherent cost sunk into powder creation places a necessary burden that testing new compositions be screened prior to atomization to both reduce costs and waste of kilogram sized batches of powder is an alloy has negative effect that make in unsuitable for further use. With this in mind, rapid solidification techniques that use grams of material and allow for quick alloy prototyping and examination stand to be a valuable asset.

1.2.0 Literature Review

A review of literature relevant to this research and dissertation are discussed in this section. The review covers the titanium alloy system, the current methods to predict titanium phase stability, rapid solidification, history of rapid solidification studies on titanium, and develops a case for further study in the reviewed fields.

1.2.1 Overview of Titanium Alloy System

The titanium material system has several crystallographic phases that can controlled and manipulated both through composition as well as processing route to produce the wanted mechanical properties and microstructure [1,13]. Pure titanium is allotropic and as such exhibits a high temperature body centered phase (β) and a low temperature hexagonal closed pack phase

(α). The transition temperature between these two phases is called the transus temperature and plays an important function as a limit on the operating temperature of many titanium alloys due to the reliance of the α structures for strengthening. The stability of β at lower temperatures can be increased by addition of beta stabilizer (Mo, V, Fe, etc.). As the addition of the β stabilizers increases, they allow for retention of beta that is only stable upon quenching, known as metastable beta, or upon significant solute additions the beta phase can be completely equilibrium stabilized at room temperature. In contrast, α stabilizers such as aluminum or several interstitial additions are also available that can counteract the ability to retain the BCC phase resulting in further stabilizing the α phase. The most widely used α stabilizer is aluminum with interstitial solute additions such as oxygen controlled and limited due to decreases in fracture strength and ductility. The general designation classes of titanium alloys are based on the proportions of these two dominant phases present at room temperature.

The titanium alloys are traditionally classified into several categories (α, α+ß, ß) according to the percentage of beta present at room temperature. The α alloys are generally composed of commercially pure (CP) titanium as well as several niche class of alloys that are further stabilized to form high temperature phases such as titanium aluminide intermetallics or to provide solid solution strengthening while retaining the excellent corrosion resistance of CP-titanium [3]. The suite of α+β alloys are generally the most widely used with Ti-6Al-4V having become the work horse alloy with 56% of the US titanium market in 1998 [13]. The criteria for what are considered an α+ β alloy does not have a distinct boundary with a small percentage (<10%) of the β phase acting as a limit as well as the tendency to martensitically transform upon quenching. The β alloys are generally broken into a metastable and stable variant. Metastable beta alloys such as Ti-5553 do not demonstrate a martensitic phase transformation upon cooling

and generally can be heat treated to allow for precipitation hardening by α phase [14]. The stable beta phases are fully beta stabilized and have seen significant interest for biomedical applications as well as in springs, due to the ability to control the Young's modulus via alloy composition[15–20].

As such, significant areas of titanium alloy design are concentrated around controlling and developing certain volume fractions and morphologies of phases to promote the desired properties. The presence and stability of these phases is largely compositionally controlled, though cooling rates have been demonstrated to also allow for nonequilibrium proportions of the α and ß phases, as well as controlling the presence of martensitic phases transformations[1,14,21]. The solutes commonly used in titanium alloys can divided based on several categories such as the equilibrium phase stabilized as well as types of transformation formed during cooling as shown in Figure 1.1. For the α stabilizers, several elements, such as oxygen and nitrogen, act as interstitial additions while the remainder of the group are non-transition metals such as aluminum and rare earth elements. In contrast, the beta stabilizers are largely dominated by transition metals such as vanadium, iron, molybdenum, or chrome. The most widely denoted difference in the β stabilizers is whether the binary phase diagram forms a eutectoid. There are also a few select elements that are traditionally neutral additions such as zirconium and tin that are alloyed with titanium but do not cause a significant change in phase compositions.

To denote and allow for rough estimation of the phase composition, molybdenum equivalency values have been developed that can roughly equate the compositions of alloys. Table 1 give the molybdenum equivalency (Mo_{eq}) and aluminum equivalency (Al_{eq}) from several

works [1, 21–23]. In general applications the use of these equivalencies is a simple summation of each element's equivalency multiplied by its weight percentage as shown in equation 1.

$$Total\ Equivalency = \sum Mo_{eq} * wt\% - \sum Al_{eq} * wt\% \qquad (1)$$

The equivalency results in a positive value for beta stabilized alloy such as Ti-5553 (Mo_{eq} value of 8.35 using Cotton's Mo_{eq} values [22]). As demonstrated in Table 1 and 2, the values assigned to each element have some variance such as iron having a range between 2.5-2.9. Molybdenum equivalencies are generally used as an empirical guide to distinguish between the classes of titanium alloys. Other more physics-based methods for estimating the stabilized phase for a given titanium alloy are by correlating the average bond order of the covalent bond versus the d-orbital energy level of the alloy as well as a method that evaluates the valence electrons per atom. Both methods have been reported in the literature to allow for a more quantitative number for understanding the phase stability and deformation mechanism of a given alloy[16,25].

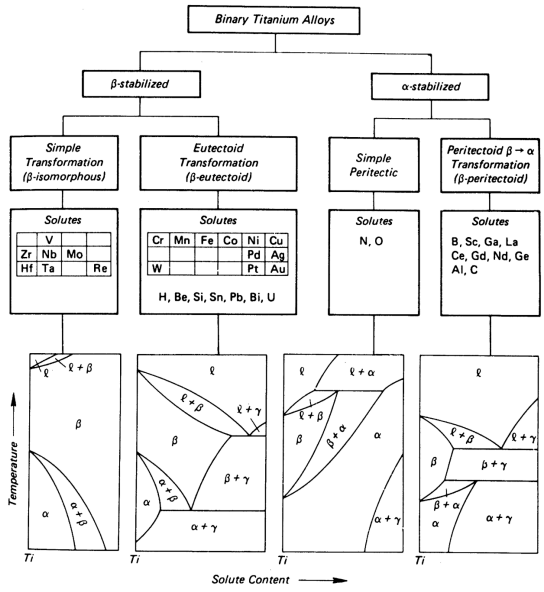

Figure 1.1 A graphical demonstration of the generalized solute categories used in titanium alloys. The solutes are first split by what phase is stabilized upon addition and secondly by the presence

of certain microstructural features on their binary phase diagram such as isomorphous or eutectoid in the ß stabilizing species [26].

	Al_{eq}		
Element	**Bania**[23]	**Collings**[2]	**Cotton**[22]
Al	1	1	1
N		10	10
O		10	10
Sn		0.33	0.33
Zr		0.17	0.17

	Mo_{eq}		
Element	**Bania**[23]	**Collings**[2]	**Cotton**[22]
Co		1.7	
Cr	1.6	1.25	1.6
Fe	2.9	2.5	2.9
Mn		1.7	1.7
Mo	1	1	1
Nb	0.28	0.28	0.28
Ni		1.25	
Ta	0.22	0.2	0.2
V	0.67	0.67	0.67
W	0.44	0.4	0.44

Table 1.1 Molybdenum and aluminum equivalency values for generally used alpha and beta stabilizing elements. Three separate studies were chosen to demonstrate the fluctuation of values and lack of inclusion across the literature.

As the use of titanium for biomedical applications grew, the ability to predict the elastic modulus and deformation mechanism through the use of physics-based models became increasingly desirable. As such, the DV-Xα cluster method was derived from a solid state physics approach that allows for the correlation of empirical data onto a plot of the average mean d-Orbital energy level (Md) and covalent bond order (Bo) as seen in Figure 1.2 [27,28]. These

values are calculated for a singular solute atom in the BCC structure of titanium and allows for plotting of alloys in a 2D space with the position of alloys resulting from vector addition of the solute elements without the scatter in values associated with the molybdenum equivalency values [29]. The use of this model allows for an easy calculation of the Bo and Md value of any given alloy that can be correlated to properties such as deformation mechanism, phase stability, and elastic modulus such as work by Abdel-Hady et al. seen in Figure 1.2 where various titanium alloys are plotted with various features of the alloys such as phases and deformation mechanisms are labeled [29]. As oxygen is not a substitutional solute addition it cannot be predicted with this approach, but due to its importance, work has been previously done to demonstrate that it seemingly reduces the metastable region between the pure α and ß regions. [29]. This method has seen further development into more generalized alloy design uses such as predicting deformation mechanisms and martensite development that allow for a deeper understanding on solute changes to alloys beyond what is offered by the molybdenum number [30].

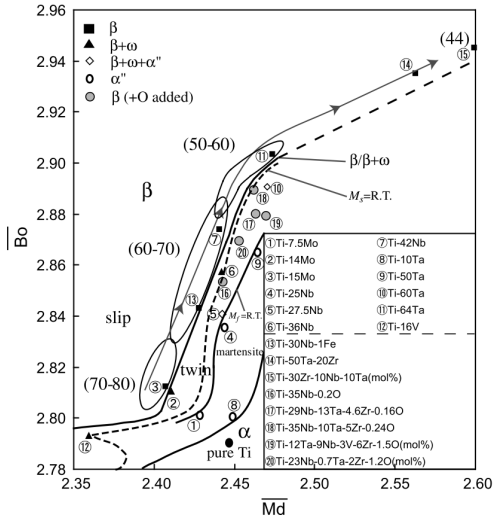

Figure 1.2 Plot of covalent bond order (Bo) and mean d-Orbital energy level (Md) for various titanium alloys demonstrating the potential of the technique to predict metastable qualities of the alloys such as modulus, deformation mode, and secondary phases [29].

The addition of interstitial oxygen to a titanium alloy can have drastic effects on the microstructure and mechanical properties of the material and is generally the most closely monitored addition in wrought or cast product. Titanium has a significant affinity for oxygen with not only a strong thermodynamic driver for oxide but the ability for oxygen to sit interstitially in the titanium matrix. Oxidation can occur in titanium in temperatures even as low as 400°C with the rate of oxide growth and oxygen pickup increasing drastically at higher temperature [31]. This correlation of temperature with oxygen pickup is a major concern due to the numerous high temperature processing steps needed both in feedstock preparation but also in component manufacturing. The oxygen stabilizes the alpha phase in α+ß alloys and has been shown to drastically increase the yield strength of structural alloys such as Ti-6Al-4V at the cost of lowering the fracture strength and ductility[32–37]. Oxygen has also been shown to increase the self-diffusion in titanium allowing for refined microstructures in the grain boundary beta alloy in Ti-6Al-4V (demonstrated in Figure 1.3) that explain both the increased strength but also the decreased ductility seen with increased oxygen content[38]. As such, the oxygen content in wrought product is a major concern for industrial use and has required refinement of processing so eliminate the possibility of oxygen induced loss of fracture toughness.

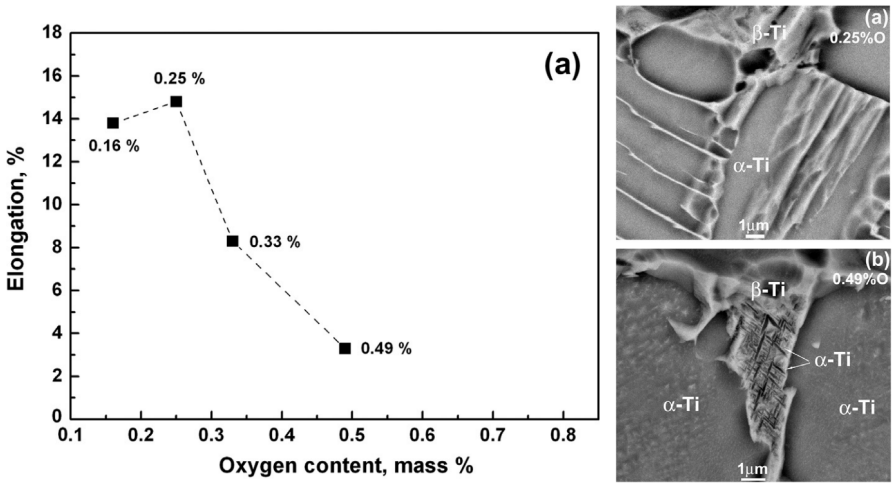

Figure 1.3 Elongation of as-sintered Ti-6Al-4V as a function of oxygen as well as SEM-BSE images of the ß phase in the material with the low oxygen material having a solely ß grain boundary and the higher oxygen content having a refined alpha platelets in the grain boundaries that resulted in intergranular fracture [38].

Beyond the two dominant phases are martensitic phases formed by a diffusionless phase transformation from cooling or applied stresses. There are two martensitic phases formed in titanium with the resulting martensitic crystal structure determined by the composition of the alloy. The α' phase is an hcp structure that is crystallographically identical to the α but formed by a military diffusionless phase transformation caused by a coupled shear and shuffle displacement [39]. The orthorhombic α" phase is similarly formed but due to increased beta stabilizers present in the alloy, it is unable to form the hcp martensite crystal structure. The difference between these two crystal structures and the BCC phase that is retained at higher compositions has been studied and found to be a continuum, demonstrated by Figure 1.4, with the orthorhombic phases existing as an intermediate phase between the HCP and BCC for numerous binaries such as Ti-Nb and Ti-Mo system [15,40]. In addition to the crystal structure, the internal microstructural

feature of the martensite is affected by the change from HCP to orthorhombic [21]. These structural differences between the two phases result in the orthorhombic α" being the softer of the two phases in spite of the additional solid solution strengthening offered by the increased solute content. In work by Davis et al. the hardness difference was attributed to inter-martensitic ß and dislocation tangles present in the 2 wt% Mo α' (HCP) martensite with the 8 wt% Mo α" (orthorhombic) martensite having dislocation free acicular martensite containing twins and stacking faults [21]. In addition to martensitic transformation upon quenching, metastable beta alloys also demonstrate the tendency to form strain induced martensite (SIM) [25,41]. The formation of SIM can largely be correlated to the region of alloy space where the BCC phase is not fully stabilized but there isnot enough of energetic benefit to phase transition upon quenching relying on applied stress to complete the transition into martensite [29,41].

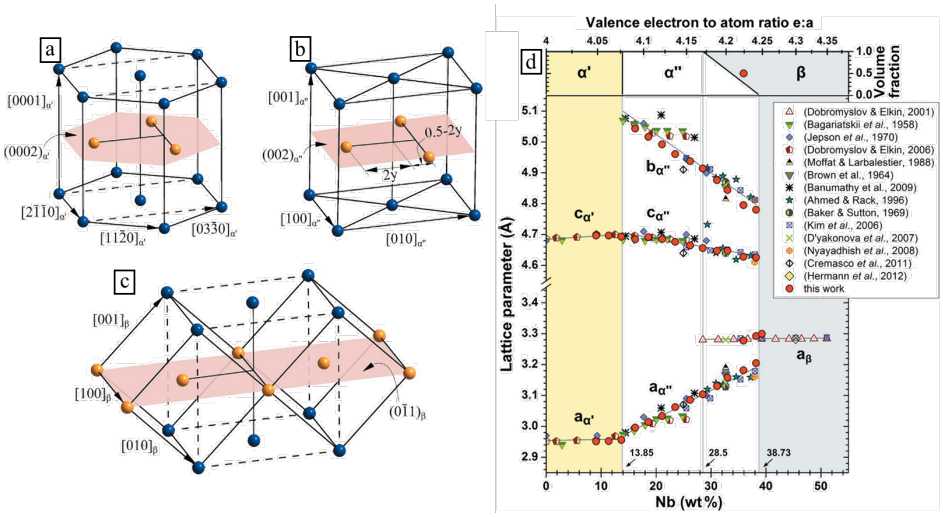

Figure 1.4 Diagrams of the (a) HCP, (b) Orthorhombic, and (c) BCC crystal structures demonstrating that they can all exist inside a parent Cmcm structure that is defined by a change in a y-distance. (d) Lattice parameters as a function of Niobium in Ti-Nb binaries demonstrating the gradual change from HCP to BCC via an intermediary Orthorhombic structure [15].

Similar to the martensitic phases, the omega phase is formed by a separate, diffusionless phase transformation in certain beta stabilized alloys. Unlike the shear driven martensitic formation, the omega phase is formed by the collapse of (111) planes in the parent BCC lattice [43–45]. This phase has two generally accepted forms, namely an isothermal and athermal variety. The athermal is formed upon quenching and can be found in beta stabilized alloys such as Ti-Mo binaries. The isothermal phase is formed during isothermal aging treatment and as such the heat treatment route of these alloys is controlled to precipitate out the alpha structures needed for strength while reducing the growth of the omega phase [44]. Both versions of ω are coherent with the beta matrix with a generally reported hexagonal crystal structure but has been demonstrated to have a trigonal structure in some heavily stabilized alloys [46]. The morphology of the ω phase has been shown to be able to form either ellipsoidal or cuboidal particles, depending on the lattice mismatch, in the range of 5-10 nm in an alloy such as Ti-5553 but can see significant differences in sizes based on the composition of the alloy [45,47]. Counterintuitively for a beta stabilized alloy, the ω phase formation can be controlled and limited by the addition of α stabilizers such as Al and O [25,48]. The omega phase has the highest young's modulus of the titanium phases that increases when in the isothermal variety as the phase diffuses out unwanted solute[49]. The result of omega phase content either from quenching or heat treating generally results in drastic lowering of ductility that practically results in heat treatment and alloy design intended to avoid the phase forming.

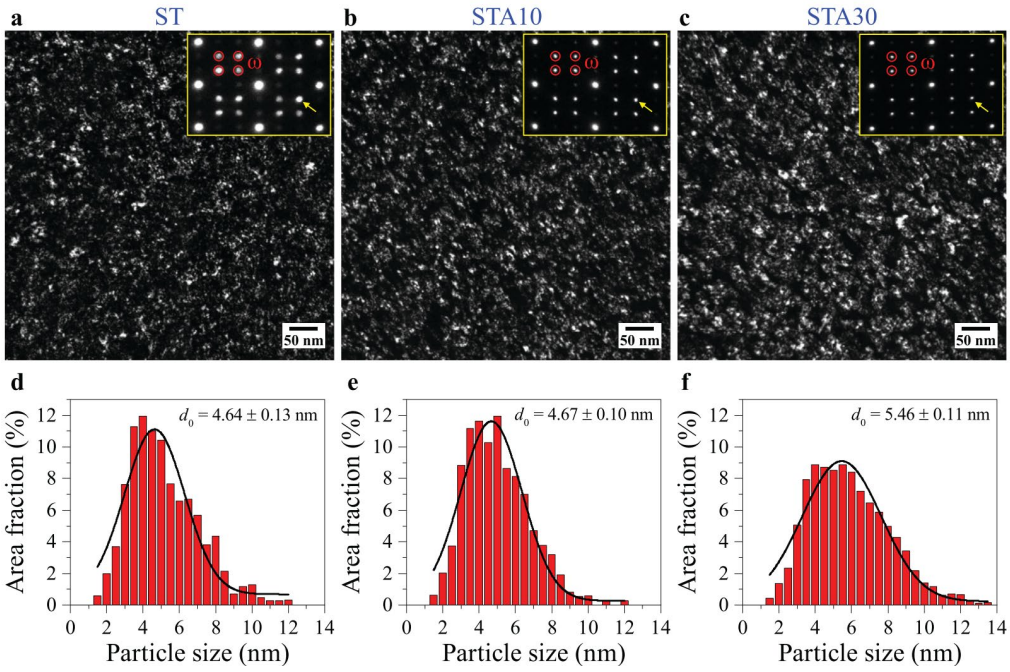

Figure 1.5 Darkfield images of Ti-12Mo highlighting the omega phase from solution treated and quenched as well as two natural aging times. The omega phase is seen to grow in size when naturally aged as well as diffusing out solute [49].

1.2.2 Rapid Solidification

Understanding of rapid solidification is critical in additive manufactured alloys such as titanium as it effect the solid-liquid interfacial stability, segregation, and undercoolings that occur in a solidifying material that all can play an effect in the final microstructure. Many approaches to additive manufacturing of titanium alloys involve rapid solidification and its impact on phase composition and microstructure demand careful investigation. Rapid solidification can be defined by a breakdown in the equilibrium in solid liquid interface. This breakdown in equilibrium is generally seen when the solidification velocity increases above 0.1 m/s as there is not enough time for diffusion to occur at the interface. This results in a breakdown of many of the solidification models used in casting. Therefore, the effect of rapid solidification

on morphological stability is a continually reoccurring area of research in the field of solidification as the solidified morphology has direct effects to post-processing and mechanical response of the material and varies by alloy and processing technique. It is a well-known phenomenon that as the cooling rate or solidification velocity increase that the resulting microstructure trends from a planar growth mode to columnar/dendritic and back again [50]. This effect can be seen in microstructure selection maps as seen in Figure 1.6 . This figure demonstrates two main points of interest when investing morphological phenomena, namely that solute addition effects the stability of the solidification mechanisms and that given a high enough solidification velocity even non-dilute alloys will trend towards planar solidification.

The first area to be introduced to understand the behavior of solidifying material is undercooling types and how they control the solid-liquid interface. The concept of undercoolings are complex but described briefly is the undercooling at which the solid-to-liquid phase transformation occurs [51]. This undercooling is therefore needed to solidify and can be achieved through several means that sum to create a driving force for solidification. The three main undercoolings relevant to rapid solidification are curvature, thermal, and constitutional undercoolings. The curvature undercooling is a term related to the creation of new interface between the newly solidified material and the liquid melt. As such, the curvature undercooling help determine the size of cells with smaller radius structures resulting in increased curvature undercooling. Thermal undercooling is simple in complex as it is the temperature below the liquidus and can develop from high thermal gradients or nucleation difficulties. The constitutional undercooling is based on solute interaction with the solidifying material. As the material solidifies there is an energetic benefit to segregation as it can lower the Gibbs free energy of the solid phase. The constitutional undercooling is typically the dominant undercooling

for alloys and results in the formation of the dendritic and cellular structures typical in solidified structures. There are additional undercoolings such as pressure and kinetic undercooling that can additionally affect the microstructure at extreme pressures (~1 GPa) and solidification velocity extremes. As such in RS applications the small cell size, decreased segregation, and ability to form sharp gradients all lead to changes in the dominant undercoolings away from typical values that lead to an area for additional research in the field of solidification.

Considering the advent and growth of the additive manufacturing field, the interest in rapid solidification has increased to a new height trying to provide a predictive framework on the microstructure and segregation profile of AM produced components. Work such as by Galenko et al. uses techniques such as melt spinning or hammer and anvil quenching to achieve the high solidification velocities necessary to form planar solidification [52]. The solidification velocity in these materials is nonuniform and so a range of solidification microstructure can be displayed such as in Figure 1.7. with a melt spun Ni-18at%B alloy that exhibits planar solidification at the chilled surface that trends towards dendritic throughout the thickness. A benefit of the high velocity planar solidification compared to columnar dendritic is a reduction in the segregation due to the solidifying material having insufficient time for diffusion to occur. Work by Aziz et al. has attempted to capture the behavior of solute trapping with the Continuous Growth Model (CGM) as well as several analytical solutions for solute partition coefficient [53,54]. Aziz et al. reported an equation (Eqn. 2.) that correlated the solute partition coefficient, $\frac{c_{solid}}{c_{liquid}}$, to the ratio of the solidification velocity to the diffusive speed, Eqn 3.

$$k(v) = \frac{\frac{V}{V_d} + k_e}{\frac{V}{V_d} + 1} \quad (2)$$

$$V_d = f v \lambda e^{\frac{-Q_d}{RT}} \quad (3)$$

As the solid phase grows, so called “impurity” atoms can become entrapped at the interface. If the solute cannot diffuse back into the liquid before the next step of the solid liquid interface, then the solute will become entrapped. The ability for solute atoms to diffuse into the liquid and enrich the solid-liquid interface leads to constitutional undercooling. Here again, it is shown that an increasing velocity would result in a segregation coefficient trends toward unity as the allowable time for the solute to return to the liquid melt is decreased as the velocity increases. Further work on the segregation model such as the local non-equilibrium diffusion model (LNDM) by Sobolev et al. have been made to better capture the high velocity range as the CGM only predicts complete solute entrapment (k=1) at infinite velocity [55]. The LNDM model introduces a maximum speed of diffusive perturbations that once the interfacial velocity reaches the segregation coefficient turns to 1.

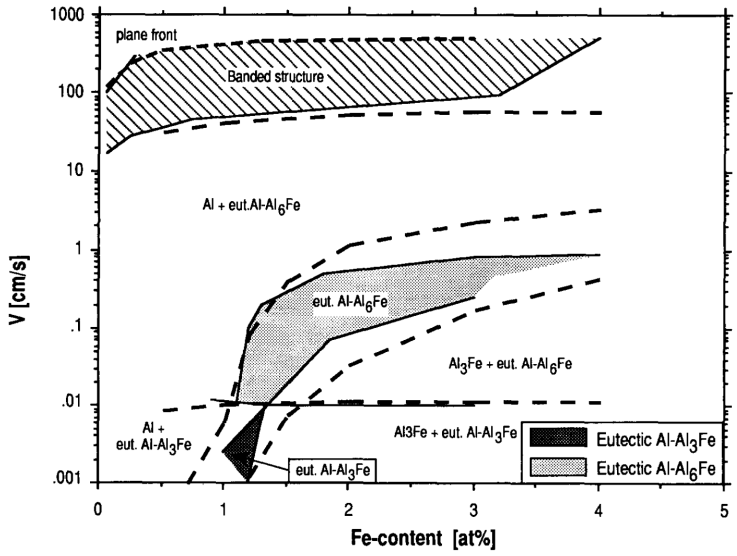

Figure 1.6 Microstructure selection map for the Al-Fe system highlighting that both composition and solidification velocity have an effect on the resulting microstructure [50].

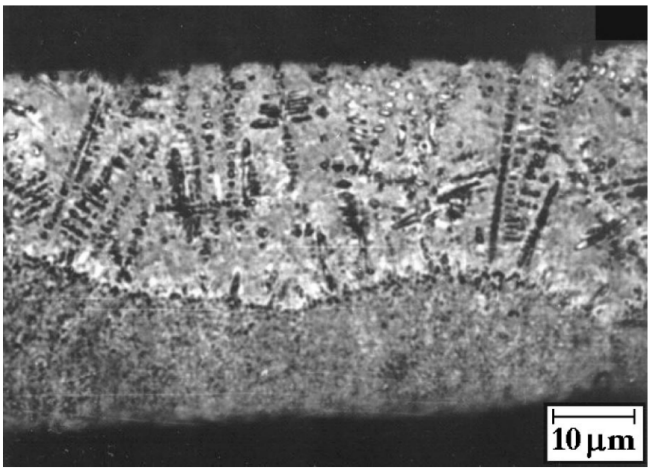

Figure 1.7 Optical micrograph of melt-spun Ni-18% B ribbon. The microstructure exhibits a change from planar solidification to dendritic from bottom to top of the ribbon [52]

Reducing the solidification velocity results in the return of the typically seen cellular-dendritic material. On a qualitative level, the selection between planar and dendritic is a competition between solute effects and interfacial surface tension. In a review by Trivedi et al. several criteria are developed linking the interface conditions to several characteristics length by relationships between these lengths the dominant solidification mode can be established [56]. Another common metric of the transition is the Peclet number, Eqn 4, that is the ratio of a characteristic length (L) and twice the solute diffusion length. The characteristic length is generally measured as the spacing between primary dendrites or cells that can be used as a measure of the perturbation spacing in the solid-liquid interface.

$$Pe_i = \frac{L}{2l_i} \qquad (4)$$

As the peclet number approaches unity then the diffusion becomes localized without the ability to create any significant solute rich boundary. In rapid solidification where the interface velocity enforces a small diffusional length then the Peclet number will tend to be above unity. In

summary, the solidification morphology that is dominant is controlled by several key parameters ranging from interfacial velocity that controls the diffusion response as well as atomic attachment method to wetting angle that controls the stability of interfacial fluctuations. While some variables are characteristic of the alloy others are controlled by the solidification itself. This is an interesting, coupled situation as both in the material itself and in the method of solidification there are variables to control so modification to the processing method or the material will allow selection and control of the resulting microstructure.

Beyond solid-liquid interfacial qualities, nucleation behavior has an intrinsic effect on the microstructure whether columnar or equiaxed grains dominate. In a melt, an undercooling is needed to provide the energy needed to overcome the nucleation barrier that is inherent to forming a solid-liquid interface. As this undercooling amount increases therefore the driving force for solidification grows. Homogeneous nucleation would then occur when there is sufficient driving force to enable the retention and subsequent growth of atomic clusters in the melt. At a high enough undercooling, these clusters are stable and begin growing until there is no more liquid. This situation is quite rare in traditional solidification techniques due to preferential substrate growth. Whether a mold wall in castings, or the underlying material in a laser pass, the energy to nucleate a solid can be drastically reduced by relying on growth from an existing crystal structure. This reduction in energy can be estimated by a geometric function of the wetting angle of the liquid melt when placed on the substrate. The equation can be seen in Eqn X. as a simple fraction of the homogeneous nucleation value. S(θ) is referred to as a shape factor and trends towards unity as the wetting angle , θ, increases thereby demonstrating poor wetting of the substrate similarly means a higher undercooling needed to nucleate off of the substrate.

$$\Delta G_{het} = \Delta G_{homo} S(\theta) \qquad (5)$$

$$S(\theta) = (2 + cos\theta)(1 - cos\theta)^2/4 \quad (6)$$

Homogeneous nucleation has been seen in some RS studies due to high cleanliness of the melt and fast cooling allowing for the development of the undercoolings needed [57,58]. Work by Turnbull evaluated the maximum undercooling of pure metals and found that generally ~0.2Tm is needed for metals to homogenously nucleate [59].Outside of these cases, heterogeneous nucleation is the dominant mode of nucleation. Heterogeneous nucleation due to the nature of growth on a substrate reduces the undercoolings needed to solidify molten material.

While nucleation is not inherently controlled by rapid solidification conditions, the velocity and gradient ahead of the solid-liquid interface creates the potential for either columnar or equiaxed grains to form and determine the final microstructure. The constitutional undercooling caused by solute segregation at the solid-liquid interface slows down growth of grains and the thermal gradient if large enough can cause nucleation of new grains in front columnar front. This competition between columnar growth and equiaxed grains has seen the creation of models such as by Hunt et al.[60] or modified for use in rapid solidification conditions by Gäumann et al. [61,62]. Explained simply, the thermal gradient in the melt in addition to the effects such as constitutional undercooling in front of the solid-liquid interface act to allow for nucleation of grains in front of the previous interface. If these newly nucleated grains grow, then the previous interface is effectively stopped, and the new grain can continue to grow until blocked by subsequently new grains. This results in a battle between columnar growth where grains nucleate and then the primary mode for solidification is attachment to the existing solid liquid interface and equiaxed grains where the grains can grow but its ultimately easier for other grains to nucleate and grow before ultimately blocked by surrounding grains. In cases such as turbine blades columnar growth is essential but in other applications equiaxed grains are

preferable due to a reduction in anisotropy or segregation. As such, the Hunt model and subsequent modifications over time takes in inputs such as thermal gradient, segregation parameters, and nucleation sites to offer a predictive tool as seen in Figure 1.8.

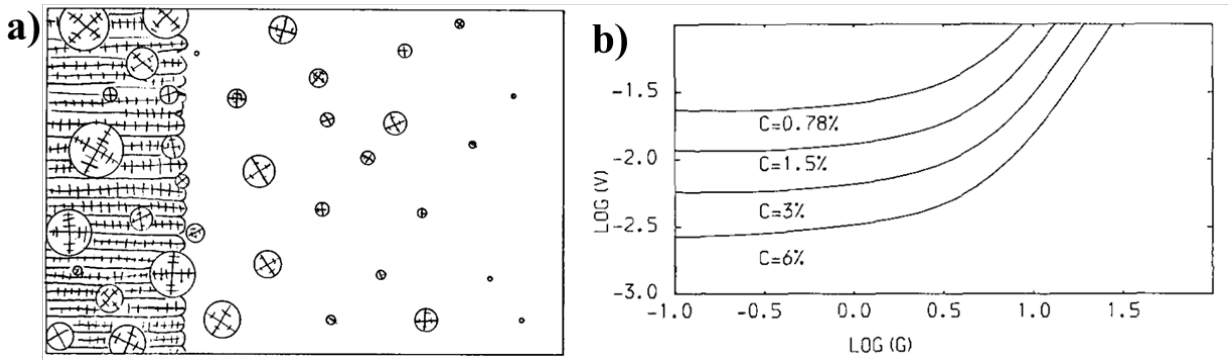

Figure 1.8 (a) Diagram of a columnar growth occurring with nuclei ahead of the growth front beginning to grow. Depending upon the size of the equiaxed grains the columnar front is broken and the resulting microstructure is fully equiaxed seen for (b) Al-Cu binary alloy[60].

Having examined the nucleation, interfacial stability, and the interplay between the two found in columnar to equiaxed transition, a basic framework on solidification has been found to begin examining rapidly solidified material to understand the correlation between the solidification morphology, microstructure, and solidification conditions.

1.2.3 Rapid Solidification Methods

Rapid solidification techniques are varied across several disciplines based on how the cooling rates necessary are created. The main rapid solidification processes have been generally binned into three groups based on working mechanism and thermal profiles by Kurz et al. with illustrations of the heat transfer characteristics of each category of rapid solidification [63]. The first of the process groups is rapid movement of high energy source such as in laser surface

treatment, single laser track melting, or in fusion based AM processes. The benefit of these processes is the ease of modeling the thermal profile to estimate values for velocity and thermal gradient. The second grouping is based upon high cooling rates generated from contact between molten material and a substrate, generally copper. Techniques such as splat quenching, melt spinning, and thermal spray follow under this umbrella allowing for extremely high cooling rates but controlled by the thickness of the material. The final overall category is techniques that rely on undercoolings. Atomization techniques with spherical particles largely dominate this category, which is unique amongst the three groups because it can demonstrate a negative thermal gradient. The differences between the cooling behavior of the three methodologies means that solidification morphology and characteristics can be different between all three.

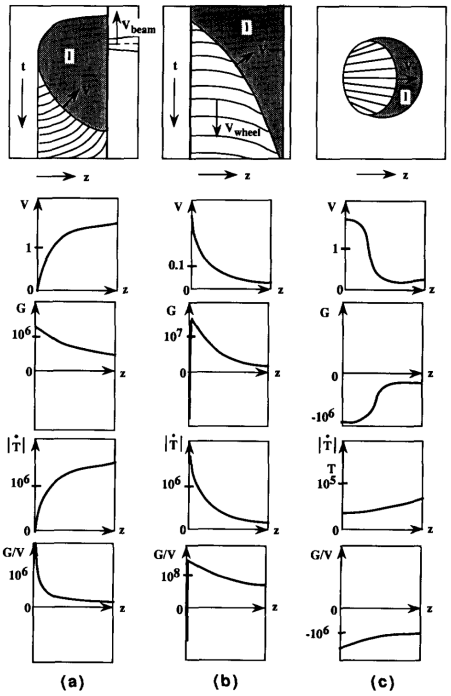

Figure 1.9 Graphical representations of the three general types of rapid solidification techniques highlighting the change in solidification velocity (V), thermal gradient (G), cooling rate ($\dot{T}$), and G/V ratio for each process[63].

Of particular interest to this dissertation is two-piston splat quenching (SQ) that belongs to the second group of rapid solidification methods relying on thermal contact between molten material and copper substrates. In this technique a small cube of metal (typically 2-3 mm on a side) is inductively levitated and heated to a desired superheat temperature. When the desired temperature is reached, the induction field is turned off and the droplet of molten metal falls and is rapidly compressed between two projectile platens moving in the range of 3.5 m/s. The collision between the platens results in the liquid material flattening as well as ensuring quality thermal contact between the platens and melt. SQ has a number of key features that make it the attractive choice for this study. It provides a relatively cheap yet repeatable means of producing RS materials, which is faithful to the cooling rates seen in LPBF techniques. Vitek, Ruhl, and Inokuti, Hayzelden all estimate/measure the cooling rates for two-piston SQ to be on the order of 10^5-10^6 C/sec with an iron alloy and copper platen [64–67]. Various modifications of splat quenching techniques have been utilized to study different aspects of RS. These techniques include the Duwez gun, Rotary Splat Quencher, Piston and Anvil Technique, and Two-Piston Splat Quencher. Both the Duwez gun and Rotary Splat Quencher, produce very thin discontinuous metal foils not suitable for measuring mechanical properties, but they also achieve the highest cooling rates (10^{10} C/sec) of the four techniques mentioned [67–72]. The piston and anvil and two-piston splat quench technique, however, produces more consistent, repeatable splat foils. Some work has been done to model the changes to the solidification conditions of rapid solidification techniques study evaluated the effect of position in the splats on the cooling rate with the interfacial material having an expectedly higher cooling rate than material near the midplane [65]. Several other parameters were varied and demonstrated minimal changes to the cooling rate such as initial substrate temperature, splat super heat, or solidification range. The

dominating factors found to control the cooling rate of the material were the coefficient of heat transfer between the splat and substrate as well as the thickness of the splat that could be affected by both the platen velocity as well as the superheat applied to the melt[70]. For both of these parameters, splat quenching offers significant benefit in repeatability as the substrates are electromagnetically shot together forcing contact between the melt and the substrate unlike in other splatting process where the solidified material can detach from the chilling surface or have varying thicknesses.

1.2.4 Rapid Solidification of Titanium

Rapid solidification of the titanium alloy system has been explored as a way to utilize the unique benefits of RS to control elemental segregation and solidification microstructure but has not been done to the extent of other alloys systems such aluminum or stainless steels. Due to the high reactivity of molten titanium, there is increased difficulty in the study of RS behavior as compared as compared to other structural alloy systems such as iron and aluminum alloys. As such, many of the studies on the titanium system are limited to containerless techniques such as inductive levitation or centrifugal methods [73,74]. Historically, RS of alloys was examined as a means to increase solubility in structural alloys such as aluminum, but due to titanium having high solubility with a significant number of elements this driving force for research was lessened. Therefore, research examining the potential for RS induced extended solubility focused on rare earth additions and metalloids that both demonstrate vastly lower solubility than the transition metals that are generally added to titanium alloys [74].The use of RS on the rare earth elements was found to produce dispersoids for strengthening with the resultant particle sizes a function of cooling rates [26,68,73–75]. The additions of more traditional solutes such as iron and nickel has been more recently studied due to the expanded interest in beta stabilized titanium

alloys. As the drive for this research is the maturing fusion based AM field, laser based RS techniques have been explored to understand the effect of the solidification conditions on titanium alloys. Work such as Roehling et al. investigate the relationships between solidification conditions, morphology, and segregation of alloys such as Ti-50 Nb to provide deeper understanding for further use in AM such as cell size and segregation that was used to calibrate a phase-field model[76]. Study of rapidly solidified Ti-V binary alloys has been conducted by Suwarno et al. as a way to increase the hydrogen storage capability of titanium alloys to limited success [77]. In total, rapid solidification studies for designing of titanium alloys are rather limited with intermittent examination across a wide range of applications and solute additions that make it difficult to predict the solidification properties in RS conditions.

In spite of a lack of segregation prone solutes, Ti-6Al-4V and its response to rapid solidification have been studied due to the dominance of the alloy as well as the widespread use of processes such as AM and laser welding that are performed on the alloy. Broderick et al. studied the effect of solidification rate across a range of techniques from powder made by rotating electrode extraction to foils made by hammer and anvil splat quenching [78]. This work correlated the beta grain size to the estimated cooling rate across the techniques to beta grain size as estimated by homogeneous nucleation and isotropic linear growth that has been used in other works investigation splat quenching materials [58]. Other work has focused more on atomized powder looking to understand the cooling rates and microstructure resulting from the atomization process [79]. Interestingly, the change in cooling rate across powder size was seen to correlate to a change solidification structure, martensite development, and hardness that leads to further interest into the effect of rapid solidification in a more complicates alloy in the titanium system.

Splat Quenching (SQ) rapid solidification studies of titanium offer a potential to study the solidification behavior that is intrinsic to processes such as AM without the need for kilograms of powder. To limit the cooling rate, several papers have demonstrated the use of gas flow on the melted material to undercool [80,81]. The undercooling in a study by Kral et al. was able to reduce the cooling rate enough to result in the formation of rare earth precipitates rather than the α' that formed upon splat quenching at the melting temperature[80]. Research on rapid solidification of beta titanium alloys is limited due to the prevailing interest of the RS literature being on the formation of dispersoids in α-stabilized alloys. Work by Krishnamurthy et al. has used the SQ technique on a range of beta titanium binaries containing eutectoid formers that demonstrate regions of partitionless solidification but is largely a qualitative study on the microstructural features of the alloys [68,82]. Ti-Fe binary alloys (10-50 wt%) have been splat quenched by Ray et al. that demonstrated an extension of the Fe solubility up to 35 at%, up from 13 at% at 590°C typically, before the formation of a metastable ordered Ti-Fe phase with the eutectoid forming only at a composition of Ti-50Fe [83]. As such, there is a currently limited data to inform alloy creation in the beta titanium alloy space especially.

1.3.0 Summary of Background and Literature Review

Titanium alloys are a highly versatile alloy system that offers a wealth of metallurgical benefits for use across numerous industries due the high strength to weight ratio, corrosion resistance, and performance at temperatures. But due to difficulties in processing because of high melting temperature and sensitivity to oxygen, there are significant areas of fundamental research in the areas of phase stability and solidification behavior that need to be addressed as the alloy space gains further development for AM applications.

- Phase fractions are a function of both composition and cooling condition, but research is largely dominated by the Ti-6Al-4V alloy, with relatively little information on the beta-stabilized alloys.
- Rapid solidification offers several key advantages in terms of increased solute solubility and decreased feature size that alloy for elimination of intermetallics that can form during casting.
- The actual effect and modeling of solidification structure and elemental segregation as a function of solidification velocity has not been captured due to the limited use of high segregating solute additions in previous generations of titanium alloys.

1.4.0 Research Objectives and Dissertation Structure

Considering the findings from literature, the following topics will be investigated:

1. Investigate the cooling rates and controlling parameters in the splat quenching experiment and their effect in general and on the titanium alloy system in particular.

2. Correlating powder atomization, splat quenched foils, and laser welding to a cooling rate to understand the response of titanium solidification across a suite of solidification conditions.

3. Validation of various thermodynamic and empirical models to predict martensitic formation upon quenching in metastable beta alloy.

This research is presented in a paper-style format. Following the introduction, chapters 2-4 address the three technical objectives in the order listed above. These chapters are followed by a conclusion and recommendations for future research in chapter 5.

References

[1] E.W. Collings, The Physical Metallurgy of Titanium Alloys, American Society for Metals, 1984. https://books.google.com/books?id=PtRTAAAAMAAJ.

[2] J. Allen, An Investigation into the Comparative Costs of Additive Manufacture vs. Machine from Solid for Aero Engine Parts, 2006.

http://oai.dtic.mil/oai/oai?verb=getRecord&metadataPrefix=html&identifier=ADA521730.

[3] G. Lutjering, J.C. Williams, Titanium, 1990. https://doi.org/10.5005/jp/books/11706_12.

[4] L. Nastac, M.N. Gungor, I. Ucok, K.L. Klug, W.T. Tack, Advances in investment casting of Ti–6Al–4V alloy: a review, Https://Doi.Org/10.1179/136404605225023225. 19 (2006) 73–93. https://doi.org/10.1179/136404605225023225.

[5] J.D. Cotton, L.P. Clark, T.R. Reinhart, W.S. Spear, S.J. Veeck, G.R. Strabel, Inclusions in Ti-6Al-4V investment castings, Collect. Tech. Pap. - AIAA/ASME/ASCE/AHS/ASC Struct. Struct. Dyn. Mater. Conf. 1 (2000) 879–887. https://doi.org/10.2514/6.2000-1464.

[6] ISO/ASTM, Additive Manufacturing - General Principles Terminology (ASTM52900), Rapid Manuf. Assoc. 2021 (2013) 10–12. http://www.ciri.org.nz/nzrma/technologies.html.

[7] S. Liu, Y.C. Shin, Additive manufacturing of Ti6Al4V alloy: A review, Mater. Des. 164 (2019) 107552. https://doi.org/10.1016/j.matdes.2018.107552.

[8] J.C. Colombo-Pulgarín, C.A. Biffi, M. Vedani, D. Celentano, A. Sánchez-Egea, A.D. Boccardo, J.-P. Ponthot, Beta Titanium Alloys Processed By Laser Powder Bed Fusion: A Review, J. Mater. Eng. Perform. (2021). https://doi.org/10.1007/s11665-021-05800-6.

[9] D. Zhang, D. Qiu, M.A. Gibson, Y. Zheng, H.L. Fraser, D.H. StJohn, M.A. Easton, Additive manufacturing of ultrafine-grained high-strength titanium alloys, Nat. 2019 5767785. 576 (2019) 91–95. https://doi.org/10.1038/s41586-019-1783-1.

[10] C. Hicks, T. Konkova, P. Blackwell, Influence of laser power and powder feed rate on the microstructure evolution of laser metal deposited Ti-5553 on forged substrates, Mater. Charact. 170 (2020) 110675. https://doi.org/10.1016/J.MATCHAR.2020.110675.

[11] S. Liu, Y.C. Shin, Additive manufacturing of Ti6Al4V alloy: A review, Mater. Des. 164 (2019) 107552. https://doi.org/10.1016/J.MATDES.2018.107552.

[12] P. Sun, Z.Z. Fang, Y. Zhang, Y. Xia, Review of the Methods for Production of Spherical Ti and Ti Alloy Powder, JOM. 69 (2017) 1853–1860. https://doi.org/10.1007/S11837-017-2513-5/TABLES/1.

[13] G. Lutjering, C. Williams, James, Titanium, 2nd Edition, 2nd Editio, Springer, New York, 2007. https://doi.org/https://doi.org/10.1007/978-3-540-73036-1.

[14] J.D. Cotton, R.R. Boyer, R.D. Briggs, R.G. Baggerly, C.A. Meyer, M.D. Carter, W. Wood, V. Li, X. Yao, Phase Transformations in Ti-5Al-5Mo-5V-3Cr-0.5Fe, (2007). https://www.researchgate.net/publication/284166885 (accessed May 26, 2022).

[15] M. Bönisch, M. Calin, L. Giebeler, A. Helth, A. Gebert, W. Skrotzki, J. Eckert, Composition-dependent magnitude of atomic shuffles in Ti-Nb martensites, J. Appl. Crystallogr. 47 (2014) 1374–1379. https://doi.org/10.1107/S1600576714012576.

[16] D. Banerjee, J.C. Williams, Perspectives on Titanium Science and Technology, Acta Mater. 61 (2013) 844–879. https://doi.org/10.1016/J.ACTAMAT.2012.10.043.

[17] T.S. Jang, D.E. Kim, G. Han, C.B. Yoon, H. Do Jung, Powder based additive manufacturing for biomedical application of titanium and its alloys: a review, Biomed. Eng. Lett. 10 (2020) 505–516. https://doi.org/10.1007/S13534-020-00177-2/FIGURES/8.

[18] M. Sarraf, E. Rezvani Ghomi, S. Alipour, S. Ramakrishna, N. Liana Sukiman, A state-of-the-art review of the fabrication and characteristics of titanium and its alloys for biomedical applications, Bio-Design Manuf. (2021). https://doi.org/10.1007/s42242-021-00170-3.

[19] T.S. Jang, D.E. Kim, G. Han, C.B. Yoon, H. Do Jung, Powder based additive manufacturing for biomedical application of titanium and its alloys: a review, Biomed. Eng. Lett. 10 (2020) 505–516. https://doi.org/10.1007/S13534-020-00177-2/FIGURES/8.

[20] A. Almeida, D. Gupta, C. Loable, R. Vilar, Laser-assisted synthesis of Ti-Mo alloys for biomedical applications, Mater. Sci. Eng. C. 32 (2012) 1190–1195. https://doi.org/10.1016/j.msec.2012.03.007.

[21] R. Davis, H.M. Flower, D.R.F. West, Martensitic transformations in Ti-Mo alloys, J. Mater. Sci. 14 (1979) 712–722. https://doi.org/10.1007/BF00772735.

[22] K. Ishida, Schaeffler-Type Phase Diagram of Ti-Based Alloys, Metall. Mater. Trans. A Phys. Metall. Mater. Sci. 48 (2017) 4990–4998. https://doi.org/10.1007/s11661-017-4218-3.

[23] J.D. Cotton, R.D. Briggs, R.R. Boyer, S. Tamirisakandala, P. Russo, N. Shchetnikov, J.C. Fanning, State of the Art in Beta Titanium Alloys for Airframe Applications, Jom. 67 (2015) 1281–1303. https://doi.org/10.1007/s11837-015-1442-4.

[24] P.J. Bania, Beta Titanium Alloys and Their Role in the titanium Industry, (1994) 16–19.

[25] R.P. Kolli, W.J. Joost, S. Ankem, Phase Stability and Stress-Induced Transformations in Beta Titanium Alloys, Jom. 67 (2015) 1273–1280. https://doi.org/10.1007/s11837-015-1411-y.

[26] C. Suryanarayana, F.H. Froes, R.G. Rowe, Rapid solidification processing of titanium alloys, Int. M. 36 (1991) 85–123.

[27] M. Morinaga, Y. Murata, H. Yukawa, Alloy design based on the DV-Xα cluster method, Springer Ser. Mater. Sci. 84 (2006) 23–48. https://doi.org/10.1007/3-540-31297-8_2.

[28] M. Li, X. Min, K. Yao, F. Ye, Novel insight into the formation of α″-martensite and ω-phase with cluster structure in metastable Ti-Mo alloys, Acta Mater. 164 (2019) 322–333. https://doi.org/10.1016/j.actamat.2018.10.048.

[29] M. Abdel-Hady, K. Hinoshita, M. Morinaga, General approach to phase stability and

elastic properties of β-type Ti-alloys using electronic parameters, Scr. Mater. 55 (2006) 477–480. https://doi.org/10.1016/J.SCRIPTAMAT.2006.04.022.

[30] M. Bignon, E. Bertrand, F. Tancret, P.E.J. Rivera-Díaz-del-Castillo, Modelling martensitic transformation in titanium alloys: The influence of temperature and deformation, Materialia. 7 (2019) 100382. https://doi.org/10.1016/j.mtla.2019.100382.

[31] P. Kofstad, High-temperature oxidation of titanium, J. Less-Common Met. 12 (1967) 449–464. https://doi.org/10.1016/0022-5088(67)90017-3.

[32] A.I. Kahveci, G.E. Welsch, EFFECT OF OXYGEN ON THE HARDNESS AND ALPHA/BETA PHASE RATIO OF Ti-6AI-4V ALLOY, 20 (1986) 1287–1290.

[33] M. Yan, W. Xu, M.S. Dargusch, H.P. Tang, M. Brandt, M. Qian, Review of effect of oxygen on room temperature ductility of titanium and titanium alloys, Http://Dx.Doi.Org/10.1179/1743290114Y.0000000108. 57 (2014) 251–257. https://doi.org/10.1179/1743290114Y.0000000108.

[34] M. Yan, W. Xu, M.S. Dargusch, H.P. Tang, M. Brandt, M. Qian, Review of effect of oxygen on room temperature ductility of titanium and titanium alloys, Powder Metall. 57 (2014) 251–257. https://doi.org/10.1179/1743290114Y.0000000108.

[35] Y. Xia, J. Zhao, Q. Tian, X. Guo, Review of the Effect of Oxygen on Titanium and Deoxygenation Technologies for Recycling of Titanium Metal, Jom. 71 (2019) 3209–3220. https://doi.org/10.1007/s11837-019-03649-8.

[36] H.R. Ogden, R.I. Jaffee, The Effects of Carbon, Oxygen, and Nitrogen on the Mechanical Properties of Titanium and Titanium Alloys, 1 (1955) 1–64. https://doi.org/doi:10.2172/4370612.

[37] Z. Liu, G. Welsch, Literature Survey on Diffusivities of Oxygen, Aluminum, and Vanadium in Alpha Titanium, Beta Titanium, and in Rutile, Metall. Trans. A 1988 194. 19 (1988) 1121–1125. https://doi.org/10.1007/BF02628396.

[38] M. Yan, M.S. Dargusch, T. Ebel, M. Qian, A transmission electron microscopy and three-dimensional atom probe study of the oxygen-induced fine microstructural features in as-sintered Ti–6Al–4V and their impacts on ductility, Acta Mater. 68 (2014) 196–206. https://doi.org/10.1016/J.ACTAMAT.2014.01.015.

[39] Y. Zheng, R. Banerjee, Y. Wang, H. Fraser, D. Banerjee, Pathways to Titanium Martensite, Trans. Indian Inst. Met. 75 (2022) 1051–1068. https://doi.org/10.1007/S12666-022-02559-9/FIGURES/19.

[40] M. Li, X. Min, K. Yao, F. Ye, Novel insight into the formation of α″-martensite and ω-phase with cluster structure in metastable Ti-Mo alloys, Acta Mater. 164 (2019) 322–333. https://doi.org/10.1016/J.ACTAMAT.2018.10.048.

[41] M. Bignon, E. Bertrand, P.E.J. Rivera-Díaz-del-Castillo, F. Tancret, Martensite formation

in titanium alloys: Crystallographic and compositional effects, J. Alloys Compd. 872 (2021) 159636. https://doi.org/10.1016/J.JALLCOM.2021.159636.

[42] M. Bignon, E. Bertrand, P.E.J. Rivera-Díaz-del-Castillo, F. Tancret, Martensite formation in titanium alloys: Crystallographic and compositional effects, J. Alloys Compd. 872 (2021) 159636. https://doi.org/10.1016/j.jallcom.2021.159636.

[43] S. Banerjee, R. Tewari, G.K. Dey, K. Urban, Omega phase transformation – morphologies and mechanisms, 97 (2006).

[44] H.D. Carlton, K.D. Klein, J.W. Elmer, Evolution of microstructure and mechanical properties of selective laser melted Ti-5Al-5V-5Mo-3Cr after heat treatments, Sci. Technol. Weld. Join. 24 (2019) 465–473. https://doi.org/10.1080/13621718.2019.1594589/FORMAT/EPUB.

[45] J.C. Sabol, C.J. Marvel, M. Watanabe, T. Pasang, W.Z. Misiolek, Confirmation of the ω-phase in electron beam welded Ti–5Al–5V–5Mo–3Cr by high-resolution scanning transmission electron microscopy: An initial investigation into its effects on embrittlement, Scr. Mater. 92 (2014) 15–18. https://doi.org/10.1016/J.SCRIPTAMAT.2014.08.003.

[46] S. Ankem, C.A. Greene, Recent developments in microstructure/property relationships of beta titanium alloys, Mater. Sci. Eng. A. 263 (1999) 127–131. https://doi.org/10.1016/S0921-5093(98)01170-8.

[47] B.S. Hickman, The Formation of Omega Phase in Titanium and Zirconium Alloys: A Review, J. Mater. Sci. 4 (1969) 554–563.

[48] J.C. Williams, B.S. Hickman, D.H. Leslie, The effect of ternary additions on the decompositon of metastable beta-phase titanium alloys, Metall. Trans. 2 (1971) 477–484. https://doi.org/10.1007/BF02663337.

[49] M.J. Lai, T. Li, F.K. Yan, J.S. Li, D. Raabe, Revisiting ω phase embrittlement in metastable β titanium alloys: Role of elemental partitioning, Scr. Mater. 193 (2021) 38–42. https://doi.org/10.1016/j.scriptamat.2020.10.031.

[50] W. Kurz, P. Gilgien, Selection of microstructures in rapid solidification processing, Mater. Sci. Eng. A. 178 (1994) 171–178. https://doi.org/10.1016/0921-5093(94)90538-X.

[51] D.M. Stefanescu, Science and engineering of casting solidification: Third edition, 2015. https://doi.org/10.1007/978-3-319-15693-4.

[52] P.K. Galenko, D.A. Danilov, Linear morphological stability analysis of the solid-liquid interface in rapidsolidification of a binary system, Phys. Rev. E - Stat. Physics, Plasmas, Fluids, Relat. Interdiscip. Top. 69 (2004) 14. https://doi.org/10.1103/PhysRevE.69.051608.

[53] M.J. Aziz, Model for solute redistribution during rapid solidification, J. Appl. Phys. 53

(1982) 1158–1168. https://doi.org/10.1063/1.329867.

[54] M.J. Aziz, T. Kaplan, Continuous Growth Model for Interface, Acta Metall. Mater. 36 (1988) 2335–2347.

[55] S.L. Sobolev, Local non-equilibrium diffusion model for solute trapping during rapid solidification, Acta Mater. 60 (2012) 2711–2718. https://doi.org/10.1016/j.actamat.2012.01.036.

[56] R. Trivedi, W. Kurz, Solidification microstructures: A conceptual approach, Acta Metall. Mater. 42 (1994) 15–23. https://doi.org/10.1016/0956-7151(94)90044-2.

[57] M.J. Kaufman, M. Ellner, H.L. Fraser, Constitution of an Al-37.5Ge splat quenched foil: Implications on nucleation kinetics, Scr. Metall. 20 (1986) 125–128. https://doi.org/10.1016/0036-9748(86)90225-5.

[58] P.G. Boswell, G.A. Chadwick, The Grain Size of Splat-Quenched Alloys, Scr. Metall. 11 (1977) 459–465.

[59] D. Turnbull, Formation of Crystal Nuclei in Liquid Metals, Heterog. Nucleation J. Chem. Phys. 21 (1950) 198. https://doi.org/10.1063/1.1699435.

[60] J.D. Hunt, Steady state columnar and equiaxed growth of dendrites and eutectic, Mater. Sci. Eng. 65 (1984) 75–83. https://doi.org/10.1016/0025-5416(84)90201-5.

[61] M. Gäumann, C. Bezençon, P. Canalis, W. Kurz, Single-crystal laser deposition of superalloys: Processing-microstructure maps, Acta Mater. 49 (2001) 1051–1062. https://doi.org/10.1016/S1359-6454(00)00367-0.

[62] M. Gäumann, R. Trivedi, W. Kurz, Nucleation ahead of the advancing interface in directional solidification, Mater. Sci. Eng. A. 226–228 (1997) 763–769. https://doi.org/10.1016/S0921-5093(97)80081-0.

[63] W. Kurz, R. Trivedi, Rapid solidification processing and microstructure formation, Mater. Sci. Eng. A. 179–180 (1994) 46–51. https://doi.org/10.1016/0921-5093(94)90162-7.

[64] J.M. Vitek, A. Dasgupta, S.A. David, Microstructural modification of austenitic stainless steels by rapid solidification, Metall. Trans. A 1983 149. 14 (1983) 1833–1841. https://doi.org/10.1007/BF02645553.

[65] R.C. Ruhl, Cooling rates in splat cooling, Mater. Sci. Eng. 1 (1967) 313–320. https://doi.org/10.1016/0025-5416(67)90013-4.

[66] Y. Inokuti, B. Cantor, The formation of martensite in splat-quenched Fe-Mn and Fe-Ni-C alloys, J. Mater. Sci. 1977 125. 12 (1977) 946–958. https://doi.org/10.1007/BF00540977.

[67] C. Hayzelden, J.J. Rayment, B. Cantor, Rapid solidification microstructures in austenitic Fe-Ni alloys, Acta Metall. 31 (1983) 379–386. https://doi.org/10.1016/0001-

6160(83)90215-8.

[68] S. Krishnamurthy, H. Jones, F.H. Froes, Solidification microstructures of hammer and anvil splat-quenched binary titanium alloys, J. Mater. Sci. Lett. 7 (1988) 1138–1141. https://doi.org/10.1007/BF00720858.

[69] H. Jones, Cooling rates during rapid solidification from a chill surface, Mater. Lett. 26 (1996) 133–136. https://doi.org/10.1016/0167-577X(95)00213-8.

[70] R.C. Ruhl, Cooling rates in splat cooling, Mater. Sci. Eng. 1 (1967) 313–320. https://doi.org/10.1016/0025-5416(67)90013-4.

[71] M.G. Scott, The role of melt superheat in splat-quenching, J. Mater. Sci. 1975 102. 10 (1975) 269–273. https://doi.org/10.1007/BF00540350.

[72] P. Predecki, A. MULLENDO, N.J. Grant, A study of splat cooling technique., Trans. Metall. Soc. AIME. 233 (1965) 1581.

[73] S.H. Whang, Review Rapidly solidified titanium alloys for high-temperature applications, J. Mater. Sci. 21 (1986) 2224–2238.

[74] F.H. Froes, R.G. Rowe, RAPIDLY SOLIDIFIED TITANIUM, Mater. Res. Soc. (1986).

[75] H. Jones, Microstructure of rapidly solidified materials, Mater. Sci. Eng. 65 (1984) 145–156. https://doi.org/10.1016/0025-5416(84)90208-8.

[76] J.D. Roehling, A. Perron, J.L. Fattebert, T. Haxhimali, G. Guss, T.T. Li, D. Bober, A.W. Stokes, A.J. Clarke, P.E.A. Turchi, M.J. Matthews, J.T. McKeown, Rapid Solidification in Bulk Ti-Nb Alloys by Single-Track Laser Melting, Jom. 70 (2018) 1589–1597. https://doi.org/10.1007/s11837-018-2920-2.

[77] S. Suwarno, J.K. Solberg, J.P. Maehlen, B. Krogh, V.A. Yartys, The effects of rapid solidification on microstructure and hydrogen sorption properties of binary BCC Ti–V alloys, J. Alloys Compd. 582 (2014) 540–546. https://doi.org/10.1016/J.JALLCOM.2013.08.077.

[78] T.F. Broderick, A.G. Jackson, H. Jones, F.H. Froes, The effect of cooling conditions on the microstructure of rapidly solidified Ti-6Al-4V, Metall. Trans. A. 16 (1985) 1951–1959. https://doi.org/10.1007/BF02662396.

[79] A.M. Birt, V.K. Champagne, R.D. Sisson, D. Apelian, Microstructural analysis of Ti-6Al-4V powder for cold gas dynamic spray applications, Adv. Powder Technol. 26 (2015) 1335–1347. https://doi.org/10.1016/j.apt.2015.07.008.

[80] M. V. Kral, W.H. Hofmeister, J.E. Wittig, Precipitate crystallography and morphology in undercooled, rapidly solidified titanium rare earth alloys, Scr. Mater. 36 (1997) 157–163. https://doi.org/10.1016/S1359-6462(96)00364-8.

[81] T.Z. Kattamis, W.F. Brower, R. Mehrabian, Microstructure and segregation in splat-cooled iron-nickel alloy, J. Cryst. Growth. 19 (1973) 229–236. https://doi.org/10.1016/0022-0248(73)90044-4.

[82] S. Krishnamurthy, A.G. Jackson, H. Jones, F.H. Froes, Beta-Eutectoid Decomposition in Rapidly Solidified Titanium-Nickel Alloys, Metall. Mater. Trans. A. 19 (1988) 23–33.

[83] R. Ray, B.C. Giessen, N.J. Grant, The constitution of metastable titanium-rich Ti-Fe alloys:An order-disorder transition, Metall. Trans. 3 (1972) 627–629. https://doi.org/10.1007/BF02642743.

CHAPTER 2 : SPLAT QUENCHING AS A HIGH THROUGHPUT RAPID SOLIDIFICATION TESTING METHOD FOR DEVELOPING ADDITIVE MANUFACTURING ALLOYS

C.J. Williamson[a], A. Deal[b], B. Brown[b], L. Nastac[a], L.N. Brewer[a]

[a] Department of Metallurgical and Materials Engineering, The University of Alabama, Tuscaloosa, AL 35487, USA

[b] Department of Energy's National Security Campus, Honeywell Federal Manufacturing & Technologies, Botts Road, Kansas City, MO 14520, USA

The potential of splat quenching as a rapid solidification technique for use in high throughput screening for additive manufacturing alloy design is evaluated. Samples were made using known alloys (SS316, In625, Ti-5553) to evaluate and establish the microstructures developed for each system as well as the predicted cooling rates. The samples are inductively heated and levitated prior to being struck between two platens that produce a high contact pressure and a thin sample resulting in cooling rates on the order of 10^6-10^7 °K/s. Process parameters were evaluated with analytical models as well as FLUENT computational fluid dynamics simulations to provide a process window and to elucidate the relevancy of process parameters such as substrate material, melt superheat, and platen velocity on the resulting solidification parameters. The thickness of the splat is the key controlling factor for varying the average cooling rate experienced by the splat quenched sample. The splat thickness can be controlled by platen velocity, melt superheat, as well as the feedstock volume, but platen velocity has the largest and most consistent influence on splat thickness for a given material volume. The

splat quenching techniques can reach regions of rapid solidification space that meet and exceed laser and electron beam techniques across the sample. The results of the study provide a useful foundation in understanding the splat quenching technique and its potential as an alloy design tool.

2.1.0 Introduction

Additive manufacturing (AM) has continued to develop through the 21st century as a solution to far-ranging manufacturing problems such as logistical strain in acquiring OEM components to providing lightweighting possibilities and component designs that are not possible with other manufacturing techniques. As the field of AM continues to mature, the ability to create alloys for the intended use in these processes is needed as the original set of alloys and their compositional specifications are reused from the common structural alloys created for traditional processing routes such as Ti-6Al-4V, SS316, and Inconel 625 [1]. These alloys were originally designed and developed for the process of casting, rolling, and general production into the various feedstock that can then be machined components, however the AM processes have fundamental differences that make the alloy design choices different than for traditional processing routes.

In fusion-based AM, the material is typically melted and experiences rapid solidification that results in thermal gradients and solidification velocities that decrease segregation and promote columnar grains. The result is that limitations put on alloys to control properties such as hot workability and intermetallic formation during casting are no longer a limiting factor for alloy design. However, AM has inherent difficulties in promoting recrystallization that could be easily achieved through rolling and processing of billet material. As such, AM generates near-net shape parts columnar grained, solidification microstructures, and there can be difficulty

producing equiaxed grains after solidification. The changes in processing route then by design motivate changes in the alloy composition that have the potential to result in the highest quality component possible. An example is the addition of iron or nickel into titanium alloys that is widely seen as a negative in traditional manufacturing due to the high propensity for segregation and the possibility for intermetallic formation when cast, but these additions can promote equiaxed grains in additive processes [2]. In spite of the continuing need for the growth and development for alloys designed for AM applications, there is a lack of testing methods that can act as a high throughput method for sampling the rapid solidification response of new and different alloys. The traditional method of creating components and testing is difficult due to the significant cost and time required for powder production. For a technique to be high-throughput it needs to be able to quickly create samples, require minimal feedstock, and preferentially be immediately available for characterization.

With these constraints in mind, twin hammer splat quenching (SQ) is a technique that has been used to study rapid solidification for alloy design with little material needed and with as-produced samples easily used for material characterization [3–6]. The technique relies on inductive levitation and heating of a pre-alloyed sample in an argon partial pressure atmosphere. When the sample is heated to the desired superheat temperature, as read by a two color pyrometer, the coil is deenergized, resulting in the melt falling and coming into contact with two platens that are electromagnetically fired at the melt (Figure 2.1). The resulting collision causes the molten material to flatten into a disk on the order of 50-100 μm thick and to reach cooling rates on the order of 10^6 to 10^7 K/s and higher [7]. The usefulness of the technique relies upon the ease of sample creation allowing for alloy testing across numerous areas of interest such as binary alloys [8,9] or for examining compositional fluctuations in a complex structural alloys

such as SS316 to validate compositional ranges [10]. The use of the technique has been underutilized in the wake of the need for a method to test alloys easily and quickly in the rapid solidification regimes experienced by alloys during the process of AM or laser welding.

Twin hammer splat quenching, similarly, referred to as hammer and anvil splat quenching, as a technique has been used since the latter half of the 20th century into modern day as a way to study alloy responses at cooling rates and solidification velocities that are difficult if not impossible to reach otherwise. The process is a modification based on other splat cooling techniques that fire molten metal at a chilled planar substrate[5,11,12]. These processes are very similar in many ways to the thermal spray process and share many similarities of heat transfer and droplet deformation[4]. Evolution of these processes later resulted into the twin hammer splat quenching and melt spin techniques [13]. The introduction of the twin hammers allowed for a higher cooling rates and foil uniformity across the splat quenched sample. The technique has seen several attempts to provide analytical and numerical calculations of the cooling rates expected during the process, however the complications behind the fluid flow and melt properties result in there being a lack of analytical models to estimate cooling rates [6,14]. In spite of this difficulty, SQ has found significant use in the study of martensite formation[15], bulk metallic glasses[16,17], and microstructure formation[8,9,18,19]. As such, splat quenching is historically situated as a tool to meet a current need for high throughput rapid solidification testing in the wake of RS techniques such as additive manufacturing continue growing.

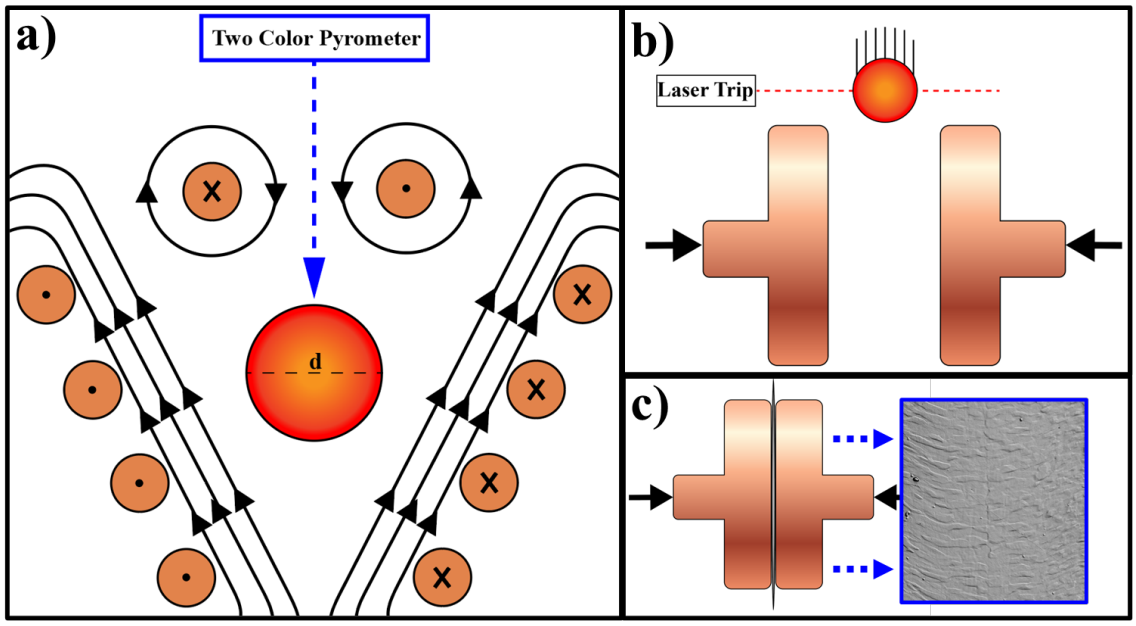

Figure 2.1 Graphical representation of the splat quenching process from (a) the levitation and heating of a ball of material as well as (b) the falling and activation of the platens to the (c) collision of the platens resulting in a rapidly solidified foil.

As the potential of splat quenching as a high throughput rapid solidification testing method is rising, this paper is focused on offering experimental data on the key parameters that effect the cooling rate of splat quenching such as platen material, melt superheat, and melt properties coupled with analytical heat transfer equations that develop a window of cooling rates achievable for splat quenching. The goal of this work is to provide an immediate comparison between splat quenching and other rapid solidification techniques such as fusion based AM and welding in terms of solidification parameters and cooling rate as well as offer insight into the controlling factors that can be easily altered in the splat quenching technique to probe a range of cooling rate regimes.

2.2.0 Experimental Procedures

Alloy samples used for this study range from arc melted buttons (Ti-5553) to material cut from commercially available feedstock (In625 and SS316). The samples were cut into cubes roughly 4 mm length on a side, approximately 100 mg, using a wire EDM. The samples were then ground to remove the EDM recast layer and cleaned with ethanol. The cleaned material was then placed on a boron nitride crucible in the Edmund Bühler splat quenching unit. The chamber was pumped down to 10^{-4} mbar and cycled with argon three times to provide an low oxygen environment to reduce interstitial pickup during heating. On the final backfill, the chamber was filled to 700 mbar to minimize solute evaporation. The induction coil was then energized, levitating the sample and heating to the melting temperature. The sample is allowed to fully melt and reach a desired superheat temperature as measured by a two color pyrometer (Fluke Model:E1RH-F0-L0-0) in around fifteen to sixty seconds depending on the response of the particular alloy to the magnetic field. The sample is then dropped, crossing a laser line that activates the pistons to fire in the range of 2-5 m/s set by a voltage applied to the capacitors used to launch the platens.

The platens were polished in three different conditions from 600p grinding (26 μm) , 1200p grinding (15 μm), and 1 μm diamond solution polishing. The surface roughness of the platens was measured with a KLA Tencor surface profilometer (Model: D-500) across a 1.0 mm distance. The standard platen was made from copper with a 1200p (15 μm roughness) surface finish. Additional platen materials were used, namely commercially pure titanium, stainless steel 316, and zirconia. Platen velocity was also varied from 2.25 m/s to 4.5 m/s, which was found to be the operational range for the current splat quenching model with the measured variation in velocity being ± 0.15 m/s. The platen velocity was controlled by the voltage applied to a

capacitor used to fire the platens at the molten droplet. To measure the velocity as well as image the falling droplet, high speed videography was used with a Phantom v611 model camera at 41k frames per second rate. The platens were fired five times at the applied voltages to calculate the average velocity. The average velocity was observed to linearly vary with applied voltage with the variation in platen velocity measured to be below 5% for the typical firing velocity of 3.5 m/s. Variation in superheat was only preformed for the Ti-5553 alloy due to the ease of controlling the drop temperature in the titanium alloy. Superheat was controlled by changing the induction coil current to stabilize the molten sphere at the desired temperature.

Representative samples were chosen for various SQ conditions and were then cross sectioned and mounted. Etching was done for the stainless steel and titanium samples using electrolytic etching with nitric acid and Kellers reagent respectively. SEM microscopy was conducted to characterize grain and cell sizes, which in turn were used as an indicative feature for cooling rate. Electron back scatter diffraction (EBSD) was conducted on several select samples to investigate the grain sizes and orientations of the etched material. Both the SEM microscopy and EBSD were conducted on a JEOL 7000 with an Oxford HKLNordlys EBSD detector and processed using Aztec processing software. The EBSD maps were across the entire through-thickness of the splats (50-100 μm) with a step size of 150 nm. The inverse pole figure maps have the grain orientations in the splat quenched direction (vertical in the maps).The heat transfer simulations were conducted in FLUENT with a 2-D cross section of the melt that was mirrored along the midline of the splat for the Ti-5553 and SS316 materials. The latent heat for Ti-5553 and SS16 were 3.5 10^5 and 2.72 10^5 J/kg respectively with a 30°C and 20°C solidification interval for the alloys. The simulated melt has an initial temperature of 50°C above the liquidus temperature with the cooling rate being calculated by the time interval spent between

the liquidus and solidus temperature. The heat transfer was dominated by conduction through the substrate with the heat transfer coefficient being estimated through analytical models.

2.3.0 Calculated Results

2.3.1 Understanding the Contact Pressure Effect on Cooling Rate

The contact between the melt and platens is the dominant mechanism for heat transfer during splat quenching and is needed to be understood prior to any prediction of solidification condition. The contact pressure of a molten sphere impinging on a cooler flat substrate is a well-known problem and has several methods for prediction [20,21]. The model for a single impact of a droplet from thermal spray, Eqn 1, was used in the current study as it incorporates the dynamic nature of the melt deformation event to provide an understanding of the evolution in contact pressure [20]. For the initial contact, there is an analytical solution available based on drop-to solid collisions that finds the impact pressure (p_0) is related to the density of the molten liquid (ρ) and the square of the impact velocity (V_0), and a constant $C_0 = 3.75$ that is used as a fitting function for thermal spray [20].

$$p_0 = C_0 \rho V_0^2 \quad (1)$$

The value of predicted impact pressure for three metals at varying velocities in Table 1. The pressure in this case increases as a function of platen velocity as well as density of the alloy. While the density cannot be meaningfully changed for a given material, the change in contact pressure results in materials such as Inconel or steels having in inherently higher impact pressure then aluminum or titanium alloys that can be accounted for with changes in platen speed if desired.

Table 2.1 Thermophysical properties calculated from Thermocalc and the associated pressure resulting from nominal platen velocities.

Material	Density near T_m (kg/m^3)	Surface Tension (J/m^2)	Conductivity (W/m°K)	Contact Pressure (MPa)		
				V=1.5 m/s	V=3.5 m/s	V=5.0 m/s
Ti-5553	4315	1.50	29.00	0.036	0.19	0.40
SS316	7340	1.55	36.08	0.062	0.32	0.68
IN625	7600	1.03	33.58	0.064	0.32	0.71

Beyond the initial impact, there is a change in the pressure as the molten splat flattens on the substrate, graphically seen in Figure 2.3. The pressure at the center of the splat decreases with time and the footprint of the splat widens. The spreading of the droplet and drop in pressure results in everything beyond twice the initial radius of the droplet (displayed as 2d in Figure 2.2) effectively having no pressure ensuring contact between the melt and the platen beyond this radius prior to the platens colliding. This change can be seen qualitatively in the face of the splat quenched sample where there is a change in the surface quality, shown pictorially in Figure 2.2b. From literature, the gradient in the pressure equalizes on the order of a 1 ms, as seen in estimated pressure data displayed in Figure 2.3, meaning that even though the molten droplet is splatted into a foil on the order of 1 ms the contact pressure in the center of the splat quenched sample has dropped significantly [20]. In the case of thermal spray, the impact of melt onto substrate is the only impact, but in splat quenching there is the impingement of the melt onto substrates followed by the collision of the platens with the liquid between. Of interest in trying to understand the process, the contact time between the platens and is dominated by this impingement stage where the only pressure enforcing contact between the melt and the platen is from melt deforming upon the platen. The entire interaction time between the molten material and the platens is on the order of 1.2 ms with the actual collision of the platens and resulting solidification occurring in less than 0.47 ms. Meaning that depending on the platen velocity that

60% of the splat quenching time is at this lower contact pressure that is controlled by the melt flow over the platen rather than the jetting that occurs due to liquid instability as the platens collide[22]. While the thickness of a splat in thermal spray is dominated by a singular impact event of the liquid hitting a substrate, the combination of two nearly simultaneous impacts, varying orders of magnitude of pressure, and liquid confinement between the two platens mean that the prediction of thickness in splat quenched samples is fairly complex.

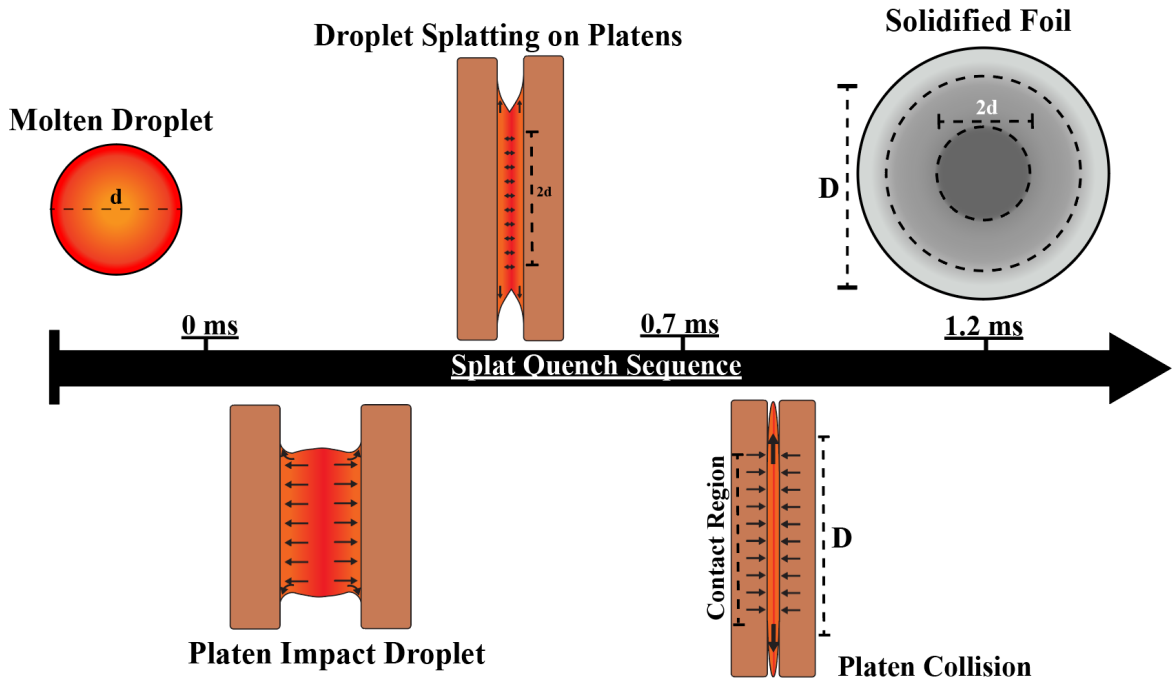

Figure 2.2 Pictorial representation of splat quenching timeline highlighting that 60% of time spent in contact with the platen is prior to platen collision. The splatting event is only slightly over 1.2 ms from contact to completion with less than half of the time spent during the high pressure collision between the projectile platens

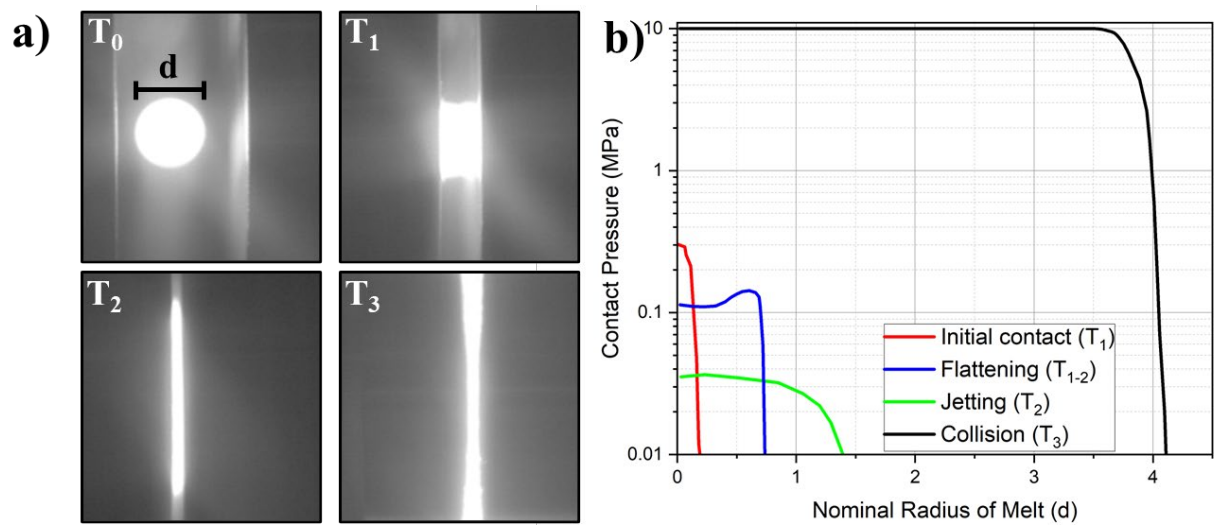

Figure 2.3 (a) Images from high speed videography of the molten ball of material being impinged by the copper platens before a final collision resulting in material jetting. (b) Nominal pressure distribution demonstrating the drop in pressure of the original impingement period and the increase in contact pressure resulting from the final collision of the platens [20].

Following the flattening of the molten sphere of material, the platens collide and impart a higher pressure on the molten material that further enforces the thermal contact between melt and platen. Additionally, using high speed videography the time for the platen to go from nominal velocity to stopped from collision can be estimated and along with the mass of the pistons and area of splat in contact with the platens can be used to predict the contact pressure of the collision. An average impact force (F_{avg}) can then be estimated using Eqn. 2 with the mass of the platen arms launched (m=0.6 kg) across a velocity ranging from 2.5 to 5 m/s. The distance the platen stops (d) can be seen in the high speed videography to be in the final stages of splat deformation on the range of the final splat thickness (50-100 µm).

$$F_{avg} = \frac{mV_0^2}{2d} \quad (2)$$

For a velocity (V_0)range from 2.5-5 m/s the associated pressure resulting from a 15 mm diameter splat ranges from 1.69-10.6 MPa that are an order of magnitude higher pressures than what develops prior to the platen collision. While a simple estimation, this expression allows for the conclusion that the heat transfer for the bulk of the splat quenched sample is primarily controlled by the collision between the platens and the resulting pressure.

The result of the dynamic process resulting from splat quenching means that there are significant differences in heat transfer and resultingly the solidification microstructure across the splat radius. The center ($0 < r < 2d$) sees a significant amount of cooling occurring prior to the platens colliding. While the edges ($2d < r < D$) see a higher quality contact with the platen and result in higher cooling rates. The molten material is assumed to be fully liquid until splatted into a foil thereby allowing for the thermal gradient to form from the substrate surface to the midline [5]. The result is that though the contact pressure during the initial stage of the deformation is affected by the material properties of the molten material, the contact pressure throughout the bulk of the platen compression is a variable of the force of the platens and the geometry of the material in contact with the platen. Examination of the splat demonstrates the thickest portion of the splat occurs at the center ($r< 2d$) with a drop to a uniform thickness for material only coming into contact with the platens during splatting ($d<r<D$). The difference in thickness and in solidification structure can be seen in Figure 2.4. The uniform thickness region at the edge of the can be assumed to be to have all been in contact with the platens during impact, though the flash farther out ($r > D$) is the result of fluid instability of the jetted material caused by the platen collision [22].

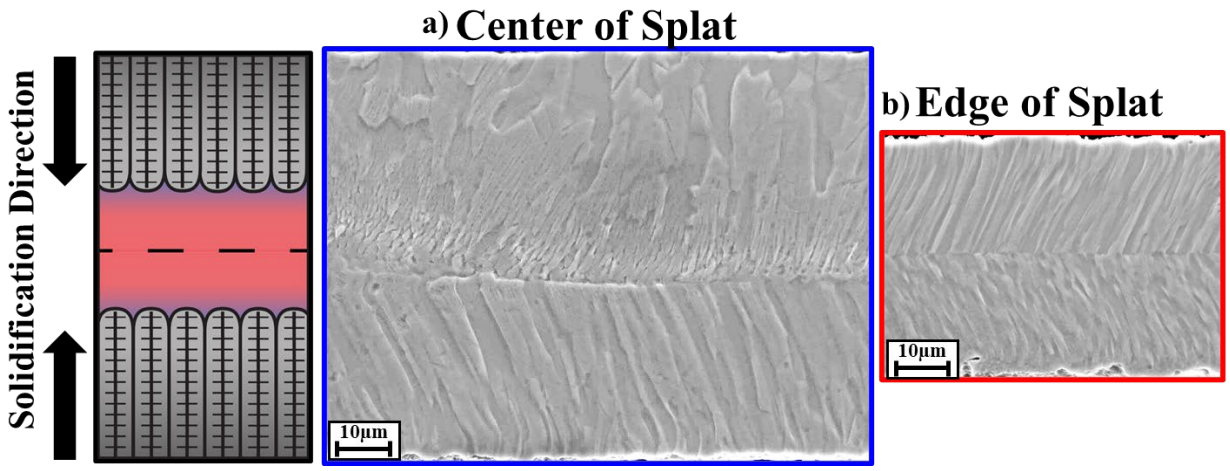

Figure 2.4 Micrographs of etched Ti-5553 splat quench cross section demonstrating the morphological and thickness differences between the thicker central region of the splat and the edge of the splat quenched sample. (Note that both images have the same scale bar.)

2.3.2 Modeling Heat Transfer Coefficient

In a substrate cooling processes such as splat quenching, the interfacial heat transfer coefficient is the dominant mechanism for cooling and thereby needs to be estimated to understand the process at any level. There are inherent difficulties in experimentally measuring and correlating a value of interfacial heat transfer coefficient due to the rapid cooling resulting in a small time window that is not easily viewable. These same problems also occur in processes such as thermal spray or casting where not all variables are easily viewable. As such, calculated values of interfacial heat transfer coefficient for splat quenching range quite significantly from 10^5 to 10^7 W/m^2°K[4,7,23]. However, the models developed for other processes allow for an estimation that, with reasonable assumptions, can provide a tool for understanding what experimental parameters the largest effect on the SQ have cooling rate.

The parameters that can affect the heat transfer from a molten metal to a substrate are quite varied and are a function of processing conditions such as the solidification time and

contact pressure. Surface roughness inherently plays an important role in all the heat transfer models as the contact between melt and substrate are defined by the shape of surface asperities and contact angle between the melt and substrate. The contact angle between a molten metal and a metallic substrate is difficult to find in literature and can vary significantly due to the formation of intermetallics, presence of oxides, roughness of substrate, dissolution of the substrate into the melt, atmosphere, and substrate temperature [24]. Some models assume that the solidification is rapid enough that the contact angle can effectively be captured by assuming a wetting angle of 180° [25] while others looking at slower time frames such as casting assume lower wetting angles [21,26]. To that end, a model developed by Xue et al. [25] was selected that was developed for thermal spray applications and has several key assumptions that make the model easy to implement, while providing information for understanding splat quenching. Firstly, the contact angle between the melt and substrate is assumed to be 180° that is seen to match the trend seen in measured contact angle between copper and titanium at low interaction times [24] as well as simplifying the surface asperities into a series of half-cylinders, illustrated in Figure 2.5. The model (Eqn. 3) is a relationship between the height of asperities on the platen (R_a) and the physical properties of surface tension (σ) and thermal conductivity (k_w), Table 1. Also included is the term for the liquid pressure (ρ_c) that is the combination of the liquid metal contact pressure as well as the contact pressure of the platens hitting. The thermal conductivity was taken as the average of the melt and platen at the melting temperature of the splatted material.

$$h = \frac{k_w \rho_c}{R_a[\rho_c + \pi\sigma/(4R_a)]} \quad (3)$$

The use of this model allows for interpretation of the parameters that offer the highest degree of change in the splat quenching process such as contact pressure, platen roughness, platen material, and material properties of the molten material. The plotted differences of heat

transfer coefficient can be seen below, Figure 2.5. Pressure increases result in a higher surface area for heat transfer as the molten metal is forced into the asperities on the platen therefore an increase in heat transfer at higher contact pressures. Beyond surface roughness, comparing copper, stainless steel, and zirconia substrates gives a wide range on what the change in thermal conductivity can be expected to do. Thermal conductivity results in a linear change in the h value so thereby a change from copper (182 W/m°K) to stainless steel (36 W/m°K) only brings about a change on the order of half a magnitude while the use of an insulator such as zirconia (1.2 W/m°K) leads to a drop of over two order of magnitude in h. The effect of a change in the material splatted on the heat transfer coefficient, h, can also be estimated with both the surface tension of the melt and the change in thermal conductivity of the interface being affected. Comparing three structural alloys at their melting temperatures demonstrates that the change is mostly dominated by a difference in surface tension. The change in surface tension, Figure 2.5d, leads to a difference in the heat transfer coefficient at low pressures while the plateau at higher pressure is fairly similar. The surface tension as a material property can be used in applications such as casting to compare the ease of penetration of the liquid metal around asperities. Therefore at high pressures the difference between the alloys is effectively eliminated due to the forced contact of the liquid with the substrate material as seen in Figure 2.5d, where h is constant at 10MPa with surface tension variation from 0.25-2.0 J/m^2. Plotting of these changing variables lead to an understanding that nominal changes in splat material and surface roughness can offer some control on the heat transfer coefficient but that controlling the pressure and substrate material changes have the possibility to have a much larger effect on the heat transfer coefficient.

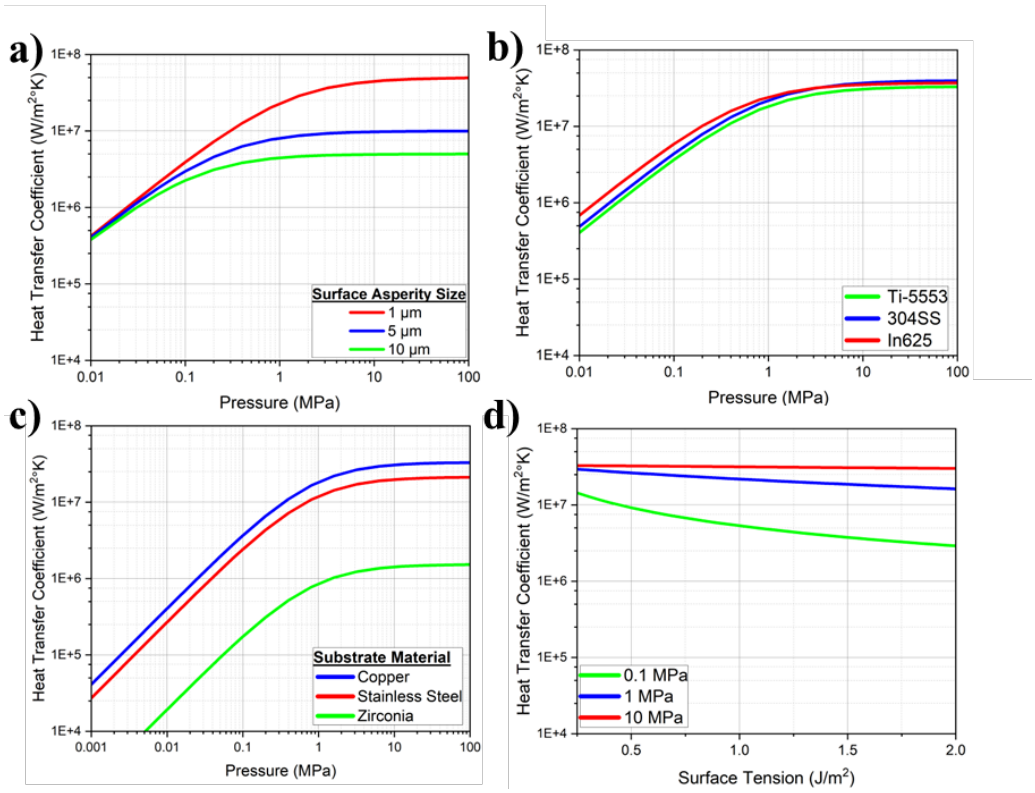

Figure 2.5 Graphs of estimated heat transfer coefficients as a function of (a) surface roughness, (b) splatted material, (c) platen material, and (d) surface tension.

With a way to estimate the heat transfer coefficient of the SQ process, the modeling of the cooling rate can be done to provide estimates on the cooling rate to provide a way to estimate the changes to the processing parameters. Work by Ruhl et al. looked into simple calculations for estimating the splat quenching process as both ideal cooling and Newtonian cooling. The Biot number, $\frac{hd}{k_s}$,can be used as an estimate to understand ability for a gradient to form during heat transfer, where d is the half thickness of the sample and k_s is the thermal conductivity of the splatted material. Ruhl et al. uses values of 0.015 and 30 as boundaries for Newtonian cooling (no formation of a thermal gradient) and ideal cooling that is completely defined by the thermal gradient formed in the sample respectively. This relationship makes physical sense as a thicker

sample or lower thermal conductivity of the fluid would promote a higher thermal gradient in the material while a lower heat transfer coefficient would limit the heat flow and result in a more homogeneous temperature profile in the sample. The Biot number then is a relationship to help describe the type of conduction heat transfer that develops in a sample. Due in part to the small 50-100 μm thickness of the samples and the large heat transfer coefficient created by the platen collision, the Biot number places the splat quenching process as an intermediate heat transfer problem with higher pressures and subsequently a higher interfacial heat transfer coefficient pushing the heat transfer into a fully ideal cooling regime. This relationship means that during the deformation of the melt, the heat transfer is not entirely gradient controlled but that after the platens collide all heat transfer is interfacial controlled. An additional factor in splat quenching is the thickness of the splats that has been related to numerous values such as surface tension, viscosity, wetting of the substrate [27–29], critical angle for jetting to occur[30], and even a function of solidification prior to the collision of the platens [18].

2.4.0 Experimental Results

2.4.1 Material Properties Effect on Splatted Samples

The material properties of the splatted material have an effect on the splat thickness with surface tension and density both found to affect the final thickness and resulting change the cooling rate. The initial collision between the molten droplet and the two impeding platens is controlled by the velocity of the platens and the density of the molten material and as such when all conditions were held constant the measured thickness was 100.3 μm, 54.5 μm, and 42.5 μm for the Ti-5553, SS316, and In625 respectively, seen in Figure 2.6. The Ti-5553 and SS316 have a 45.7% difference in splat thickness and a 41.2% difference in densities, indicating that the

density of the material does have a strong correlation to the variation in splat thickness. However, comparing the SS316 and In625 is less clear with the two alloys having only a 3.5 % difference in densities but a 23.8% difference in splat thickness. This difference is likely due to the 33.5% decrease in surface tension between the two alloys, while the surface tension is nearly identical between the stainless steel and titanium alloy. So, while the densities do have an inherent effect on thickness the melt flow and subsequent final splat thickness are a more complicated result with surface tension effects coming into play.

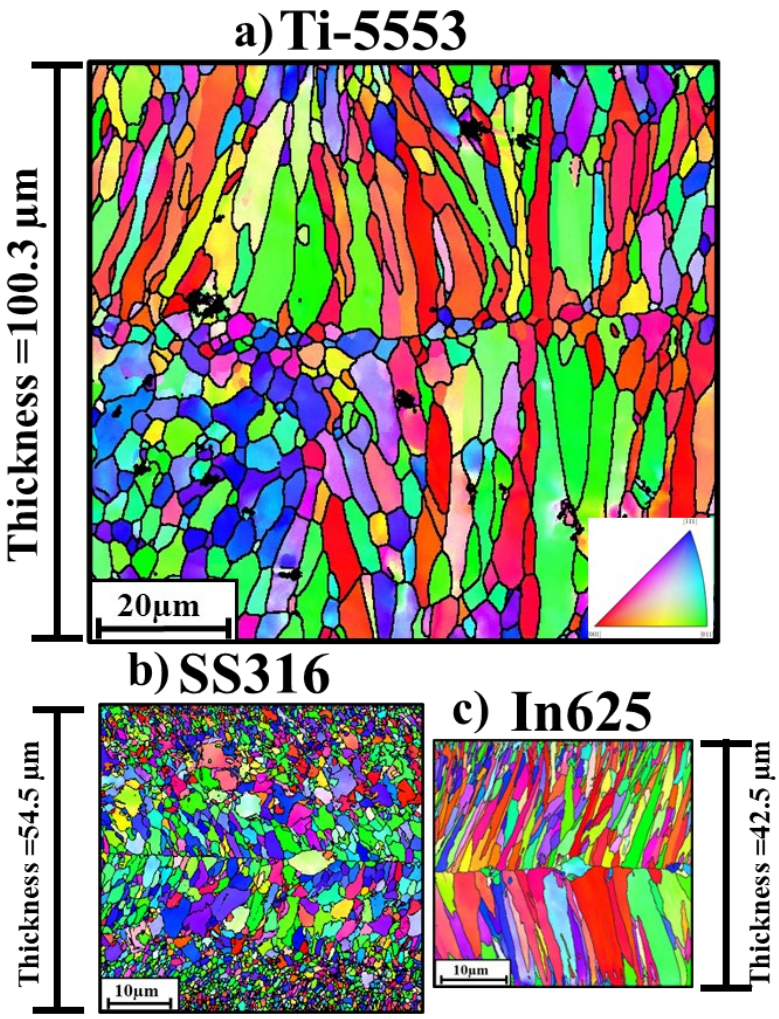

Figure 2.6 EBSD inverse pole figure maps of Ti5553, SS316, and IN625 samples created by splat quenching with copper platens at the same conditions. The orientation of grains shown in

the maps is along the solidification direction. The Ti5553 sample demonstrates a near doubling of thickness as compared to the other two materials and has a mixed microstructure of equiaxed and columnar grains at the center. The IN625 is largely dominated by columnar grains while the SS316 has a phase transition that hides the original solidification structure.

2.4.2 Effect of Surface Quality on Heat Transfer

Comparing three surface finishes, the grain sizes demonstrates that there is a cooling rate benefit to a polished platen, but the effect is limited due to flow features that lower the heat transfer coefficient by lowering the surface of material in contact with the platen. Surface profilometry was used to calculate the roughness for the three platen conditions giving values ranging from 1 μm to 50 nm, Table 2. The roughness was taken as the peak to valley height of the largest asperities present (R_z) as that depth is the controlling factor in melt interaction. As can been seen in Table 2, there is a drop in the average grain size between the 25 μm polish and the finer surface finishes. However, the other two conditions did not display a clear separation. Additionally, the standard deviation of grain sizes results in overlap between all three conditions. In order to understand the change in platens, the surface of two of specimens are compared in Figure 2.7 with SEM imaging of the central and edge region of the splat are compared. The 2.3 μm roughness platen samples clearly display a surface topography that mimics the grooves formed on the platens during grinding. The diamond polished platen with asperities the size of 0.13 μm resulted in areas of the splat that are smooth but there are also clear areas of entrapped gases generated by the material flow over the platen during splatting. There is little topographical difference between the center and edge regions of the ground platen as the melt largely conforms to the surface of the platen. The polished platens displayed more dramatic

differences based on the flow behavior of the splat region with the center having concentric rings of porosity and flow features in the region of initial melt splatting and radial valleys forming from the ejection of melt when the platens collide. These features result in a liquid to gas heat transfer as there is not contact between the melt and the platen resultingly lowering the heat transfer locally. The heat transfer coefficient model assumptions do not anticipate the flow lines found in the splat quenched samples so there would accordingly be a decrease in the heat transfer due to this lower thermal contact that would explain why there is a smaller than expected difference in the three conditions. Up to 17% of the surface area in the edge region of the polished platens in one of the flow features so roughly a fifth of the surface area for transferring heat to the substrate was effectively eliminated by a reliance on a liquid to gas heat transfer.

Table 2.2 Surface roughness values measured for three platen conditions and measured grain size of splat.

Polishing Abrasive Size	25 µm	15 µm	1 µm
Maximum Asperity Size (R_a)	0.97±0.24 µm	0.35±0.07 µm	0.05±0.01
Grain Size (µm)	3.4±1.6	2.4±0.9	2.5±0.9

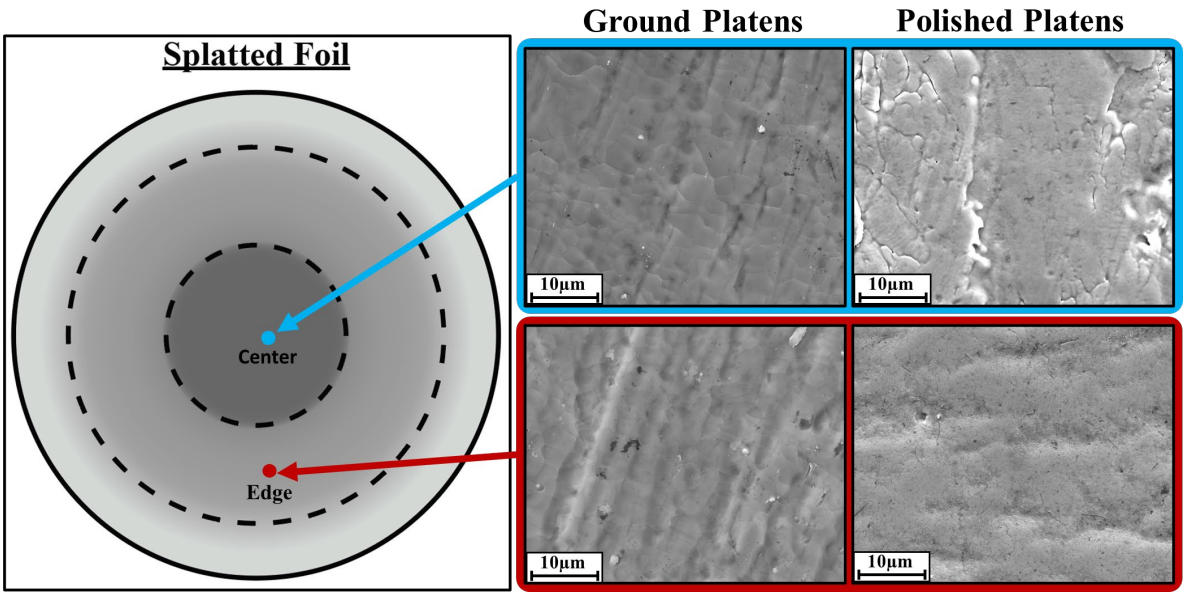

Fig 2.7 (a) Graphical representation of splat quenched foil with SEM images of the (b,c) central and (d,e) and edge regions of the splat demonstrating that there are minimal differences across the splat with the size of the asperity changing between platen surface finishes though all regions of poor thermal contact with the platens through flow features of the molten material.

2.4.3 Effect of Substrate Material on Solidification

While complicated, the interactions between the melt and platen offers a method to control the solidification conditions by the choice in substrate material. The substrate inherently controls heat transfer during splat quenching as the heat removal is largely based on conduction, and as such, there is an avenue to modify the heat transfer by changing the thermal properties of the projectile platens. Seen in Figure 2.5c, changing from copper to stainless steel and then to a low thermal conductivity ceramic should inherently lower the cooling rate. Figure 2.8. displays EBSD micrographs of the Ti-5553 splats made with four different substrates tested in this study. The difference between the titanium and copper substrates were largely minimal as expected from Eqn. 3. The difference in heat transfer coefficient between a lower thermal conductivity

substrate such as stainless steel or titanium and a copper substrate is seen to be less than the variation throughout the splat itself seen in Figure 2.5c. The stainless steel substrate similarly resulted in relatively little change in the splat behavior, but with the caveat that the stainless steel displayed significant melting and resulted in *joining of the splat to the platen* though this was not seen to significantly alter the solidification structure. This effect is likely due to the combination of the stainless steel having a low thermal diffusivity and a melting temperature lower than the molten titanium resulting in the substrate melting and subsequently welding to the splatted material. For all other substrates, the splat quenched samples are easily removed, so platen melting was found to only be a concern for the stainless steel platens. The zirconia substrate did have a pronounced impact compared to the other two substrates due to its order of magnitude lower thermal conductivity. Additionally, the titanium splat was found to be on the order of 50 microns, roughly half as much in the other substrates and was the only substrate found to significantly change the splat thickness. The zirconia platen sample also demonstrated the effect of a lowering of Biot number as the low heat transfer coefficient has resulted in grains that while still oriented along the cooling direction do not display the same columnar growth structure that the other conditions display. Other substrate-melt interactions such as nucleation potency or intermetallic formation could have an effect but were observed to provide significant impact to the microstructure observed with EBSD.

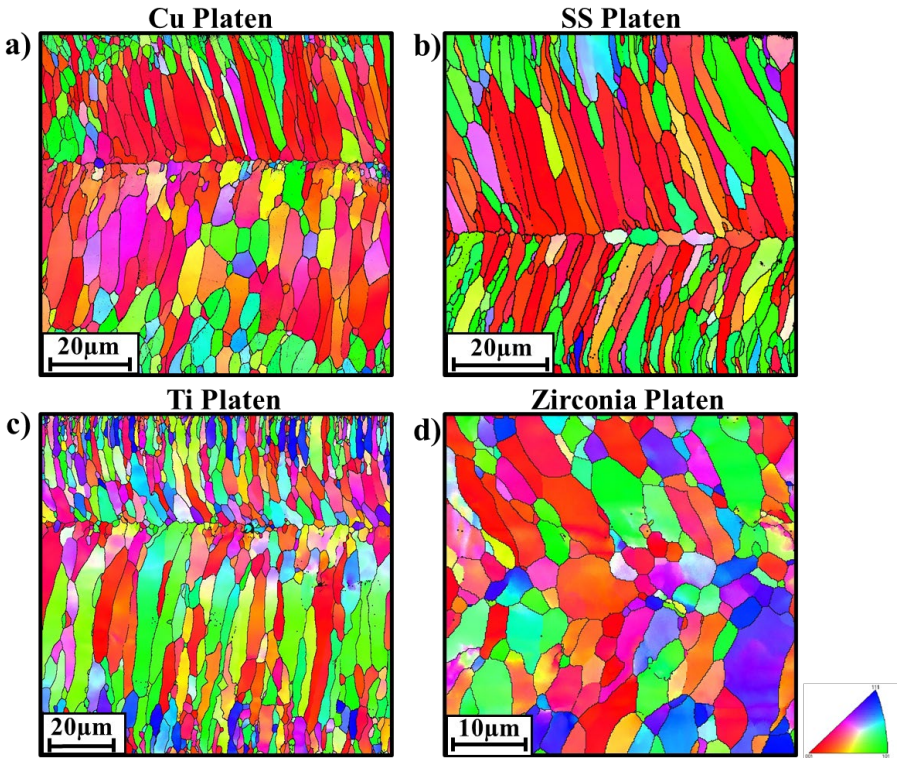

Figure 2.8 Inverse Pole Figure maps of the Ti-5553 splats made with (a) copper, (b) stainless steel 316, (c) titanium, and (d) zirconia platen. The three metallic substrates are all nominally the same thicknesses and demonstrate a strong elongation of grains along the cooling direction towards the midline. The zirconia substrate is half the thickness and does not have the same degree of columnar grains or a midline.

2.4.4 Effect of Platen Velocity on Material

The platen velocity was found to affect the thickness of the sample and to promote a higher cooling rate throughout the splat quenched sample. The velocity of the platens affects both Eqn. 2 and 3 and as a result affects both solidification regimes across the splat quenched sample. An increase in pressure during the platen collision (pressure over 1 MPa) is not expected to have a significant change in the heat transfer coefficient as can be seen in Figure 2.5. However, the increase in velocity increases the initial contact pressure of the melt impinging on the substrates . The contact pressure is related to the velocity squared and changes in the lower

pressure region are expected to offer an order of magnitude change in heat transfer coefficient. The platen velocity in this case would have a similar effect to density in changing the specimen thickness. The resulting change in thickness would have a more pronounced effect on the cooling rate than the pressure variation would have on its own. Seemingly, the platen velocity offers more control of the final cooling rate by controlling the specimen thickness rather than just by the change in contact pressure. This trend can be seen in Figure 2.9, where the average specimen thickness and calculated contact pressure (Eqn 1.) are plotted as a function of platen velocity. Two samples are then highlighted to show the variation in thickness and in solidification morphology at the center of the splat quenched foils.

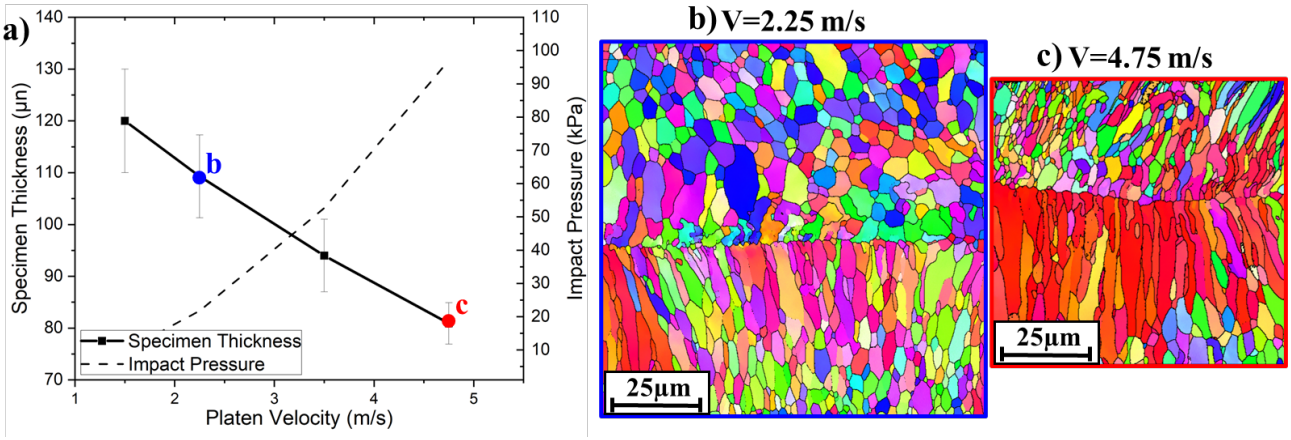

Figure 2.9 (a) Plot of data demonstrating the drop in Ti-5553 specimen thickness and increase in estimated impact pressure as a function of platen impact velocity. (b) and (c) are IPF orientation maps of the cross sections of the central region of the splats at platen velocities of 2.25 and 4.75 m/s respectively highlighted on the graph by a blue and red circle respectively.

2.4.5 Effect of Superheat on Material

The applied superheat to the melt affected the thickness of the splat, but it did not have a significant effect on the solidified microstructure when varied from 50°C to 150°C above the liquidus temperature for Ti-5553. The superheat of a molten droplet has been found across thermal spray research to have a significant effect on the cooling rate and splatting behavior. This correlation is due to higher temperature melts being able to have more deformation and flow prior to cooling enough to initiate solidification [31]. For splat quenching contact between melt and platen is enforced, and so there is a significantly smaller effect of superheat; but there is still a minimum amount needed to prevent solidification prior to the splatting event. The superheat has largely been found to reduce the viscosity of the melt and allow for marginally thinner splat quenched foils [12,17]. A trend of increased cooling rates at higher superheats has been accredited to the reduction in thickness rather than inherently the superheat [12]. Separating the individual components of heat transfer during splat quenching leads to the assumption that the thickness variation is the dominant result offered by varying the superheat. Additionally, low superheat does introduce concerns of the splat beginning to solidify either prior to splatting or before fully flattened. In addition, the cleanliness of platens are important as the low superheat is not enough to melt any embedded material in the platens resulting in preferential nucleation sites for solidification [12]. Figure 2.10 highlights these results where above 100°C superheat there is only a small change in thickness with increasing temperature with a change from 1750°C to 1850°C only resulting in a 7.6% decrease in thickness. However, below 100°C superheat there is a sharp increase in thickness that can be seen in the accompanying IPF maps to be due to premature solidification that results in drastically larger grain size and a deformation structure occurring at grain boundaries. Additionally, these low superheat samples result in significant deformation in the platens, while a higher superheat splat results in a small amount of

deformation that is easily polished flat for additional splat quenching. Solidification was seen to occur at low superheats prior to the pistons colliding. This premature soldification pushes this technique out of rapid solidification and complicates the thermal analysis and is seen more as condition to avoid by increasing the superheat rather than a parameter to control the solidification conditions.

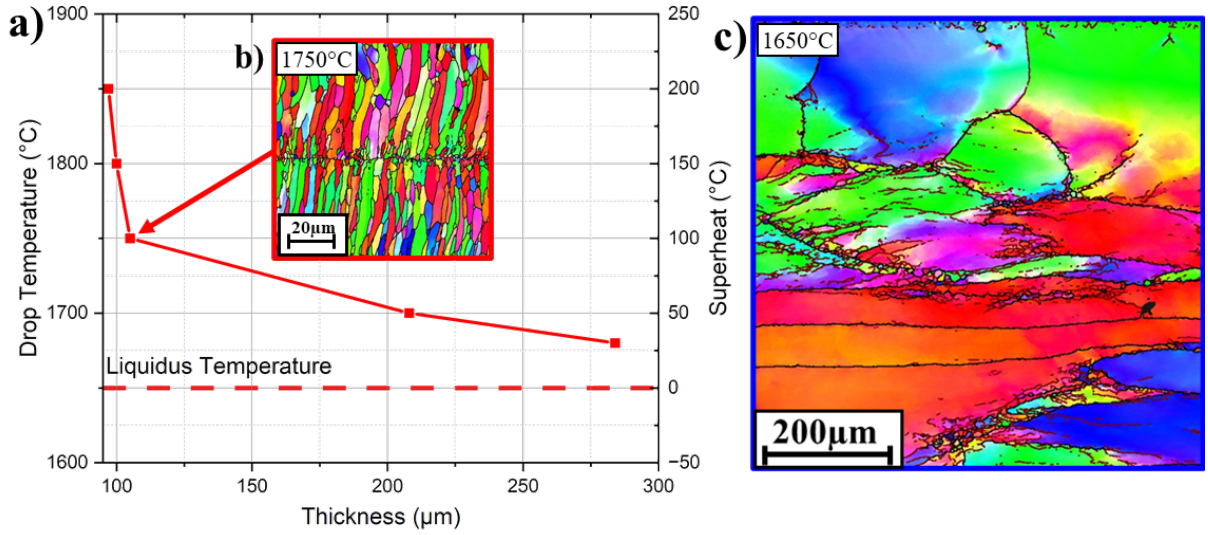

Figure 2.10 Graph of splat thickness as a function of superheat for Ti-5553 splat on copper platen. At low superheat (c), solidification occurs prior to the final collision of the platens, resulting in deformation structures forming and a significant increase in grain size of the thicker sample.

2.4.6 Comparison Between Simulation and Empirical Data

Thermal simulations demonstrated that the variation in thickness and heat transfer coefficient across a splat quenched sample can result in an order of magnitude cooling rate difference. The simulation results for the SS316 and Ti-5553 can be seen in Figure 2.11. The results exhibit, as expected, that the material nearest to the copper platen experienced the highest

cooling rate with a reduction towards the centerline of the sample. Furthermore, there is a decrease in both the temperature gradient and solidification velocity away from the substrate interface as well. The simulated material does experience an increase in the solidification velocity at the midline of the sample due to the increasingly small volume of molten material and the low thermal gradient that allows for the solidification velocity to increase. This spike in solidification velocity was not experimentally found to effect the microstructure, though the reduction in thermal gradient at the center would explain the presence of equiaxed grains at the midline in splats such as in figure 2.8. The heat transfer coefficient and thickness of sample were varied in the Ti-5553 simulation to provide a comparison to the experimental parameter changes. Decreasing splat thickness leads to expected increases in cooling rate as well as solidification velocity and thermal gradient in the material. Doubling the thickness of a Ti-5553 splat from 50 μm to 100 μm resulted in a drop in cooling rate of 39% at the interface and 66% at the center line of the sample. For a perfectly ideal, cooling condition the change in cooling rate would be proportional to the square of the thickness ratio, while with Newtonian cooling it would be a proportional to the ratio of the thicknesses [18]. Thereby the heat transfer condition predicted by the FLUENT simulation is neither *ideal* nor *Newtonian cooling* as can be seen by calculated Biot numbers of 12.5 and 25 for the 50 and 100 μm splats, respectively, that are in the intermediary cooling region outlined by Ruhl et al. [6]. When comparing the cooling rate expected from using zirconia ($h= 10^6$ W/m^{2}K) or copper ($2.5\ 10^7$ W/m^{2}K) platens there is easily an order of magnitude difference in the cooling rate at the substrate interface (96.8% reduction in cooling rate). This dramatic decrease in cooling rate is reduced throughout the thickness of the splat reducing to a 51.3% reduction at the centerline of the sample as compared to the copper. The SS316 splat quench has a lower cooling rate for the same conditions as the Ti-5553 due to the

increased thermal diffusivity of the stainless steel resulting from a 41.2% increase in density. Beyond cooling rate, the reduction in thermal gradient and solidification velocity also demonstrate at least order of magnitude drops across the thickness of the splat demonstrating the significant sampling of solidification space that is enveloped in a single splat quenched sample. This variation also explains the limited effect of several of the processing parameters as the variation in the splat itself is already so significant that small variations are often unnoticed.

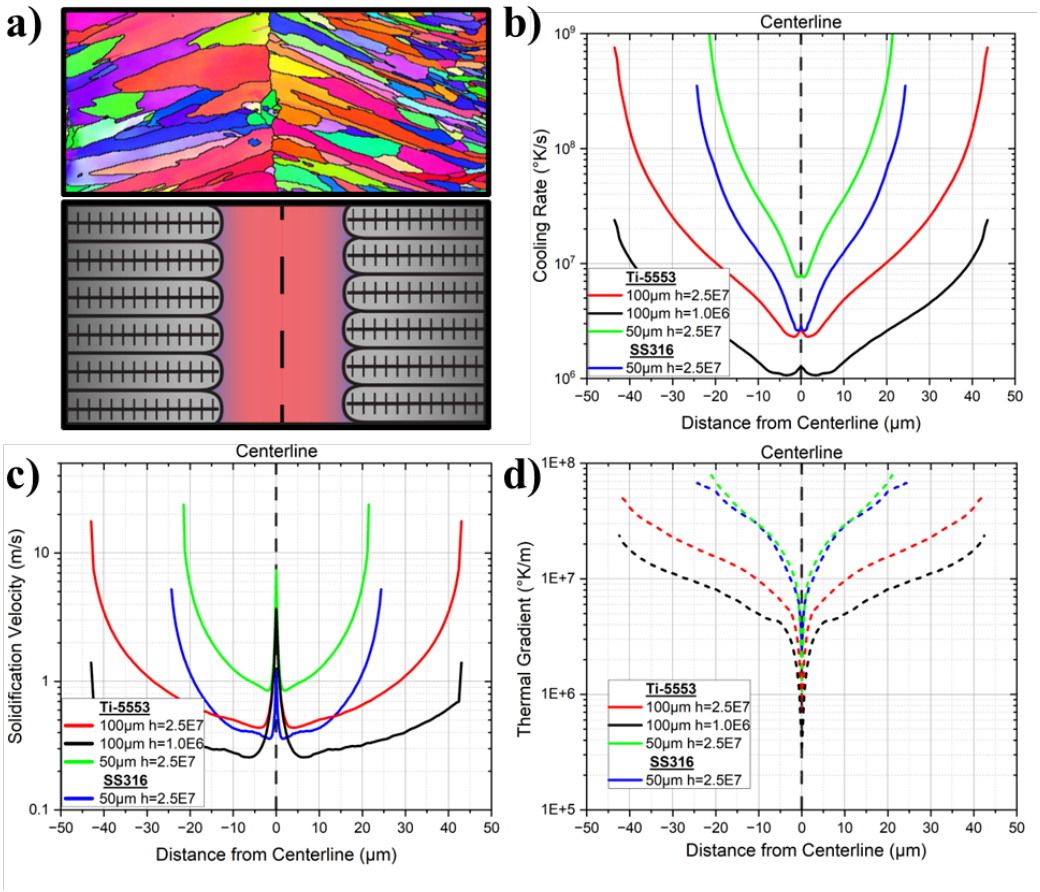

Figure 2.11 (a) IPF and illustration of the orientation of the splat quenched sample. The (b) cooling rate, (c) solidification velocity, and (d) thermal gradient predicted for the Ti-5553 splats and SS316 splat predicted from 2-D heat transfer for a variety of heat transfer coefficients ($W/m^{2}°K$) and thicknesses [32].

The cell spacing of the SS316 splat on copper platens was used to estimate the cooling rates and demonstrated that the fluent simulation was well correlated, validating the current approach. Cell spacing to cooling rate relationships are an easy method to estimate the solidification conditions and have therefore been used in areas such as AM and welding as an empirical measure to provide an understanding of the process the material is undergoing [10,33]. Using the power law fit developed from Katayama et al. [33] the expected range of cooling rate throughout the splat, Figure 2.12, is seen to have a minimum at the center of the splat quenched sample with the edges having a smaller cell size and associated higher cooling rate resulting from the two stage splatting process discussed earlier. The cooling rate predicted in the splat can then be predicted to range from 1.2 10^7 °K/s to 2.5 10^8 °K/s which matches with the FLUENT simulations that predict a maximum cooling rate on the order of 1.3 10^7 °K/s to 3.5 10^8 °K/s based on the heat transfer coefficient changing across the splat quenched sample. Therefore, the predicted heat transfer coefficients seem to align well with reality for the stainless steel material as well as the expected change in cooling condition from the center of the sample to the edge.

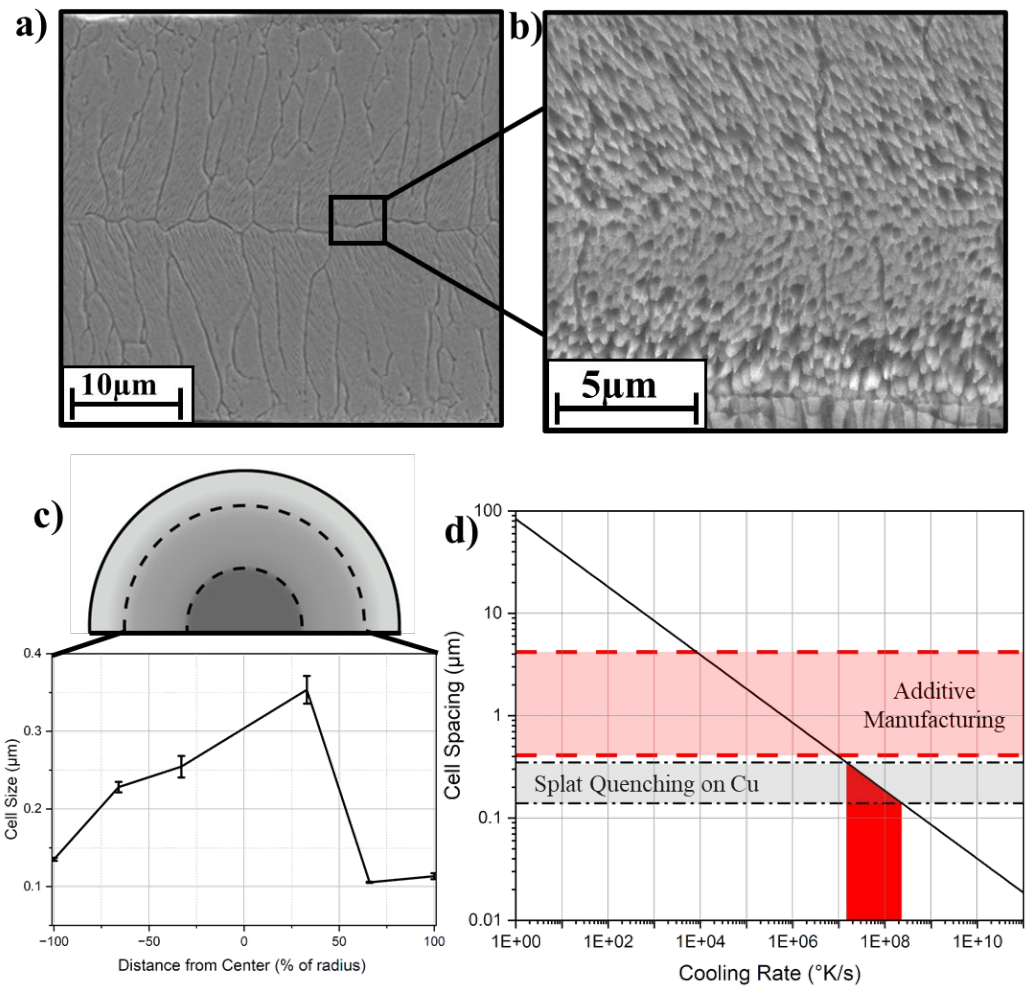

Figure 2.12 (a) SEM micrograph of an etched SS316 splat quenched foil with (b) higher magnification image of the cells measured. A graph of the cell size as a function of radius (c) demonstrating a trend of reduction in size farther from the center. (d) The cell sizes can then be compared to the cooling rate to cell spacing for stainless steel [31] to estimate the cooling rate of the splat quenched foil as compared to what is expected in additive manufacturing techniques ranging from DED to LPBF.

Splat quenching is found to have significant overlap with the conditions seen in powder bed fusion techniques offering a technique for the testing and designing of alloys without the

significant cost and time associated with AM manufacturing. The solidification conditions of splat quenching that have been estimated can be compared to literature values for additive manufacturing techniques from laser and electron beam techniques to arc processes. Figure 2.13 demonstrates that splat quenching is generally at a higher thermal gradient and solidification velocity as compared to AM techniques. There is significant overlap with beam based techniques such as laser bed powder fusion and electron beam additive manufacturing at the lowest cooling rates for SQ. The lowest cooling rate predicted occurs near the midline at the center of the splat quenched sample. The ability to decrease the cooling rate in terms of decreasing platen velocity and changing platen material offers further ability to control the cooling rate and positioning the splat quenched foils closer to the conditions present in AM processes. The slower cooling rate techniques such as wire arc AM and directed energy deposition are not accurately represented by the splat quenching processes. So even though, the splat quenching process is not able to easily match all AM techniques it offers a high throughput method to analyze the rapid solidification response of compositions in the region of laser powder bed and electron beam additive manufacturing without the need for significant investment in terms of powder and feedstock material.

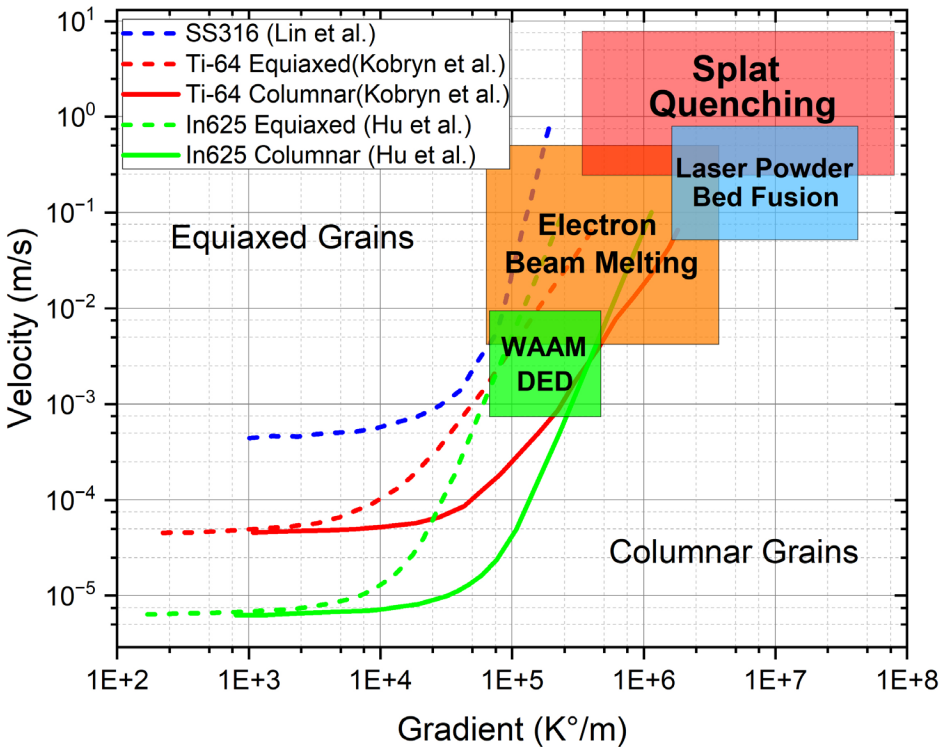

Figure 2.13 Map of the typical thermal gradients and soldification veloicties for different additive manufacturing techniques in comparision with splat quenching [34–38]. There is signficant overlap for laser and electron beam techniques and splat quenching, while lower power density techniques such as directed energy deposition and wire arc additive manufacturing posses much slower solidification velocities than those achieved in splat quenching.

2.5.0 Conclusion

In this work, the rapid solidification technique of twin hammer splat quenching (SQ) has been carefully analyzed as a method for high throughput compositional testing for use in developing alloys for additive manufacturing or laser welding applications. Various models from the thermal spray literature have been adapted and implemented to give a framework for assessing the cooling rates generated by splat quenching in terms of both testing process parameters as well as material properties of the melt and substrates. Through the use of FLUENT CFD simulation and

comparison of microstructural features, these models have been validated as a means to analytically predict the cooling rate during splat quenching so that direct comparison between the elemental segregation and microstructural phases formed in the various regions of the splat quenched sample can be compared to other rapid solidification techniques. Based on the analysis the following trends have been found:

- Splat quenching can easily process a wide range of materials from stainless steels, nickel-based alloys or titanium in a clean environment to study the phases and microstructures predicted for a rapid solidification condition.
- The cooling rate range for a typical test with copper platens at 3.5 m/s can easily reach 10^7 °K/s with changes in the platen material and velocity providing means to move from 10^6 or 10^8 °K/s.
- The cooling rate in the center of the splat is lower than at the edges due to a lower heat transfer coefficient and cooling rate during initial contact with the substrate as well as the variation in splat thickness.
- Superheat, velocity, and platen material can all affect the thickness of the splats, which in turn changes the cooling rate of the material. Of these variables, platen velocity offers the easiest way to control the splat thickness and therefore the cooling rate. Superheat can effect the microstructure by allowing the formation of more thermal gradients prior to solidification.
- The substrate material makes a significant difference in the cooling rate especially in relation to thermal conductivity of the material such as copper as compared to zirconia, while the platen surface roughness has a much lower effect than predicted likely due to

the entrapped gas and turbulent flow of the melt, which results in intermittent contact between the melt and substrate.

References

[1] D. Zhang, S. Sun, D. Qiu, M.A. Gibson, M.S. Dargusch, M. Brandt, M. Qian, M. Easton, Metal Alloys for Fusion-Based Additive Manufacturing, Adv. Eng. Mater. 20 (2018). https://doi.org/10.1002/adem.201700952.

[2] B.A. Welk, N. Taylor, Z. Kloenne, K.J. Chaput, S. Fox, H.L. Fraser, Use of Alloying to Effect an Equiaxed Microstructure in Additive Manufacturing and Subsequent Heat Treatment of High-Strength Titanium Alloys, Metall. Mater. Trans. A Phys. Metall. Mater. Sci. 52 (2021) 5367–5380. https://doi.org/10.1007/s11661-021-06475-3.

[3] T.W. Clyne, A. Garcia, The application of a new solidification heat flow model to splat cooling, J. Mater. Sci. 16 (1981) 1643–1653. https://doi.org/10.1007/BF02396883.

[4] H. Zhang, X.Y. Wang, L.L. Zheng, X.Y. Jiang, Studies of splat morphology and rapid solidification during thermal spraying, Int. J. Heat Mass Transf. 44 (2001) 4579–4592. https://doi.org/10.1016/S0017-9310(01)00109-0.

[5] T. Bennett, D. Poulikakos, Splat-quench solidification: estimating the maximum spreading of a droplet impacting a solid surface, J. Mater. Sci. 1993 284. 28 (1993) 963–970. https://doi.org/10.1007/BF00400880.

[6] R.C. Ruhl, Cooling rates in splat cooling, Mater. Sci. Eng. 1 (1967) 313–320. https://doi.org/10.1016/0025-5416(67)90013-4.

[7] F. Duflos, B. Cantor, Cooling rate measurements on pure iron rapidly solidified by piston quenching, J. Mater. Sci. 22 (1987) 3765–3770. https://doi.org/10.1007/BF01161492.

[8] S. Krishnamurthy, H. Jones, F.H. Froes, Solidification microstructures of hammer and anvil splat-quenched binary titanium alloys, J. Mater. Sci. Lett. 7 (1988) 1138–1141. https://doi.org/10.1007/BF00720858.

[9] R. Ray, B.C. Giessen, N.J. Grant, The constitution of metastable titanium-rich Ti-Fe alloys:An order-disorder transition, Metall. Trans. 3 (1972) 627–629. https://doi.org/10.1007/BF02642743.

[10] Z.A. Hasenbusch, G. Harvill, K. Ziska, A. Deal, B. Brown, L. Nastac, L.N. Brewer, Influence of Molybdenum on Rapid Solidification Microstructure and Microsegregation in

Primary Ferrite Solidified Stainless Steel, Metall. Mater. Trans. A Phys. Metall. Mater. Sci. 54 (2023) 4834–4849. https://doi.org/10.1007/s11661-023-07206-6.

[11] H.A. Davies, J.B. Hull, The formation, structure and crystallization of non-crystalline nickel produced by splat-quenching, J. Mater. Sci. 11 (1976) 215–223. https://doi.org/10.1007/BF00551430.

[12] M.G. Scott, The role of melt superheat in splat-quenching, J. Mater. Sci. 1975 102. 10 (1975) 269–273. https://doi.org/10.1007/BF00540350.

[13] R.W. Cahn, K.D. Krishnanand, M. Laridjani, M. Greenholz, R. Hill, Novel splat-quenching techniques and methods for assessing their performance, Mater. Sci. Eng. 23 (1976) 83–86. https://doi.org/10.1016/0025-5416(76)90171-3.

[14] K. Miyazawa, J. Szekely, A mathematical model of the splat cooling process using the piston and anvil technique, Metall. Trans. B. 10 (1979) 349–358. https://doi.org/10.1007/BF02652505.

[15] Y. Inokuti, B. Cantor, The formation of martensite in splat-quenched Fe-Mn and Fe-Ni-C alloys, J. Mater. Sci. 1977 125. 12 (1977) 946–958. https://doi.org/10.1007/BF00540977.

[16] D.M. Kroeger, W.A. Coghlan, D.S. Easton, C.C. Koch, J.O. Scarbrough, A study of cooling rates during metallic glass formation in a hammer and anvil apparatus, J. Appl. Phys. 53 (1982) 1445–1453. https://doi.org/10.1063/1.330639.

[17] W.E. Brower, S.C. Megli, Influence of superheat and hammer speed on the formation of metallic glasses, Mater. Sci. Eng. A. 133 (1991) 846–849. https://doi.org/10.1016/0921-5093(91)90199-W.

[18] T.Z. Kattamis, W.F. Brower, R. Mehrabian, Microstructure and segregation in splat-cooled iron-nickel alloy, J. Cryst. Growth. 19 (1973) 229–236. https://doi.org/10.1016/0022-0248(73)90044-4.

[19] T.F. Broderick, A.G. Jackson, H. Jones, F.H. Froes, The effect of cooling conditions on the microstructure of rapidly solidified Ti-6Al-4V, Metall. Trans. A. 16 (1985) 1951–1959. https://doi.org/10.1007/BF02662396.

[20] C.J. Li, J.L. Li, Transient contact pressure during flattening of thermal spray droplet and its effect on splat formation, J. Therm. Spray Technol. 13 (2004) 229–238. https://doi.org/10.1361/10599630418158.

[21] M. Karkkainen, L. Nastac, Evaluation and Implementation of a Fundamental Model for

Interfacial Heat Transfer Coefficient in High-Pressure Die-Casting, Metall. Mater. Trans. B Process Metall. Mater. Process. Sci. 51 (2020) 664–676. https://doi.org/10.1007/s11663-020-01784-1.

[22] N.Z. Mehdizadeh, S. Chandra, J. Mostaghimi, Formation of fingers around the edges of a drop hitting a metal plate with high velocity, J. Fluid Mech. 510 (2004) 353–373. https://doi.org/10.1017/S0022112004009310.

[23] C. Hayzelden, J.J. Rayment, B. Cantor, Rapid solidification microstructures in austenitic Fe-Ni alloys, Acta Metall. 31 (1983) 379–386. https://doi.org/10.1016/0001-6160(83)90215-8.

[24] Q. Sun, P. Jin, Y.B. Liu, J. Li, J. Wang, T. Ma, J. Feng, Wetting of liquid copper on TC4 titanium alloy and 304 stainless steel at 1273–1433 K, Mater. Des. 169 (2019) 107667. https://doi.org/10.1016/j.matdes.2019.107667.

[25] M. Xue, Y. Heichal, S. Chandra, J. Mostaghimi, Modeling the impact of a molten metal droplet on a solid surface using variable interfacial thermal contact resistance, J. Mater. Sci. 42 (2007) 9–18. https://doi.org/10.1007/s10853-006-1129-x.

[26] R.S. Prasher, Surface chemistry and characteristics based model for the thermal contact resistance of fluidic interstitial thermal interface materials, J. Heat Transfer. 123 (2001) 969–975. https://doi.org/10.1115/1.1388301.

[27] T. Bennett, D. Poulikakos, Splat-quench solidification: estimating the maximum spreading of a droplet impacting a solid surface, J. Mater. Sci. 1993 284. 28 (1993) 963–970. https://doi.org/10.1007/BF00400880.

[28] J. Madejski, Solidification of droplets on a cold surface, Int. J. Heat Mass Transf. 19 (1976) 1009–1013. https://doi.org/10.1016/0017-9310(76)90183-6.

[29] H. Jones, Cooling rates during rapid solidification from a chill surface, Mater. Lett. 26 (1996) 133–136. https://doi.org/10.1016/0167-577X(95)00213-8.

[30] F.J. Heymann, High-speed impact between a liquid drop and a solid surface, J. Appl. Phys. 40 (1969) 5113–5122. https://doi.org/10.1063/1.1657361.

[31] G.X. Wang, E.F. Matthys, Experimental determination of the interfacial heat transfer during cooling and solidification of molten metal droplets impacting on a metallic substrate: effect of roughness and superheat, Int. J. Heat Mass Transf. 45 (2002) 4967–4981. https://doi.org/10.1016/S0017-9310(02)00199-0.

[32] L. Nastac, Splat Quench Mapping of Titanium Additive Manufacturing: Fluent Modeling and Analysis, 2024.

[33] S. Katayama, A. Matsunawa, Solidification Microstructure of Laser Welded Stainless Steels, 44 (1984) 60–67.

[34] J.A. Kittl, M.J. Aziz, D.P. Brunco, M.O. Thompson, Nonequilibrium partitioning during rapid solidification of SiAs alloys, J. Cryst. Growth. 148 (1995) 172–182. https://doi.org/10.1016/0022-0248(94)00836-1.

[35] J. Yoshioka, M. Eshraghi, Temporal evolution of temperature gradient and solidification rate in laser powder bed fusion additive manufacturing, Heat Mass Transf. Und Stoffuebertragung. 59 (2023) 1155–1166. https://doi.org/10.1007/s00231-022-03318-8.

[36] Z. Yan, W. Liu, Z. Tang, X. Liu, N. Zhang, M. Li, H. Zhang, Review on thermal analysis in laser-based additive manufacturing, Opt. Laser Technol. 106 (2018) 427–441. https://doi.org/10.1016/j.optlastec.2018.04.034.

[37] Z.J. Li, P. Xiao, H.L. Dai, W.F. Luo, C. Du, Z.F. Tong, Thermo-mechanical analysis of functionally graded nickel/titanium alloys under different process parameters of directed energy deposition, Thin-Walled Struct. 193 (2023) 111235. https://doi.org/10.1016/j.tws.2023.111235.

[38] N. Raghavan, R. Dehoff, S. Pannala, S. Simunovic, M. Kirka, J. Turner, N. Carlson, S.S. Babu, Numerical modeling of heat-transfer and the influence of process parameters on tailoring the grain morphology of IN718 in electron beam additive manufacturing, Acta Mater. 112 (2016) 303–314. https://doi.org/10.1016/j.actamat.2016.03.063.

CHAPTER 3 : CRYSTALLOGRAPHIC STABILITY OF THE BCC PHASE DURING QUENCHING OF METASTABLE BETA TITANIUM ALLOY TI5553 AND COMPARISON OF STRUCTURAL CRITERIA FOR THE PREDICTIVE CAPABILITY OF α" MARTENSITE

C.J. Williamson[a], A. Deal[b], B. Brown[b], L. Nastac[a], L.N. Brewer[a]

[a] Department of Metallurgical and Materials Engineering, The University of Alabama, Tuscaloosa, AL 35487, USA

[b] Department of Energy's National Security Campus, Honeywell Federal Manufacturing & Technologies, Botts 214281 281 Road, Kansas City, MO 14520, USA

This work evaluates the compositional standard currently developed for Ti-5553 powder and explores the metastable β region for sensitivity to martensitic formation during rapid quenching from the melt. Ti-5553 is a beta-stabilized titanium alloy that is increasingly being used in additive manufacturing applications. The use of both empirical models such as molybdenum equivalency and martensitic start temperature as well as physics based martensitic energy models are compared to the composition to understand the accuracy and limitations of the applied models. A series of alloys within the Ti-5553 compositional space was produced and then processed using two-piston spat quenching to perform rapid solidification and quenching for each of these alloy compositions. X-ray diffraction and electron microscopy provided information about the composition, crystallography, and microstructure for this set of rapidly quenched titanium alloys. Typical empirical models such as molybdenum equivalency are not able to fully separate the retained BCC and martensitic compositions as the basic empirical natures of the models is meant for as a general phase stability approximation and not as an alloy design tool. The use of estimating the energy needed to transform the martensite that relies on thermodynamic data to estimate the T_0 temperature is able to differentiate the alloys and provide a metric to further develop compositional limits for metastable beta titanium alloy development.

3.1.0 Introduction

Beta titanium alloys have garnered increasing popularity due to the growth of techniques that employ rapid solidification, as the high solidification velocity eliminates many of the negative effects that have stymied previous attempts to explore the alloy space in the later part of the 20th century. Techniques such as atomization and fusion based AM processing operate at solidification velocities that largely mitigate the segregation-based beta fleck formation, which limits the ability to cast these alloys due to its detrimental effect on mechanical properties such as fatigue. In light of this advance, the use and development of beta stabilized alloys have grown to offer alloys that have unique deformation mechanisms, increased heat treatability, and a low modulus of elasticity. In this space, the titanium alloy Ti-5Al-5V-5V-3Cr (0.4 Fe), known simply as Ti-5553, has been used as a heat treatable, metastable beta alloy offering increased strength as compared to the alpha-beta Ti-6Al-4V alloy that has largely dominated structural titanium alloys, particularly for AM.

Ti-5553 is categorized as a metastable beta alloy meaning that, when quenched, there is only BCC retained; but upon heat treatment, the HCP (α) phase is precipitated out. Unlike in fully beta-stabilized alloys where the BCC structure is maintained even after heat treatment, metastable beta alloys can nucleate and grow α structures upon aging. The metastable beta titanium alloys often exist in a region of titanium alloy space that resides at the borderline between transformation induced plasticity (TRIP) effects and martensitic development upon quenching. The instability of the BCC matrix is largely considered the controlling factor, with β stabilizers such as Fe, Cr, Mo, and V being added to stabilize the BCC structure and α stabilizers, Al, reducing the stability. The stability of the alloy has been described by numerous criterion such as a molybdenum equivalency that act to provide a numerical value to ascertain the amount of BCC retained. This equivalency has been used for many decades as a means of estimating the overall stability of the BCC phase, but it can have difficulty delineating the transitory region such as alloys displaying TRIP or TWIP properties. The mostly widely used tool across the literature when exploring this metastable beta alloy space is the molecular orbital method [1,2] that uses two compositionally controlled bonding parameters, d-orbital energy level (Md) and bond order (Bo), to map out the titanium alloy space and to plot regions of stability as well as to predict deformation mechanisms and Young's modulus [3–7]. These Bo-Md maps have significant usefulness in predicting superelastic properties and Young's moduli, but again this approach has difficulty in clearly delineating compositional regions that form martensite upon quenching [8].

The martensite developed in these beta stabilized titanium alloys can be either HCP α' (P63/mmc) or orthorhombic α" (Cmcm), depending entirely on composition. The breakdown from the high temperature BCC phase into the HCP phase results in the angle between the <111> directions changing from 70.5° in the {110} BCC plane to 60° in the HCP structure (α'), displayed graphically in Figure 3.1. The inability to complete this shear/shuffle of the atomic structure results in an intermediary orthorhombic structure (α") [9]. The shuffle of the atomic structure is fixed for BCC and HCP with the orthorhombic structure existing as a transitory state connecting the BCC lattice to the HCP lattice as the composition varies [10–12]. The result being that in quenching, during which the time too short to allow for the formation of HCP, there is instead the formation of the martensitic orthorhombic phase. The α" phase has been observed in numerous binary alloys such as Ti-V [10], Ti-Mo [13,14], and Ti-Nb [12] but not in alloys with elements such as Ti-Fe[15] and Ti-Cr [16] that instead form α' and β. Furthermore, there are no studies on ternary, quaternary , or more complex alloys and the change in α' or α" stability. So, at present, there is limited established data on the effect of complex alloying such as in structural alloys on the development and structure of the orthorhombic martensite phase. Alloys that include solutes that include both α" and α' formers therefore have not been studied to understand the effect that the mixed solutes have on phase formation.

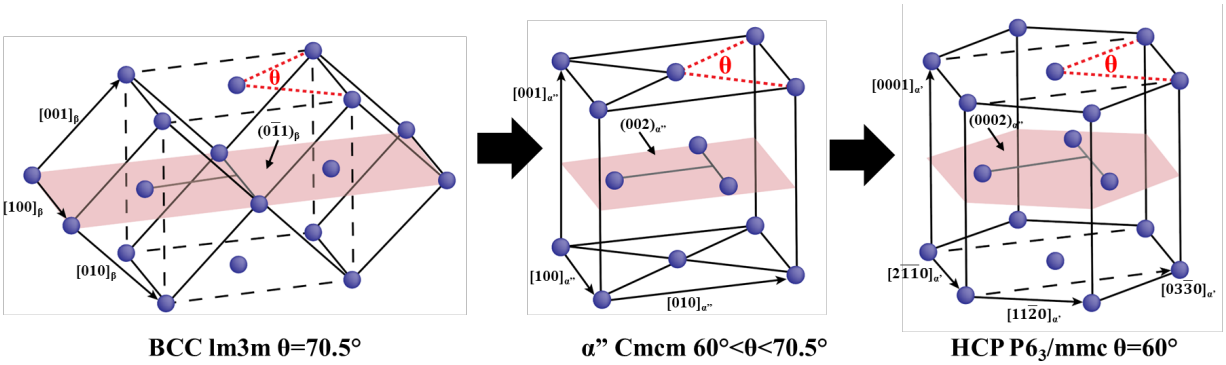

BCC Im3m θ=70.5° **α" Cmcm 60°<θ<70.5°** **HCP $P6_3/mmc$ θ=60°**

Figure 3.1 Crystal structure of the BCC (a), orthorhombic (b), and HCP (c) phases in titanium space redrawn and modified from work by Bönisch et al. [12]. The same equivalent crystallographic plane is outlined in each structure to note the shift in atoms that results in the change. In the BCC and HCP structures, the equivalent orthorhombic structure is outlined (dashed lines) to reinforce the correlation between the three phases.

Due to the desire for material to have predictable microstructures and mechanical properties throughout manufacturing and service life, compositional standards for the alloy have been created, such as AMS 7026 [17]. AMS 7026, seen in Table 1, is a standard created to control the alloy composition in powder for additive manufacturing. The use of the composition allows for control and predictability in the heat treatment response as the phase content of α after heat treatment has a significant effect on the mechanical properties. There is, however, another area of concern that upon quenching there is formation of a martensitic phase. The formation of the martensitic phase is a concern for certain heat treatments applied to Ti-5553 that require quenching, as well as, in additive manufacturing or laser welding where the rapid solidification and cooling innate to these processes offer another route for martensitic development. Due to the nature of the difficulty and cost in experimentally testing a significant number of alloys in a rapidly quenched condition, there is generally not a robust exploration of the composition space to fully understand the BCC matrix stability.

Table 3.1 Compositional range allowable in AMS 7026 for major solute in Ti-5553

Element	**Ti**	**Al**	**V**	**Mo**	**Cr**	**Fe**	**O**
wt%	Bal.	4.4-5.7	4.0-5.5	4.0-5.5	2.5-3.5	0.3-0.5	0.18 max

As such, splat quenching (SQ) as a technique is uniquely placed as a method to test a large number of alloy compositions in rapidly solidified conditions to provide fundamental information without the need for the significant material cost and time investment of attempting to additively manufacture a selected group of compositions. SQ has been used for the purpose of exploring rapid solidification behavior in titanium alloys to study extended solubility as well as dispersoid formation previously [18–20] as well as in recent work on the effect of compositional variance in alloys such as SS316L [21]. The technique uses inductive heating and levitation to heat material to a desired superheat above its melting point in a containerless condition that allows for the study of reactive metals in an argon atmosphere without concern for material interaction with a crucible. The temperature of the small specimen, ~100 mg, is monitored through the use of a two-color pyrometer and once the desired superheat of the material is reached, the power to the induction coil is removed resulting in the molten material falling. The molten material falls through a laser line and activates electromagnetically fired platens, velocity of 2-5 m/s, which strike and compress

the molten ball resulting in a thin, coin-shaped foil on the order of 50-100 µm in thickness. The high surface area to volume ratio of the splat and high thermal conductivity of the copper platens results in cooling rates on the order of 10^6-10^7K/s in the center of the splats [22]. The benefits of the technique are that only small amounts (~100 mg) of material need to be created and can then be easily processed at high solidification rates without the need for significant material volumes or the use of processing techniques such as atomization.

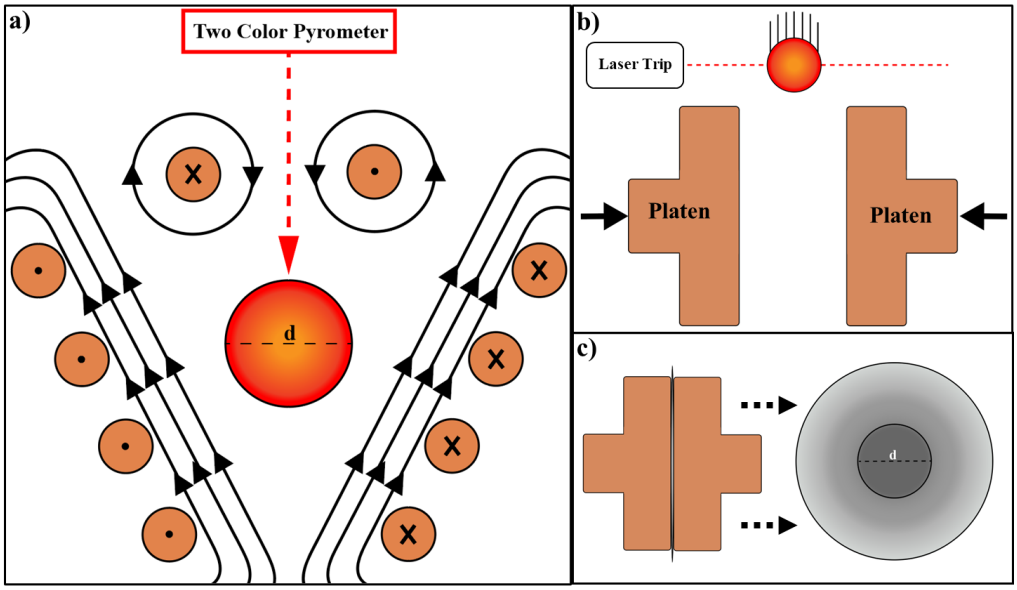

Figure 3.2 Graphic of (a) molten material levitating/heating in inductive coil with magnetic field lines shown, (b) falling towards projectile platens, and (c) the resultant foil produced.

In the present work, the Ti-5553 compositional space, according to AMS 7026, has been investigated using splat quenching to provide analysis on the stability of the BCC phase formed upon rapid solidification and quenching. Nineteen individual alloys were produced to examine this compositional space inside and around the AMS 7026 standard. The use of x-ray diffraction (XRD) and electron microscopy techniques allow for characterization of phases both morphologically and structurally. An understanding of the structural changes and phases present as a function of solute addition is then mapped onto various criterion to explore the potential for predicting what regions of the compositional space could potentially offer significant crystallographic instability in the BCC parent phase.

3.2.0 Experimental Procedures

The alloys were chosen based off a simple aluminum and molybdenum equivalency, spanning AMS 7026, that allowed for generalizations of the numerous beta stabilizers according to previous ratios from the literature [23]. The Mo_{eq} equation used can be seen in Eqn. 1, while the traditional HCP stabilizers are normalized in an Al_{eq}, Eqn. 2. For the use of the current work, aluminum and oxygen act as the only HCP stabilizers in the alloy. Generally, the phase stability value is typically the difference between the Mo_{eq} (Eqn. 1) and Al_{eq} (Eqn. 2) as this is expected to give a total value for expected BCC phase stabilization. This approach is generally just referred to as Mo_{eq} number and is been seen historically to act as a predictive tool for understanding the amount of BCC expected in a titanium alloy.

$$Mo_{eq} = Mo_{wt\%} + 0.67\, V_{wt\%} + 1.25\, Cr_{wt\%} + 2.5\, Fe_{wt\%} \quad (1)$$

$$Al_{eq} = Al_{wt\%} + 10\, O_{wt\%} \quad (2)$$

The alloy space, as defined by the compositional standard for pre-alloyed powder for additive manufacturing, ASM 7026 [17], can then be outlined according to aluminum equilibrium and molybdenum equivalency as seen in Figure 3.4b. In total, nineteen alloys were created to explore the region of alloy space around Ti-5553 with a focus around the lower beta stabilized region. Instrumental gas analysis, IGA, demonstrated an oxygen content across representative samples chosen from the nominal, max α, and max β alloys of **0.068±0.004 wt%** and a nitrogen content of **0.0081±0.0015 wt%** that was assumed constant for all alloys since the methods of preparations was held identical for all compositions. The oxygen was intentionally minimized and was not intended as a variable. Additionally, the nitrogen content was low enough that it was assumed to have minimal impact on the resulting crystallographic structure and ignored during further analysis of these alloys. Due to the standard deviation across the three tested samples being an order of magnitude lower than the average, the samples were assumed to have oxygen variation of a similar order to the standard deviation and was therefore neglected from analysis assuming instead a constant value of 0.068 wt%.

The alloy compositions can be seen in Table 2. The table lays out the compositions as well as the total Mo_{eq} for each of the alloys. The alloy compositions were measured using quantitative x-ray energy dispersive spectroscopy (QEDS) conducted on a JEOL FEG SEM equipped with an Oxford X-Max EDS detector and processed with Aztec Software. The scans were run in triplicate

for 120s live time at a beam current of 0.5 nA at a process time of 4. The collected EDS spectra were then analyzed using DTSA II with pure elemental standards to calculate the composition. The vanadium, chromium, and iron had associated errors on the order of 0.05 wt% though the aluminum and molybdenum had higher errors in the range of 0.2-0.4 wt% across the scans.

Table 3.2 Composition of alloys in wt% measured by QEDS.

	Alloy Composition (wt%)									
	Phases	**Aluminum**	**Vanadium**	**Molybdenum**	**Chromium**	**Iron**	**Al_{eq}**	**Mo_{eq}**	**(Moeq-Al_{eq})**	**e/a**
1-Max α	α"+β	5.8	3.6	3.8	2.5	0.4	5.8	9.5	3.7	4.018
2	α"+β	5.6	4.0	3.6	2.4	0.3	5.6	9.4	3.8	4.021
3	α"+β	5.6	4.8	2.4	2.8	0.4	5.6	9.5	3.9	4.027
4	α"+β	5.2	4.7	2.5	2.7	0.5	5.2	9.6	4.4	4.035
5	α"+β	5.1	4.1	4.0	2.3	0.3	5.1	9.7	4.6	4.034
6	α"+β	4.3	4.8	2.4	2.7	0.4	4.3	9.4	5.1	4.049
7	β	5.7	4.3	4.6	2.7	0.4	5.7	11.3	5.6	4.041
8	α"+β	4.5	5.0	4.0	2.4	0.3	4.5	10.5	6.0	4.054
9	β	4.9	4.4	4.9	2.5	0.3	4.9	11.2	6.2	4.052
10	β	5.7	4.8	4.5	3.0	0.4	5.7	11.9	6.3	4.051
11	β	4.7	4.5	4.5	2.8	0.4	4.7	11.3	6.6	4.060
12	β	4.4	5.0	4.2	3.0	0.4	4.4	11.7	7.3	4.073
13	β	5.1	5.7	4.0	3.3	0.5	5.1	12.7	7.5	4.073
14-near nominal	β	5.2	5.2	5.3	3.1	0.4	5.2	13.1	7.9	4.073
15	β	5.7	5.0	5.5	3.3	0.5	5.7	13.6	7.9	4.071
16	β	4.6	5.2	4.0	3.5	0.5	4.6	12.5	7.9	4.081
17	β	5.7	5.5	5.5	3.5	0.6	5.7	14.5	8.8	4.082
18	β	4.4	5.5	4.8	3.4	0.5	4.4	13.4	9.0	4.094
19-Max ß	β	4.8	5.2	5.5	3.5	0.6	4.8	14.2	9.4	4.095

The alloys were created from 99.995% pure elemental feedstock material (Kurt J Lesker) that were arc melted into buttons under argon and flipped four times. The buttons were cut into cubes using a wire EDM . The prepared cubes (2-3 mm length per side) were then sanded to remove the recast layer. This process produced samples around 70 milligrams in mass that could be used in the splat quenching process. The cubes were super-heated to 1750°C as measured by a two color pyrometer (Fluke Model:E1RH-F0-L0-0) prior to being dropped. X-ray diffraction was then conducted on these rapidly solidified foils to investigate the phases formed as well as any structural variation in those phases as a function of the composition. No processing step was conducted between splat quenching and x-ray diffraction (XRD)` diffraction as the samples were flat enough for analysis, thereby ensuring that the phases indexed were from the SQ process and

not induced by specimen preparation afterwards. A Phillips X'Pert x-ray diffractometer was used with a Cu-Kα x-ray source and an angular step size of 0.05° at a collection time of 50 s/°. The XRD was calibrated using a silicon standard to 0.01° at the <111> peak (28.44°) and 0.006° at <531> (114.09°). The lattice parameters were fitted by Rietveld refinement using the HighScore Plus software. After XRD, representative splats were subsequently sectioned, graphically represented in Figure 3.3, and mounted to investigate the cross sectional solidification morphology. The samples were then polished to a 0.05 µm colloidal silica finish. They were then imaged using a JEOL 7000 FEG-SEM at 20 keV. Electron back scatter diffraction (EBSD) was performed to allow for analysis of the grain and phase morphology. The EBSD patterns were collected by Oxford HKLNordlys EBSD with a step size of 125 nm across the thickness of the splat quenched sample on the order of 100 µm. The phases indexed were BCC and an orthorhombic phase created from the indexed XRD patterns of a α" containing splat with a space group of Cmcm, Wyckoff position 4c. Additionally, thermodynamic properties such Gibbs free energy, T0, and equilibrium phases were calculated using the Thermo-Calc TCTI5 database.

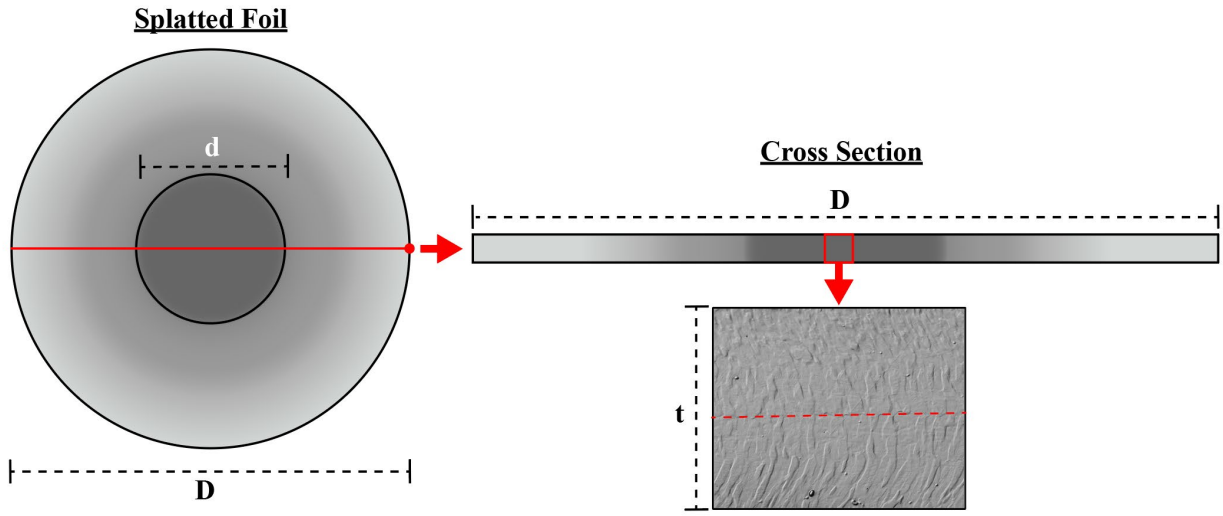

Figure 3.3 Graphical representation of the orientation and location of the area for the EBSD scan in the splat quenched foil cross section.

3.3.0 Results

The XRD patterns clearly demonstrate differences in the crystal structure due to compositional variation in the splat quenched alloys. Three representative diffraction patterns from

the near-nominal Ti-5553, Alloy 14 in Table 2, as well as the two corners of the compositional range in terms of maximum BCC and HCP stabilization are displayed in Figure 3.4. The increased stabilization of the BCC phase does not have any apparent effect on the diffraction pattern as the max β and near-nominal compositions are identical with the only difference being a slight peak shift due to a change in lattice parameter. However, a reduction in BCC stability resulted in the presence of both *BCC and orthorhombic phases in the material*. The orthorhombic phase, space group 63 (Cmcm, Wyckoff position 4c), is the α" martensite that is forming due to an incomplete transition to the HCP structure[12]. Additionally, the XRD pattern demonstrate a significant texture in the splat quenched material due to the preferred solidification directions, i.e. <110> in BCC material. This is highlighted by comparing the XRD of the BCC alloys with XRD of powder Ti-5553 highlighting an increase in counts from the <121> peak compared to the other peaks. The transition between the BCC phase to martensite is not a subtle transition with the samples either fully BCC or having broken into the orthorhombic phase. The aluminum equivalency was not seen to significantly impact the phases formed with changes to the molybdenum equivalency being seen to be the controlling factor for phase selection, Figure 3.4b.

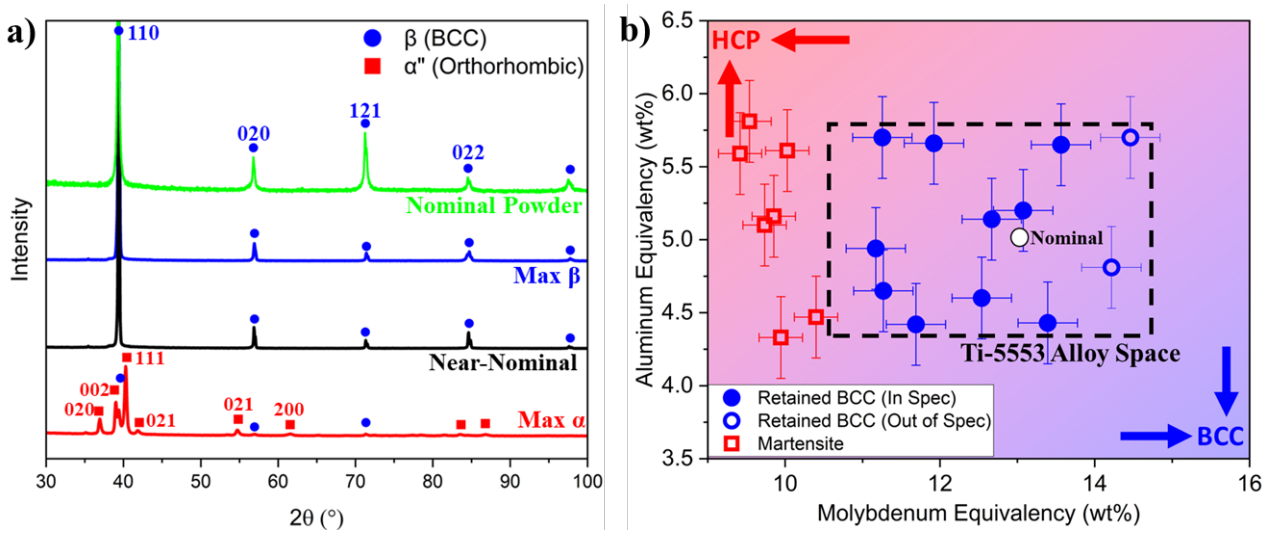

Figure 3.4 (a) Representative XRD patterns from three of the splat quenched alloys demonstrating the change in crystal structure resulting from reduction in beta stabilizers in the alloy. (b) plot of the identified phases (red-α", blue-β) across a composition space of molybdenum and aluminum equivalency with the nominal composition highlighted in white

Rietveld refinement of XRD patterns showed a shift in the lattice parameters for the BCC and orthorhombic phases. Correlating the changes in lattice parameters to the Moeq had limited success due to the intricacies of modifying several solutes at a time. The BCC lattice parameter was nominally the same for all the alloys with the largest shift measured on the order of 0.01 Å. The error associated with the XRD goniometer error were plotted in both lattice parameters and result in overlap in the lattice parameter. When plotted according to Mo_{eq}, Figure 3.5a, the fully BCC alloys displayed a minor shift in lattice parameter corresponding to Mo_{eq}. The orthorhombic structure demonstrated larger lattice parameter changes across the alloy range as compared to the BCC structure both in lattice parameters as well as changes in the unit cell shape. When correlated to the molybdenum equivalency, the $b_{\alpha"}$ and $c_{\alpha"}$ both increased and the $a_{\alpha"}$ was largely constant with some fluctuation between the alloys.

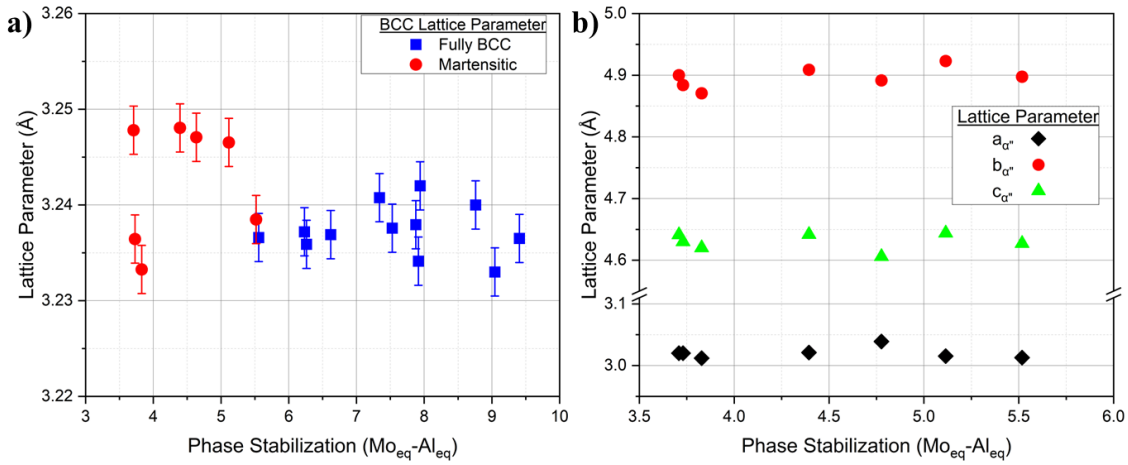

Figure 3.5 Comparison of lattice parameter for the (a) BCC phase that occurs in the fully stabilized compositions and is partially retained in the martensitic samples. (b) α" martensite lattice parameters as a function of molybdenum equivalency.

Further exploration into the microstructure of the splat quenched samples was done with EBSD that validates the differences between the compositions seen in the XRD spectra. Figures

3.6a and b are the inverse pole figure (IPF) map and band contrast map for the near-nominal Ti5553 alloy with Figures 3.6 c-f containing these maps for the maximum α and maximum β alloys respectively. What can be seen in the IPF maps is that there is some minor difference in the solidification morphology of the near-nominal and max-β alloys potentially due to differences in constitutional undercooling effects as there is an increased amount of BCC stabilizers in the alloy. However, in the low beta stabilized region, there is the presence of martensite laths throughout the entire sample. Similarly in the band contrast maps, the prior-beta grains seen in the max α can be seen revealing a very similar structure to the other two alloys. When examining the martensitic laths, the smaller prior-beta grains tend to have smaller lates resulting in the small grains at the center and edges to display much finer microstructure. The IPF maps also demonstrate the preferred <110> and <100> solidification direction in the splats that are the known preferred growth direction in BCC material.

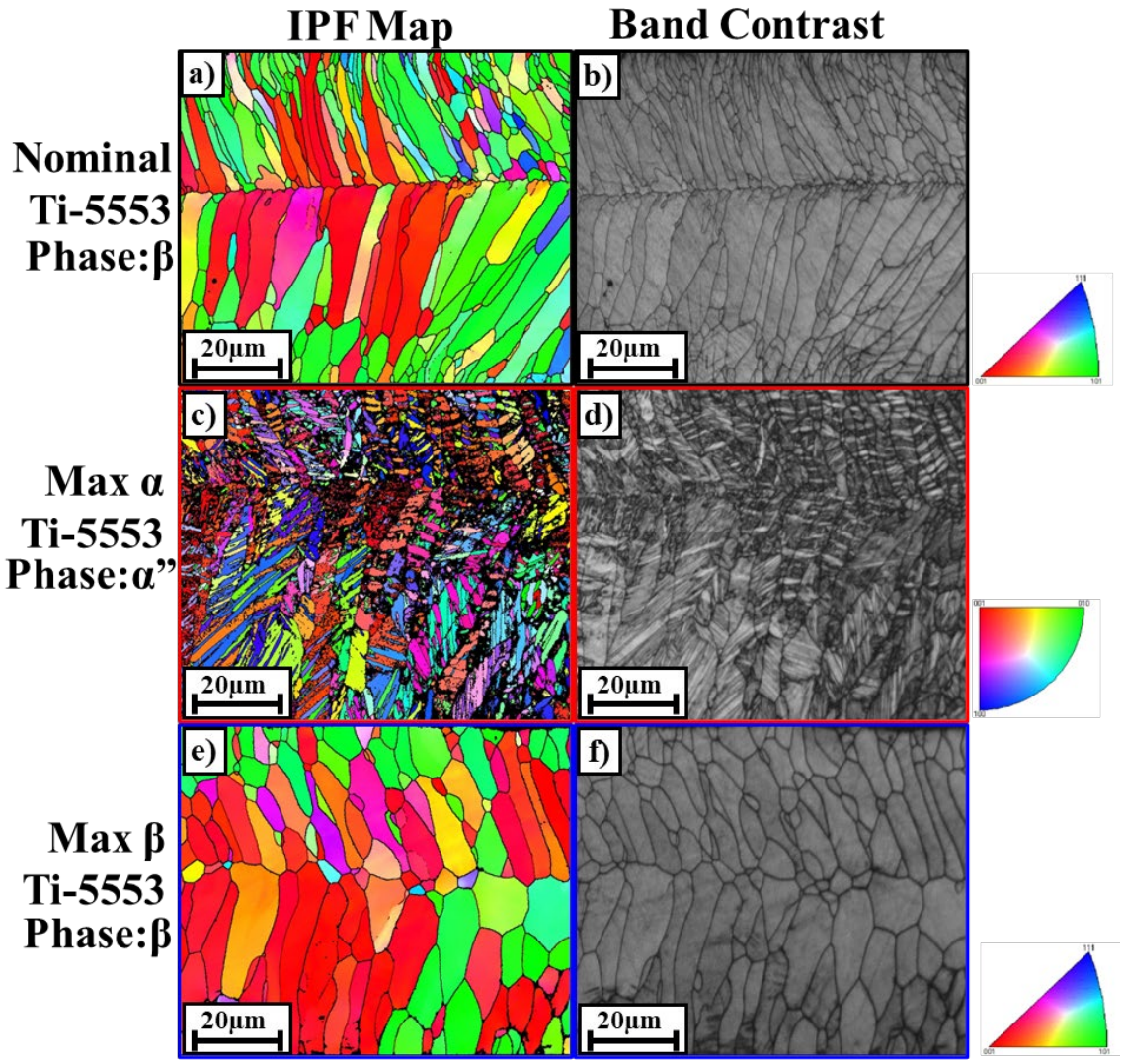

Figure 3.6 EBSD maps of a cross section of the splat quenched samples for three alloys (nominal, max α, and max β) in both IPF, oriented along the solidification direction, and band contrast allowing for the ability to see the grain structure and preferential solidification texture. The top and bottom figure are indexed using a cubic IPF map for the BCC phase and the central map is indexed using the orthorhombic α” structure. The prior beta grains can be seen in the band contrast map to resemble those seen in the other samples as the martensite forms well below the solidifications range of the alloy.

3.4.0 Discussion

3.4.1 Compositional Variation on Crystallographic Structure

The results of this study indicate that there is a sensitivity for martensitic transformation at the lower beta stabilized edge of the compositional range of Ti-5553 alloy space allowable for AM. The use of the splat quenching technique allowed for a screening over a significant compositional range of the titanium alloy. The formation of martensite in titanium alloys when quenched is not uncommon at lower Mo_{eq} values, typically below a value of 8 has a potential for martensite development but this is highly dependent on the solute added, and has been studied significantly [8,12]. As Ti-5553 is a metastable beta alloy, it logically follows that at the least beta stabilized corner of the composition specification, that the alloy would be more susceptible to α" martensite developing either upon quenching or stress-induced as was validated by this current study.

When examining the evolution of lattice parameters with composition, there are noticeable differences in what would be predicted from literature values and the crystallographic changes measured in XRD. The orthorhombic structure has only seen significant experimental study in the area of binary alloys such as Ti-V, Ti-Mo, Ti-Nb, and Ti-Ta [24]. Across the literature, studies on titanium binary alloys for several of the solutes such as Cr, Fe, and Al do not result in the creation of the α" with the likes of Ti-Cr resulting in untransformed β and ω formation instead of a transition in the structure of the α" martensite [11,15,16,24]. This means that for several of the solute additions in Ti-5553 there is limited information on their influence of the orthorhombic structure. There is some limited data on the α" structure in ternary or quaternary form such as Ti-V-Al-Fe [24] but limited data correlating composition on the effect of solute on the crystallographic

tendencies. Using values from literature, an estimate for the crystallographic structure sensitivity on solute type and concentration can be expressed for both α" and β as Eqn. 3-6 [8].

$$a_{\alpha"} = 2.89 + 3x_{Mo} + x_v + 3x_{Cr} + 0.083x_{Al} + 0.0223x_{Fe}\text{Å} \quad (3)$$

$$b_{\alpha"} = 5.20 - 5.20x_{Mo} - 1.73x_v - 5.67x_{Cr} - 0.018x_{Al} + 0.0504x_{Fe}\text{Å} \quad (4)$$

$$c_{\alpha"} = 4.734 - 1.5x_{Mo} + +0.4x_v - 2.67x_{Cr} - 0.0535x_{Al} - 0.0326x_{Fe}\text{Å} \quad (5)$$

$$a_{\beta} = 3.274 - 0.1259x_{Mo} - 0.2x_v - 0.55x_{Fe} - 0.4x_{Cr}\text{Å} \quad (6)$$

The values calculated for these parameters are displayed in Figure 3.7 alongside the measured values from XRD for both BCC and orthorhombic unit cells. The BCC lattice parameter is largely in agreement with the experimental results. The average difference from XRD measurement was found to be 0.035%, potentially due to the fact that the values used in estimating the lattice parameter are derived from binary alloys. The orthorhombic structure, however, has significant disparities in the structure as compared to the estimate. While this difference could be an effect of the retained BCC structure, the retention of some amount of BCC has commonly been seen in studies of the α" phase [24]. In both the binary alloys, tested from literature, and the current Ti-5553 modified alloys, the $c_{\alpha"}$ and $b_{\alpha"}$ lattice parameters decrease while the $a_{\alpha"}$ parameter increases as the solute increases. At higher Mo_{eq} the predicted $c_{\alpha"}$ and $b_{\alpha"}$ parameters overlap with the experimental values while the $a_{\alpha"}$ remains displaced from the prediction. Fitting the data using multiple linear regression with the QEDS composition for each alloy allows for observing the trends, Eqn. 7-9, between the crystallographic changes that are observed in this alloy as compared to the literature equations.

$$a_{\alpha"} = 3.016 + 0.018Al_{wt\%} + 0.025V_{wt\%} - 0.009Mo_{wt\%} - 0.086Cr_{wt\%} - 0.120Fe_{wt\%} \quad (7)$$

$$b_{\alpha"} = 5.767 - 0.017Al_{wt\%} - 0.009V_{wt\%} - 0.064Mo_{wt\%_{Mo}} - 0.216Cr_{wt\%} - 0.027Fe_{wt\%} \quad (8)$$

$$c_{\alpha"} = 5.233 - 0.020Al_{wt\%} - 0.012V_{wt\%} - 0.021Mo_{wt\%} - .019Cr_{wt\%} - 0.307Fe_{wt\%} \quad (9)$$

Fitting the data this way demonstrates some similarities to what has been seen in the literature on binary alloys such as no significant effect of aluminum on $c_{\alpha''}$ but generally the lack of data on multi-component α" alloys as well as the effect of chromium and iron on the orthorhombic structure means that the crystallographic changes in this compositional space are difficult to predict. There are several possibilities for the error namely being the binary data relies on the breakdown of the HCP phase at atomic percentages of 9% for vanadium or 4-6% for molybdenum while in the current case there is around 18 at% solute addition in the case for α" appearance [10]. Additionally, the reliance on QEDS also introduces error into the true composition of the alloys. When examining the coefficients of Eqn. 7-9, it is interesting to note the strong relationship between the lattice parameter and the iron and chromium content as they are two of the solutes that do not form α" in a titanium binary.

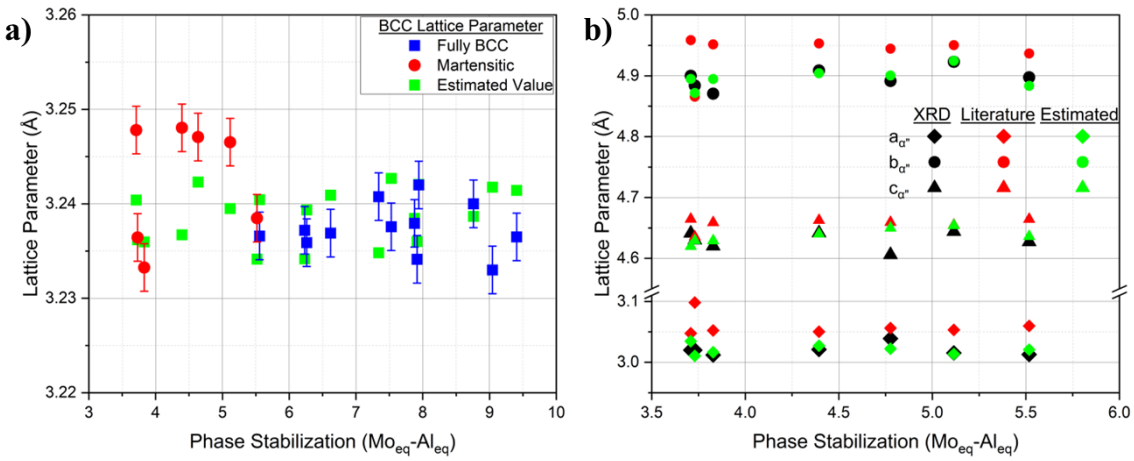

Figure 3.7 Measured lattice parameters for each splat quenched alloy compared to estimated values from literature equations for (a) BCC and (b) Orthorhombic α". Due to the poor fitting of the α" to literature equations (Eqn 3-5) a fit of the data has been performed and added as a comparison point in the difference (Eqn 7-9).

3.4.2 Predictive Capability of Martensitic Criterion

Martensite developing from quenching has clearly been established to occur in a compositional region near the Ti-5553 alloy space and developing a metric to predict its formation will deepen the understanding of the connection between composition of the alloy and its phase stability. In turn, this connection will provide us with a more accurate prediction of solidification microstructures that could occur during additive manufacturing or laser welding of this titanium alloy. There are numerous criteria developed throughout literature that have been constructed to evaluate certain regions of stability in titanium alloy development. The first is the previously established Mo_{eq} that has significant relevancy when looking at equilibrium α and β content. Another similar method involves calculating the average valence electrons per atom in the alloy as this value has been correlated to stability of the BCC lattice [12,25,26]. Beyond a simple linear combination, mapping based on solid state physics parameters as proposed by Morinaga et al. [27] has been used to build empirically derived map (Bo-Md map) of the structural stability of titanium alloys. In this model, each solute is a vector in the Bo-Md space allowing for more refined delineation in the effect of a solute then just a scalar coefficient. And the final two methods that will be compared are the martensitic start temperature and a martensitic nucleation parameter. Work throughout literature has developed methods that allow for thermodynamic simulation using CALPHAD along with the understanding of α" growth in the BCC material to predict the start temperature for martensite as well as a martensitic nucleation parameter that allows for calculation of a driving force for breaking down the BCC structure[8,28,29].

The molybdenum equivalency and valence electron per atom (e/a) methods are not able to cleanly separate the martensitic and retained BCC alloys in the current compositional space. The molybdenum equivalency is a widely used technique across academic studies and industrial

applications as a metric to understand BCC stabilization and the associated amount of β phases expected at room temperature [23,30]. This model consists of an empirically derived coefficient of stability with the namesake molybdenum having a value of unity with HCP stabilizers being subtracted with aluminum also having a value of unity. There is no great agreement on the coefficients to use as the stability with numerous equations being provided throughout literature [23,30–32]. While a clear separation does occur in Figure 3.4b, this does not acknowledge the effect of aluminum that a typical Mo_{eq} approach would advise has a significant effect on the stability of BCC. However, from the compositions tested in this study, the aluminum content was not seen to have a significant effect on martensite formation. In comparison, the stability of the BCC phase has also been correlated to the valence electron per atom ratio, e/a, especially in applications such as quenching or AM where there is limited time for diffusional segregation unlike post-heat treated components[25]. The valence electrons for each individual element are given in Table 3. with the e/a value being a sum of the individual atomic fractions multiplied by the number of valence electrons. Calculating the two values for each alloy, Table 2, demonstrates that the molybdenum equivalency and valence electron per atom techniques share similar qualities in that there is a general ability to separate a vast majority of the alloys but there is overlap at the center. This was repeated for several widely used Mo_{eq} equations but there was no change to the result [31,32]. As such, the Mo equivalency and Bo-Md map techniques can be seen to be useful as tools for providing insight into BCC stabilization, but they have difficulty separating out regions in the metastable beta alloy group. Additionally, there are certain weakness in the two techniques with Mo_{eq} incorrectly predicting the effect of oxygen on martensitic stability, and the e/a does not account for interstitial additions as the technique has only been used for substitutional solute additions. Studies have largely shown that oxygen has a complicated relationship with the

formation of martensite in beta stabilized titanium alloys with the ability to suppress the martensite formation [33].

Table 3.3 Criterion parameters for use in titanium alloys with bond order (Bo), metal d-orbital energy (Md), and room temperature shear modulus (μ_{rt})

Element	Valence Electron	Bo [4]	Md (eV) [4]	μ_{RT} (GPa) [34]
Ti	4	2.79	2.45	28.3
Al	3	2.43	2.20	25.0
V	5	2.81	1.87	43.2
Mo	6	3.06	1.96	109.2
Cr	6	2.78	1.48	99.0
Fe	8	2.65	0.97	116.0

The Bo-Md map has seen increasing use in titanium alloy design but due to the complexity of the transition region between fully stable BCC and HCP martensite, this approach has few, well-defined delineations that can be used to separate out the current alloys. The unique mechanical properties of unstable BCC titanium alloys such as super elasticity, TRIP (transformation induced plasticity), TWIP (twinning induced plasticity), and shape memory alloy properties has led to a growing body of empirical data of titanium alloys in the Bo-Md space, where Bo is the bond order, a measure of covalent bond strength between titanium and the solute, and Md is the metal d-orbital energy level that correlates with electronegativity and metallic radius of the solute atoms [27]. The increasing use of the Bo-Md maps is due to the ability to estimate the properties of the BCC phase including elastic properties and deformation mechanisms [4,9,11,27]. The values for each of the solutes is given in Table 3. Examination of the map with the created alloys for this paper placed on it reveals that the Ti-5553 system is on the border of the martensitic to TRIP space, Figure 3.8b. This position follows with what is known in literature as the as-quenched Ti-5553 alloy does form stress induced martensite in its nominal composition [35]. In the current study, the alloys can form martensite if the beta stabilization is reduced. Another interesting result of this map is that it can

capture both as-quenched samples with limited segregation, as well as, heat treated or cast samples that have a larger compositional variation throughout the material by plotting the different regions of the material as discrete points in the space to see the effect of segregation on the stability regions of the material [36]. Its limitations are largely due to the borders between different regions being fuzzy, so using the method to define borders in the regions such as Ti-5553 are difficult. Additionally, the model has an inherent inability to correlate interstitial atoms such as oxygen to a change in either structural parameter besides qualitative observations that oxygen increases the stability of the BCC phase [2].

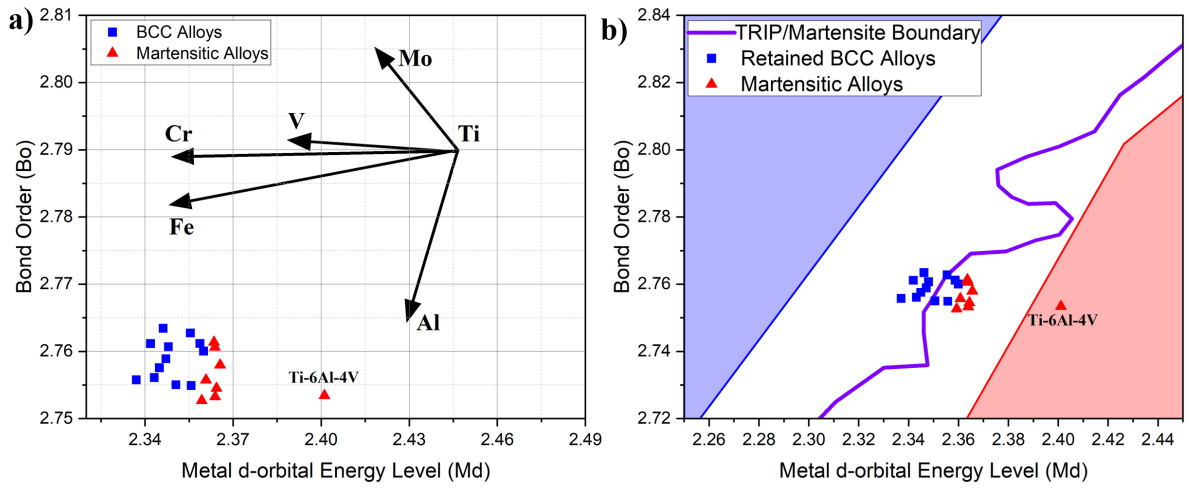

Figure 3.8 Plot of the current Ti-5553 alloys (red and blue symbols) on a Bo-Md plot with (a) the vectors outlined for the solutes from the origin point of pure titanium with the current alloys highlighted as well as Ti-6Al-4V for comparison and a (b) map with empirical boundaries for the stable BCC and HCP regions along with the TRIP/Martensite boundary from literature[8]. The complicated nature of martensitic break down from martensite to TRIP (retained BCC) is shown by the torturous border [8,37] between the two regions on the Bo-Md map.

Adapted from work on ferritic martensite, the use of a martensitic start temperatures, M_s, allows for the separation of martensitic and retained BCC alloys in the current study, while maintaining the ease of models such as the molybdenum equivalency. Interestingly, the M_s temperature of the retained BCC still has a value above room temperature. Therefore, the M_s of alloys that do not form martensite is difficult to predict without experimental observations, such as in the current work, as the change from martensitic to TRIP has been shown to vary with the composition of the alloy [38]. Martensitic start temperature has been used as a means for the study of stress-induced martensite and thermal martensite in titanium alloys [8,28,38]. Various methods have been used to predict the martensitic start temperature such as equating the driving force to form martensite as the combination of the elastic strain energy needed to change shape plus the strains introduced by solute additions to the matrix [29]. Other methods focus on volumetric energy introduced by an finite sized region of martensite as well as the interfacial energy needed for the creation of the parent-martensite interface [8].There are more additional methods than the two discussed above, but all attempts result in a estimation of the energy needed to create the martensitic phases coupled with the use of a CALPHAD software to correlate the energy needed for the Gibbs free energy difference between the HCP and BCC phase to estimate a temperature for the development of the martensite. These methods also allow for the creation of equation that can correlate the compositions to the martensitic start temperature such as in Eqn. 10 [8,28,29].

$$M_s = 1156 - 150Fe_{wt\%} - 96Cr_{wt\%} - 49Mo_{wt\%} - 37V_{wt\%} + 15Al_{wt\%} \quad (10)$$

The plot of the M_s temperature versus Mo_{eq} exhibits a *separation between the martensitic and retained BCC alloys at 570°C* . The use of this parameter therefore has a value that can then be used to model a threshold that needs to be met for the splat quenched alloy to retain full BCC structure. The use of this model is fairly accurate as an estimation even for multi-component

systems [28], but this limited form does have certain weaknesses in use. The first is that there is not a term used to address the effect of oxygen. The second point to mention is due to the ability for TRIP titanium alloys to have a martensitic start temperature above room temperature while retaining the BCC phase upon quenching. As such, experimentation such as the current study is needed to validate the M_s value that correlates to an actual transition in the BCC stability.

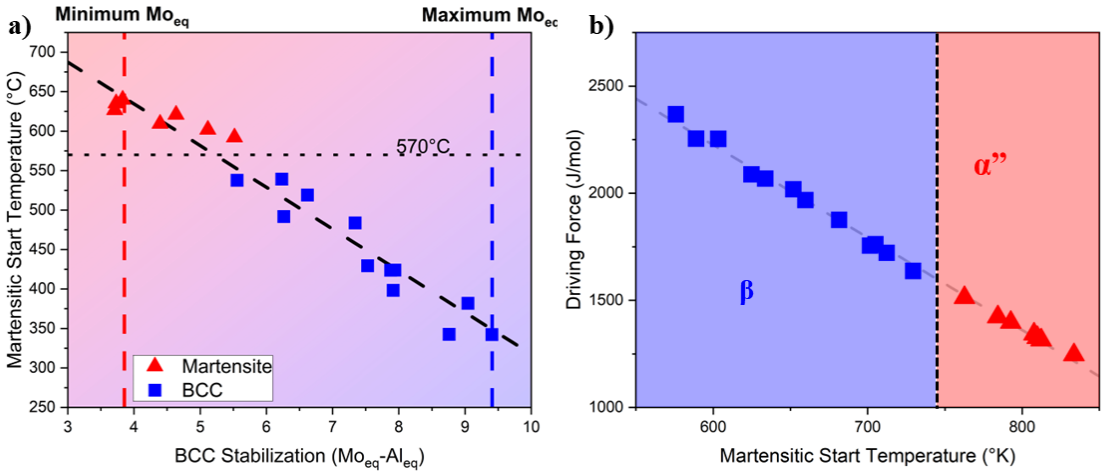

Figure 3.9 (a) Martensitic start temperature correlated to molybdenum equivalency for the Ti-5553 based alloys with delineation for the edges of the AMS 7026 composition standard. (b) Driving force derived from CALPHAD simulation between the BCC and HCP phases at the predicted martensitic start temperature start temperature demonstrating increased energy needed to nucleate the HCP phase at lower M_s values.

To provide a clearer transition across larger alloy spaces, further models have been developed to address TRIP materials that create a parameter for the driving force to nucleate martensite that incorporate CALPHAD as well as the kinetics of nucleating martensite to provide a criterion for the breakdown of the BCC lattice upon quenching. The model described in detail by Bignon et al.[8] results in an Eqn. 11.

$$\frac{kT_0}{\mu(T_0)b^3} > \frac{\chi}{\ln\left(\frac{N_0 Q_0}{N_m Q}\right)} \qquad (11)$$

Where χ is a constant independent from the composition that relates to the energy to dissociate a $\frac{1}{2}[111]$ dislocation into three partials that have been identified as the first step of the BCC to HCP transition. The orthorhombic martensite follows the same pathway except cannot complete the transition to HCP, so the model has been applied to α" as well as α'.The burger vector b of the screw dislocation is calculated as $\frac{1}{2}\sqrt{3}a_\beta$. The partitionless equilibrium temperature, T_0, is calculated through CALPHAD and $\mu(T_0)$ is the shear modulus calculated at the T_0 temperature. N_0 is the number of potential martensite nucleation sites and N_m is the critical number of locations needed to form the martensite. And lastly, Q is the cooling rate during the quench, Q_0 is the temperature range during cooling multiplied by the vibrational frequency, f_0, at T_0, and k is the Boltzmann constant. This relationship in Eqn. 11. established on the LHS is a ratio of the available thermal energy at the T_0 temperature where the BCC and HCP phases are in equilibrium and the energy required for nucleation. The RHS of Eqn. 11. then is compositionally invariant and can be used as a martensitic criterion. In literature, a value of the LHS below $1.24 \cdot 10^{-2}$ has been set as the criterion needed for repression of the martensite.

The use of T_0 as a parameter from CALPHAD allows the ease of incorporating interstitial elements such as oxygen into a predictive tool to understand the likelihood of martensite formation. The effect of oxygen on T_0 can be seen in the change of the curve in Figure 3.10 that correlate to the repression of martensitic development that has been seen in oxygen. When plotted the T_0 curve reveals the same discrete transition between the martensitic and retained BCC alloys that was displayed by the martensitic temperature on current and literature alloys. What can also be seen when calculating this value with and without oxygen addition is that the oxygen actually lowers

the equilibrium temperature between the BCC and HCP phases thereby providing stabilization against martensitic development as compared to in the Mo_{eq} where it has been seen that oxygen increases the α phase content. Figure 3.10b demonstrates the effect of compositional fluctuations away from nominal Ti-5AL-5V-5Mo-3Cr-0.4Fe on the T_0 temperature for each alloy as simulated by TCTI5. The strongest solute for driving down the T_0 temperature and thereby reducing the ability for martensitic development is oxygen followed by iron with only aluminum increasing the driving force for martensite but at a smaller slope than any of the other solutes. The strength of oxygen in controlling martensitic transition does mean that variance in the oxygen content between samples may play a part in the control of the transition with higher levels of oxygen may further stabilize the BCC phase even at alloy below the AMS 7026 standard beta stabilizer content. The resulting conclusion is that in terms of as-quenched microstructural stability, Ti-5553 is sensitive to martensite especially at low oxygen content with beta stabilizer fluctuations being more important than HCP stabilizer fluctuations at controlling martensite development.

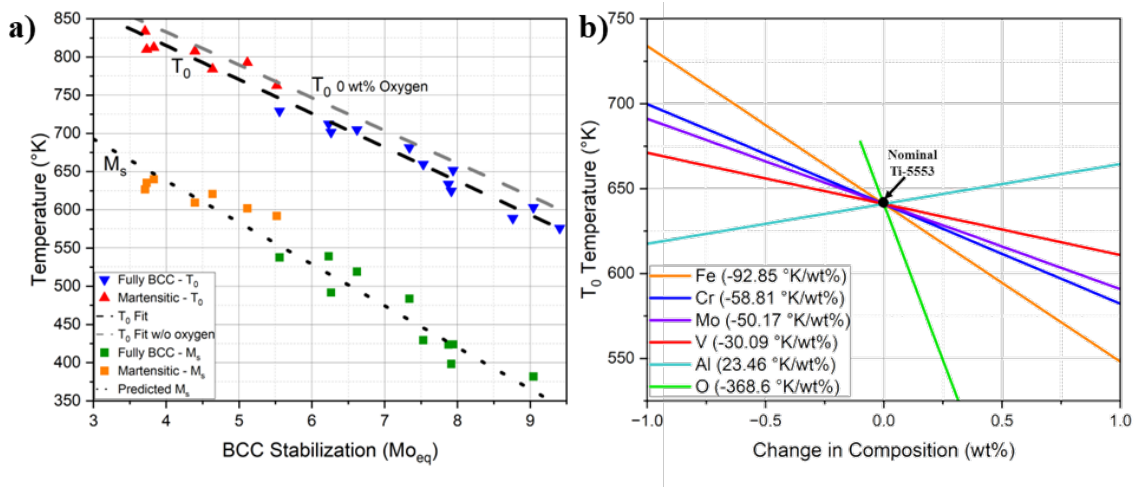

Figure 3.10 (a) T_0 temperature as a function of BCC stabilization highlighting the effect removing oxygen on T_0 and highlighting the difference in the martensitic start temperature and T_0. (b) Plot of the effects of composition variation on the T_0 values as a function of the various solutes in Ti-5553 demonstrating the significant effect of oxygen and beta solutes.

The shear modulus at the T_0 temperature, $\mu(T_0)$, used in Eqn. 11. was estimated using the method outlined in Galindo-Nava, Eqn. 12 [8,29], where v is Poisson ratio that is taken to be 1/3 for all alloys.

$$\Delta\mu_{temp} = \frac{1}{\mu_{RT}2(1+v)}(119.4\text{-}0.07193(T\text{-}273)) \text{ GPa} \quad (12)$$

This change due to temperature however does not have a compositional component. An estimation of the modulus was done using a rule of mixtures from pure elemental values of shear modulus, Eqn. 13, displayed in Table 3 [34]. This results in an estimated value that can be applied to titanium alloys that have limited shear modulus data to inform model calibration.

$$\Delta\mu_{comp} = \frac{\mu_{alloy}}{\mu_{Ti}} = \frac{1}{\mu_{Ti}}(\mu_{Ti} + \sum_i(\mu_i - \mu_{Ti})x_i) \quad (13)$$

The results from Eqn. 12 and 13 can then be multiplied to give an estimated shear value for the composition at the T_0 temperature. Additionally, there have been studies that have captured the shear modulus increases due to measured upticks in oxygen that have found that that the oxygen increases the Youngs modulus linearly[39]. To that effect, an estimate of the shear modulus estimated shear modulus for the alloy in Eqn. 14.

$$\mu_{alloy} = (\Delta\mu_{temp}\Delta\mu_{comp})\mu_{Ti} + 5.06x_{wt\%Oxy} \quad (14)$$

With the shear modulus and burgers vector calculated from the BCC lattice parameter, the nucleation parameter can be calculated. The transition is in the region of nucleation parameter equaling $1.425\cdot10^{-2}$. This is higher than the $1.24\cdot10^{-2}$ [8] that was found in a previous study but a higher amount of oxygen would lower the T_0 temperature which likely means that the variation in the value from literature could be due to incorporating the effect of oxygen into the thermodynamic calculation. Plotting of the T_0 temperature and the nucleation parameter demonstrate a linear

relationship due to the limited variation in the shear modulus and lattice parameter that would vary more significantly across larger composition changes.

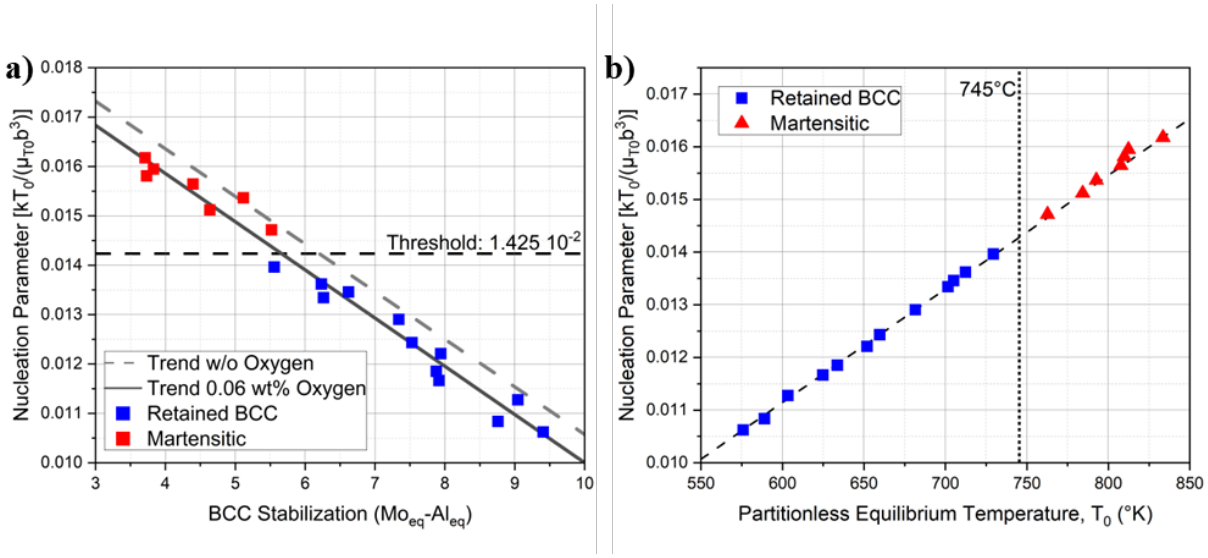

Figure 3.11 (a) Martensitic nucleation parameter as a function of BCC stabilization of the Ti-5553 alloys highlighting the experimentally determined threshold for forming martensite across the Ti-5553 based alloys as well as the effect of oxygen in lowering alloys toward BCC stabilization. (b) Plot highlighting the potential for T0 as a martensitic predictor due to the limited deviation between nucleation parameter and T0.

The methods evaluated in this work have all been previously used in literature as a metric to evaluate the BCC stability in titanium alloys. The current work has found that there is limited sensitivity in the Ti-5553 alloy space, as outlined by AMS 7026, to form martensite upon quenching. As such, this work outlined and used various martensite formation criteria to evaluate their ability to distinguishing martensitic compositions in the metastable β allow space with focus on the predictive ability, ease of implementation, and ability to incorporate the effect of oxygen on martensitic repression. Thereby providing a review and analysis of martensitic criteria in the

titanium alloy system in addition to providing a criterion for avoiding martensite when designing new metastable beta titanium alloys through the use of compositional stability.

3.5.0 Conclusion

In this paper, the stability of the BCC phase in Ti-5553 over its compositional range was investigated through the splat quenching process. Correlation of crystallographic structure to composition was conducted using x-ray diffraction and quantitative x-ray energy dispersive spectroscopy. Following characterization, predictive martensite formation models from literature were examined including molybdenum equivalency, valence electron to atom ratio, martensitic start temperature, and martensitic nucleation parameter to evaluate the strengths and weaknesses of each model for use in outlining a separation from martensitic to retained BCC upon quench. Based on this analysis, we have learned the following:

- In the AMS 7026 composition specification for Ti5553, there was not found to be any sensitivity to martensite formation upon rapid solidification and quenching with the loss of beta stabilizers being more impactful than the aluminum content.
- The experimentally observed space group of the orthorhombic α" martensite (S.G. 63, Cmcm) was found to match literature values for binary Ti-X alloys, but a direct correlation between composition and lattice parameters for this space group was complicated due to the complexity of the solute interaction on the orthorhombic structure deviating from what was expected from binary additions.
- The use of molybdenum equivalency equations and valence electron per atom models all result in phase stability predictions which overlap the experimentally observed retained BCC and martensitic microstructures, resulting in significant uncertainty for the quenched structure in an intermediary, compositional range. Interestingly, the Mo_{eq} method was able

to separate the currently studied alloys if the aluminum and oxygen contributions were removed.

- The use of martensitic start temperature (M_s) successfully separated the two groups of alloys using only the alloy composition. Outside of the current study there is limited information to designate a M_s temperature that would separate the martensitic and retained BCC alloys. The difficulty in using M_S as a generalized delineator is due to the transition value being an alloy specific parameter that varies with compositional changes.
- A model created to correlate the stability in terms of the available energy in compared to the energy barrier to nucleate martensite as a function of composition was also implemented. The model was found to successfully separate the martensitic and retained BCC alloys and provide a more widely useful transition limit. The benefit of this model includes incorporation of the damping effect of oxygen on martensite development as well as providing a clear transition across the titanium alloy space.

References

[1] M. Morinaga, Y. Murata, H. Yukawa, Alloy design based on the DV-Xα cluster method, Springer Ser. Mater. Sci. 84 (2006) 23–48. https://doi.org/10.1007/3-540-31297-8_2.

[2] M. Abdel-Hady, K. Hinoshita, M. Morinaga, General approach to phase stability and elastic properties of β-type Ti-alloys using electronic parameters, Scr. Mater. 55 (2006) 477–480. https://doi.org/10.1016/J.SCRIPTAMAT.2006.04.022.

[3] Y. Liu, L. Xu, C. Qiu, Development of an additively manufactured metastable beta titanium alloy with a fully equiaxed grain structure and ultrahigh yield strength, Addit. Manuf. 60 (2022) 103208. https://doi.org/10.1016/j.addma.2022.103208.

[4] D. Kuroda, M. Niinomi, M. Morinaga, Y. Kato, T. Yashiro, Design and mechanical properties of new β type titanium alloys for implant materials, Mater. Sci. Eng. A. 243 (1998) 244–249. https://doi.org/10.1016/s0921-5093(97)00808-3.

[5] R.P. Kolli, W.J. Joost, S. Ankem, Phase Stability and Stress-Induced Transformations in Beta Titanium Alloys, Jom. 67 (2015) 1273–1280. https://doi.org/10.1007/s11837-015-1411-y.

[6] M. Marteleur, F. Sun, T. Gloriant, P. Vermaut, P.J. Jacques, F. Prima, On the design of new β-metastable titanium alloys with improved work hardening rate thanks to simultaneous TRIP and TWIP effects, Scr. Mater. 66 (2012) 749–752. https://doi.org/10.1016/j.scriptamat.2012.01.049.

[7] K. Shitara, K. Yokota, M. Yoshiya, J. Umeda, K. Kondoh, First-principles design and experimental validation of β-Ti alloys with high solid-solution strengthening and low elasticities, Mater. Sci. Eng. A. 843 (2022) 143053. https://doi.org/10.1016/j.msea.2022.143053.

[8] M. Bignon, E. Bertrand, F. Tancret, P.E.J. Rivera-Díaz-del-Castillo, Modelling martensitic transformation in titanium alloys: The influence of temperature and deformation, Materialia. 7 (2019) 100382. https://doi.org/10.1016/j.mtla.2019.100382.

[9] Y. Zheng, R. Banerjee, Y. Wang, H. Fraser, D. Banerjee, Pathways to Titanium Martensite, Trans. Indian Inst. Met. 75 (2022) 1051–1068. https://doi.org/10.1007/S12666-022-02559-9/FIGURES/19.

[10] A. V. Dobromyslov, V.A. Elkin, The orthorhombic α″-phase in binary titanium-base alloys with d-metals of V-VIII groups, Mater. Sci. Eng. A. 438–440 (2006) 324–326. https://doi.org/10.1016/j.msea.2006.02.086.

[11] M. Bignon, E. Bertrand, P.E.J. Rivera-Díaz-del-Castillo, F. Tancret, Martensite formation in titanium alloys: Crystallographic and compositional effects, J. Alloys Compd. 872 (2021) 159636. https://doi.org/10.1016/j.jallcom.2021.159636.

[12] M. Bönisch, M. Calin, L. Giebeler, A. Helth, A. Gebert, W. Skrotzki, J. Eckert, Composition-dependent magnitude of atomic shuffles in Ti-Nb martensites, J. Appl. Crystallogr. 47 (2014) 1374–1379. https://doi.org/10.1107/S1600576714012576.

[13] H.M. Flower, S.D. Henry, D.R.F. West, The β ⇄ α transformation in dilute Ti-Mo alloys, J. Mater. Sci. 9 (1974) 57–64. https://doi.org/10.1007/BF00554755.

[14] R. Davis, H.M. Flower, D.R.F. West, Martensitic transformations in Ti-Mo alloys, J. Mater. Sci. 14 (1979) 712–722. https://doi.org/10.1007/BF00772735.

[15] R. Ray, B.C. Giessen, N.J. Grant, The constitution of metastable titanium-rich Ti-Fe alloys:An order-disorder transition, Metall. Trans. 3 (1972) 627–629. https://doi.org/10.1007/BF02642743.

[16] R.H. Ericksen, R. Taggart, D.H. Polonis, The martensite transformation in Ti-Cr binary alloys, Acta Metall. 17 (1969) 553–564. https://doi.org/10.1016/0001-6160(69)90114-X.

[17] A.M.S.A.M.A.M. Metals, Titanium Ti-5553 (Ti - 5Al - 5Mo - 5V - 3Cr) Powder for Additive Manufacturing, (2021). https://doi.org/https://doi.org/10.4271/AMS7026.

[18] R. Seshadri, R. V. Krishna Rao, R. V. Krishnan, R.M. Mallya, Electron-beam melting and centrifugal splat-quenching technique for rapid solidification of titanium alloys, J. Mater.

Sci. 23 (1988) 1637–1642. https://doi.org/10.1007/BF01115702.

[19] D.B. Snow, Investigation of Rapidly-Solidified Dispersion Strengthened Titanium Alloys, 1987.

[20] F.H. Froes, R.G. Rowe, RAPIDLY SOLIDIFIED TITANIUM, Mater. Res. Soc. (1986).

[21] Z.A. Hasenbusch, A. Deal, B. Brown, L. Nastac, N. Luke, Z.A. Hasenbusch, A. Deal, B. Brown, L. Nastac, L.N. Brewer, Microstructural and Nanostructural Evolution in Splat Quenched Stainless Steels Microstructural and Nanostructural Evolution in Splat Quenched Stainless Steels, (n.d.).

[22] T.W. Clyne, A. Garcia, The application of a new solidification heat flow model to splat cooling, J. Mater. Sci. 16 (1981) 1643–1653. https://doi.org/10.1007/BF02396883.

[23] E.W. Collings, The Physical Metallurgy of Titanium Alloys, American Society for Metals, 1984. https://books.google.com/books?id=PtRTAAAAMAAJ.

[24] J.Y. Yan, G.B. Olson, Molar volumes of bcc, hcp, and orthorhombic Ti-base solid solutions at room temperature, Calphad Comput. Coupling Phase Diagrams Thermochem. 52 (2016) 152–158. https://doi.org/10.1016/j.calphad.2016.01.003.

[25] A. V. Dobromyslov, V.A. Elkin, Martensitic transformation and metastable β-phase in binary titanium alloys with d-metals of 4-6 periods, J. Phys. IV JP. 112 II (2003) 723–726. https://doi.org/10.1051/jp4:2003984.

[26] X.H. Min, S. Emura, T. Nishimura, K. Tsuchiya, K. Tsuzaki, Microstructure, tensile deformation mode and crevice corrosion resistance in Ti-10Mo-xFe alloys, Mater. Sci. Eng. A. 527 (2010) 5499–5506. https://doi.org/10.1016/j.msea.2010.06.016.

[27] M. Morinaga, M. Kato, T. Kamimura, M. Fukumoto, I. Harada, K. Kubo, Theoretical Design of beta-Type Titanium Alloys, Miner. Met. Mater. Soc. (1993).

[28] S. Neelakantan, P.E.J. Rivera-Díaz-del-Castillo, S. van der Zwaag, Prediction of the martensite start temperature for β titanium alloys as a function of composition, Scr. Mater. 60 (2009) 611–614. https://doi.org/10.1016/j.scriptamat.2008.12.034.

[29] E.I. Galindo-Nava, On the prediction of martensite formation in metals, Scr. Mater. 138 (2017) 6–11. https://doi.org/10.1016/j.scriptamat.2017.05.026.

[30] G. Lutjering, J.C. Williams, Titanium, 1990. https://doi.org/10.5005/jp/books/11706_12.

[31] J.D. Cotton, R.D. Briggs, R.R. Boyer, S. Tamirisakandala, P. Russo, N. Shchetnikov, J.C. Fanning, State of the Art in Beta Titanium Alloys for Airframe Applications, Jom. 67 (2015) 1281–1303. https://doi.org/10.1007/s11837-015-1442-4.

[32] K. Ishida, Schaeffler-Type Phase Diagram of Ti-Based Alloys, Metall. Mater. Trans. A Phys. Metall. Mater. Sci. 48 (2017) 4990–4998. https://doi.org/10.1007/s11661-017-4218-

3.

[33] S. Kawano, S. Kobayashi, S. Okano, Effect of oxygen addition on the formation of α'' martensite and athermal ω in TiNb alloys, Mater. Trans. 60 (2019) 1842–1849. https://doi.org/10.2320/matertrans.ME201908.

[34] H.P.R. Frederikse, Elastic Constants of Single Crystals General References, CRC Handb. Chem. Phys. (2013) (12)35-(12)40.

[35] A. Zafari, K. Xia, Stress induced martensitic transformation in metastable β Ti-5Al-5Mo-5V-3Cr alloy: Triggering stress and interaction with deformation bands, Mater. Sci. Eng. A. 724 (2018) 75–79. https://doi.org/10.1016/j.msea.2018.03.070.

[36] C.H. Ng, M.J. Bermingham, L. Yuan, M.S. Dargusch, Towards β-fleck defect free additively manufactured titanium alloys by promoting the columnar to equiaxed transition and grain refinement, Acta Mater. 224 (2022) 117511. https://doi.org/10.1016/J.ACTAMAT.2021.117511.

[37] M. Abdel-Hady, K. Hinoshita, M. Morinaga, General approach to phase stability and elastic properties of β-type Ti-alloys using electronic parameters, Scr. Mater. 55 (2006) 477–480. https://doi.org/10.1016/j.scriptamat.2006.04.022.

[38] C. Li, J.H. Chen, X. Wu, W. Wang, S. Van Der Zwaag, Tuning the stress induced martensitic formation in titanium alloys by alloy design, J. Mater. Sci. 47 (2012) 4093–4100. https://doi.org/10.1007/s10853-012-6263-z.

[39] Y.T. Lee, G. Welsch, Young's modulus and damping of Ti6Al4V alloy as a function of heat treatment and oxygen concentration, Mater. Sci. Eng. A. 128 (1990) 77–89. https://doi.org/10.1016/0921-5093(90)90097-M.

CHAPTER 4 – EXPLORATION OF RAPID SOLIDIFICATION CONDITIONS ON SOLIDIFICATION MORPHOLOGY AND SOLUTE SEGREGATION IN BETA-STABILIZED TITANIUM ALLOY

C.J. Williamson[a], A. Deal[b], B. Brown[b], L. Nastac[a], L.N. Brewer[a]

[a] Department of Metallurgical and Materials Engineering, The University of Alabama, Tuscaloosa, AL 35487, USA

[b] Department of Energy's National Security Campus, Honeywell Federal Manufacturing & Technologies, Botts Road, Kansas City, MO 14520, USA

Developing and refining solidification models for titanium alloys is critical to understand and predict the material response at rapid solidification conditions as seen in additive manufacturing and welding processes. The use of analytical models and numerical simulations allowed for correlation between key microstructural features such as solute segregation, grain morphology, and solidification structure with the thermal history (cooling rate, solidification velocity and thermal gradient). The properties and thermal history of laser welds, splat quenched samples, and plasma atomized powder of beta titanium alloy Ti-5553 are investigated through the use of rapid solidification experiments, electron microscopy, and thermal simulation. The segregation of the solute above a solidification velocity of 0.1 m/s was reduced with the chromium being the most agressive segregator. Planar solidification is expected to occur on the order of 1.0 m/s that was only reached with twin hammer splat quenching as the laser welds at 550 mm/s still retained a cellular structure. The end result is the ability to evaluate and calibrate the usefulness of models for columnar-equiaxed transition, velocity dependent solute partition coefficient, and solid-liquid interface stability across a suite of rapid solidification techniques.

4.1.0 Introduction

The maturation and development of additive manufacturing (AM) processes have changed the landscape of component manufacturing and processing. Fusion AM components have seen acceptance into industrial applications due to the unique geometries possible and freedom from logistical strains that accompany traditional component acquisition. In this field, titanium alloys have developed as a major alloy group due to their excellent strength to weight ratio, corrosion resistance, and biocompatibility. Traditionally, Ti-6Al-4V has dominated the marketplace making up over 50% of the titanium alloy being manufactured, and this has included into the development of AM-based research on titanium alloys [1]. Recently, beta stabilized alloys such as Ti-5553 have been developed for AM processes due to their improved printability as well as their combination of high strength and toughness [2]. Beta-stabilized titanium alloys are a group that contain a suite of solute additions that promote the retention of the BCC (β) titanium phase. As such there are numerous benefits to the use and development of new titanium alloys for the unique needs of AM processes but there are also challenges when using the higher segregating solute that require a deeper understanding of rapid solidification in titanium alloys.

Fusion based AM revolves around the melting and then re-solidification of feedstock material into what will become the final component. The specific solidification conditions heavily depend on the AM technique and parameters used but can generally be regarded as approaching rapid solidification especially in the case of laser powder bed fusion and other beam-based techniques [2–6]. Resultingly, the cooling rate and solidification velocity of the melt are significantly different then slower solidifying processes and result in changes to the solidification structure as well as the segregation profile. In casting, the solidification velocity is

comparatively low, and the formation of dendrites and significant segregation can occur causing intermetallic defects. In contrast, AM processes have the potential to reach solidification regimes that lower segregation and promote increased uniformity in composition throughout components. As such studies have examined the addition of alloy addition to promote beneficial effects in AM of titanium such as iron and yttrium as well as boron to promote equiaxed grains and reduce the anisotropy resulting from columnar grains seen in AM components[7,8].

Despite the considerable progress in applying AM to titanium alloys, the knowledge base for understanding rapid solidification, especially in titanium, is limited with much of the information on beta stabilized titanium being limited to specific applications. The amount of solidification research on titanium is generally smaller compared to other alloys groups, such as irons, steel and aluminum alloys. This is due both to the inherent difficulties in casting titanium, such as reactivity and higher melting temperature, as well as the significantly lower industrial use of cast titanium. Alloys examined for potential biomedical applications such as Ti-Nb [9,10] and Ti-Mo [11] have been processed using rapid solidification techniques to characterize the microstructure such as cell spacing and segregation. Additionally, extensive work has looked at low power density AM processes such as DED [12–14]; but the unique process of adding in unmelted powder into the melt pool has complications that result in solidification conditions that are not easily applied to other processes due the unique nucleation sites presented in the melt. As such, prediction and exploration on the effect of varying solidification conditions is limited for titanium especially when developing alloys away from the Ti-64 alloy [15].

During solidification there is an interplay between the solute diffusion and growth of the solid-liquid interface that is controlled by the solidification parameters. In rapid solidification conditions the velocity of the solid-liquid interface can approach the same order of magnitude as

the speed of the solute diffusion at the solid-liquid interface resulting in localization of diffusion and an overall reduction in segregation of the solute and coarsening of the microstructure. This parameter has been shown to be represented by the solutal Peclet number that compares the velocity of solid-liquid interface (V) to the liquid diffusion coefficient (D_i) with the cellular-dendritic tip radius (R) being the distance needed to diffuse solute. The dendritic tip radius can be estimated through models as well as be measured experimentally by values such as cell spacing of etched microstructures. As the velocity increases, the Peclet number trends upward with a value of unity or greater indicating localization of diffusion to the interface.

$$Pe_i = \frac{RV}{2D_i} \qquad (1).$$

The Peclet number is the ratio of the advective to diffusive transport and a value over unity means that the diffusion transport no longer dominates over the solidification velocity. The localization in diffusion breaks down the equilibrium at the solid liquid interface that is an assumption of models developed for casting. This breakdown in equilibrium is most easily seen in the retention of solute in the solid resulting in decreased segregation. The segregation can be estimated by the partition coefficient, k, which is the ratio of the solute composition in the solid over the composition in the liquid. Changes in the partition coefficient are fundamentally important to the understanding of the solidification structure and the sensitivity to beta fleck formation. However, understanding and modeling of the partition coefficient as a function of velocity is difficult with experimental results being even more difficult to obtain.

This paper serves to provide a stepping point to characterize and to provide predictive tools for understanding the rapidly solidified microstructure of beta stabilized titanium alloys. The current work will focus on rapid solidification of three kinds: powder atomization, splat quenching, and single laser pass remelting. Each solidification technique relies on a separate

cooling and solidification conditions profiles, Figure 1, resulting in exploration across a wide range of conditions for use in understanding the behavior of the titanium system. The use of solidification models will gather and connect characteristics that when empirically validated allow for predictions of the resulting microstructure. Models used in the current study evaluate the columnar to equiaxed transition, segregation profile, and planar stability to provide an estimate of the grain structure, cell size, and segregation that occur during solidification. The final result of this work is to provide a platform for understanding the solidified material as a tool for generating alloys and processing routes to better predict the initial state of the alloy after RS processing.

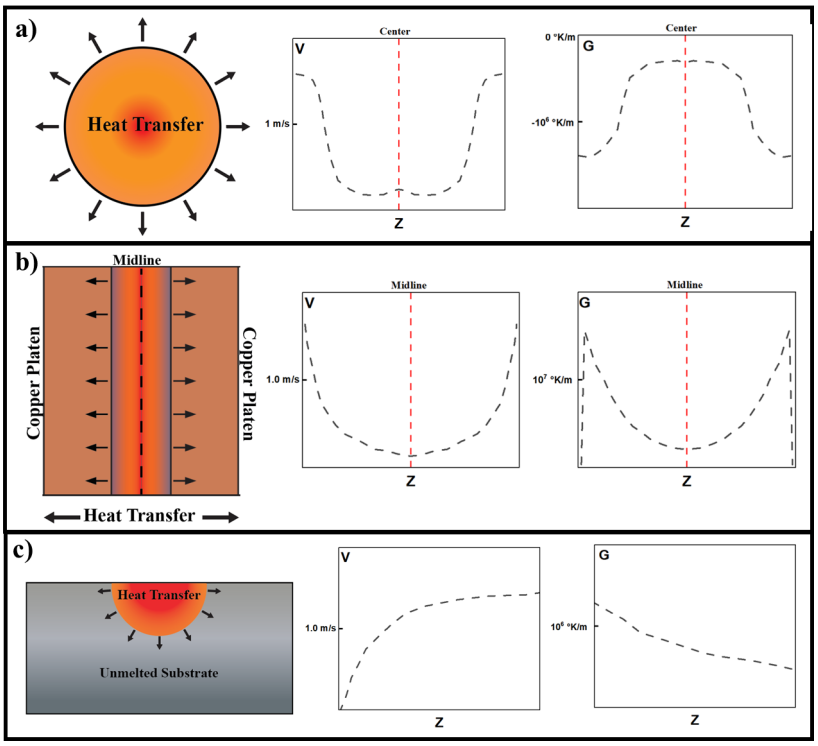

Figure 4.1 Graphical representation of the solidification conditions seen in (a) bulk undercooled atomization, (b) substrate cooled splat quenching, and (c) laser remelting with nominal profiles of the solidification velocity and thermal gradient in the material modified from [16]. The Z axis is defined as a nominal direction of heat transfer for each application (parallel to black arrows).

4.2.0 Experimental Procedures

To explore a range of cooling rates beyond the limits of a single technique, several different solidification processes were used. The first technique was atomization. The pre-alloyed powder was commercially available Ti-5553 powder created using plasma atomization. Plasma atomization displays a much lower average cooling rate then techniques such as gas atomization. The cooling in plasma atomization process relies on convective flow of a rotating rod of feedstock material in an argon atmosphere that is melted using an arc. As such, the cooling demonstrates a significant drop shortly after solidification due to the convective cooling dropping off significantly as the powder is thrown from the rod[17]. The powder analyzed in the current study was ranged in size from 20-63 μm. The other materials analyzed in this study were created by arc melting from elemental feedstock. The arc melted buttons were created using elemental feedstock (wt%=99.95%) that was melted and flipped four times to increase homogeneity. The arc melting was performed under a positive pressure ultra-high purity argon atmosphere after the chamber was backfilled four times. The arc melted buttons were then cut into pieces using a wire EDM and polished prior to processing to remove the recast layer. The arc melted pieces were then used both for splat quenching as well as single track laser welding experiments.

Splat quenching is a rapid solidification technique that uses samples that are inductively heated and containerlessly levitated[18,19]. The levitating material is then heated to a desired superheat and dropped between two projectile copper platens that result in a ~50-100 μm thick foil that is rapidly cooled in the region of 10^6-10^8 °K/s[20]. For this current study, copper platens polished to 1 micron were launched at ~3.5 m/s towards a droplet (70 mg) with a superheat

above the liquidus temperature of 100 °K. Additionally, using the same feedstock and preparation as the splat quenched sample, a molten droplet was solidified by dropping onto a stationary copper substrate to estimate the microstructure in a lower regime than those demonstrated in the three rapid solidification. The laser remelting sample was with a 110 watt power and a scanning speed of 0.55 m/s. The laser welds were done ten times to provide a statistically relevant number of samples to examine melt pool morphology and cell sizing. The three rapid solidification techniques can be seen graphically in Figure 1 alongside an estimate for cooling rate in the solidification region from literature [16].

Electron microscopy was conducted on all solidification conditions with a focus on grain size, solidification morphology, and elemental segregation. The splat quenched and laser welded samples were cross sectioned and then the samples representing each RS condition were mounted and polished down to 0.05 μm colloidal silica. The samples were etched using Krolls reagent to reveal the cellular structure and imaged using a JEOL 7000. Electron back scatter diffraction (EBSD) was conducted on the etched samples to see orientation and grain structure of the solidified material. The EBSD patterns were collected with an Oxford HKLNordlys EBSD detector using a step size of 125 nm and processed into inverse pole figure (IPF) maps using the Oxford Tango software. The micrographs were then measured using ImageJ to provide a cell spacing size. To examine the segregation in the rapid solidification techniques, a liftout was taken from each RS sample using a Thermo Fisher Helios focused ion beam system that removed the limitation of interaction volume effecting the elemental variation picked up in the EDS data. The EDS line scans were taken with a step size of 20 nm and a spot time of 750 ms for the laser weld and splat quench and 250 ms for the powder particle using an Oxford X-Max detector at 20keV.

Various methods were employed to estimate the solidification conditions for each technique. Heat transfer simulations were conducted for the splat quenched samples and droplet sample using FLUENT with 150 points across the samples. The laser welding conditions were calculated using a 2-D Rosenthal model to solve for an estimated cooling rate as well as calculating the resulting solidification velocity and gradient [9,21]. The powder cooling rate was correlated to simulated cooling curves calculated for plasma atomization of Ti-6Al-4V powder[17]. The combination of calculated solidification conditions across the various orders of magnitude demonstrated in the current study and measured characteristic length size was used to map out a linear relationship between the two and as a basis for comparing the accuracy of the solidification models. The models were calibrated using a combination of literature and experimental data [22–24] in combination to thermodynamic properties from Thermocalc Database TCTI5 as seen in Table 1 for solute specific parameters such as the diffusional coefficient as well as the partition coefficient.

Table 4.1 Solute specific solidification parameters

Parameter		Al	V	Mo	Cr	Fe
D	m_2/s	9.42E-09	5.61E-09	3.67E-09	5.73E-09	6.88E-09
k_0	-	1.06	0.95	1.15	0.74	0.38
m_0	°K/wt%	0.87	-6.98	9.52	-7.33	-9.86

The equilibrium partition coefficient values (k_0) were taken from work on beta stable titanium alloys by Mitchell et al. examining the segregation in zone cast titanium alloys [25]. Table 4.2 contains alloy parameters used in the solidification modeling from literature and Thermocalc titanium database [24,26,27].

Table 4.2 Alloy material parameters

Variable	Value	Units
Latent heat, L_f	380	J/g
Gibbs-Thomson coefficient, Γ	7.8×10^{-8}	m °K
Interfacial width, δ	1	nm
Interface kinetic coefficient, μ	0.74	m/(s °K)
Solute Segregation coefficient, A	10	
Substrate initial temperature, T_0	308	°K
Thermal conductivity, $k_t(T_L)$	30	W/mk
Thermal Diffusivity, $\alpha(T_L)$	10.2×10^{6}	m^2/s
Absorptivity, C	0.48	
Nucleation density, N_0	1×10^{17}	sites/m^3
Nucleation undercooling, ΔT_N	6.3	°K

4.3.0 Solidification Theory

4.3.1 Segregation and Diffusion

Various models attempt to characterize solute entrapment by a gradual change in the partition coefficient (k) towards unity as the solidification velocity approaches infinity as seen in Eqn. 2 [28–30]. Experimentally there is a finite velocity (V_d) that results in entrapment of the solute into the growing solid that can be estimated by changing the partition coefficient function , k(V), to unity at a dimensionless velocity value defined by $\phi = V/V_d$ [31,32]. There is a nondimensional constant, A, which effects the onset of solute entrapment and suddenness of the drop in segregation. The interfacial diffusional velocity can be estimated by Eqn. 3 [33], where D is the liquid diffusional coefficient, δ is the solid-liquid interface width assumed to be on the order of 1 nm, and k_0 is the equilibrium partition coefficient [34]. This diffusional speed at the solid-liquid interface has not been neatly captured in analytical form and is found to vary significantly in literatures with various equations ranging values around 1 m/s to higher values [34–36] thus providing an estimated region where the initiation of solute entrapment is expected

to occur[29]. The variation in diffusional speeds is due to changes in assumptions of whether the diffusional speed at the solid-liquid interface or the diffusional speed of solute in the liquid controls entrapment of solute.

$$k(V) = \begin{cases} k_0^{(1/(1+A*\frac{\phi}{1-\phi}))}; & \phi < 1 \\ 1; & \phi = 1 \end{cases} \quad (2)$$

$$V_D \approx 0.207\left(\frac{\ln(\frac{1}{k_0})}{1-k_0}\right)\frac{D_i}{\delta} \quad (3)$$

The result allows for an estimation of the partition coefficient as a function of solidification velocity. Additionally, the liquidus slope values (m) can also be modeled with the addition of solute drag term equaling 24/35 [29]. These models allow for the use of thermodynamic and kinematic values found from experiments and CALPHAD databases to model the expected solidification parameters.

$$m(V) = m_0\left[\frac{1-k(V)+(k(V)+\left(k(V)+\left(1-k(V)\right)\frac{24}{35}\right)\ln(\frac{k(V)}{k_0})}{1-k_0}\right] \quad (4)$$

To evaluate the effect that the velocity dependent values would have, the Scheil-Gulliver equation (Eqn 5) was used to evaluate the variation in composition in the solid (C_s) as a function of fraction solid (f_s). The closer to unity the partition coefficient is the primary dendrite or cellular structure will display a lower degree of segregation across it as well as removing the solute pile-up at intercellular regions needed to form intermetallics. Plotting the Scheil-Gulliver equation at different k values as estimated by Eqn 2 allowed for comparison to the expected segregation at different solidification veloicties.

$$C_s = k(V)C_0(1-f_s)^{k-1} \quad (5)$$

4.3.2 Interface Stability

The use of a marginal stability model can be used as a conservative estimate for the stability of solid-liquid interfacial features such as cells that can be related to the length of the stable linear perturbations of the planar interface. The Kurz-Giovanola-Trivedi (KGT) model [29,33,37] can be used to estimate the expected dendrite/cell tip size as a function of both the velocity and gradient (G) as seen in Eqn. 6 by predicting the feature size stable at those solidification conditions. The planar stability at a low solidification velocity (V_c) occurs due to the limited effect of constitutional undercooling as compared to the thermal gradient ahead of the solidification front and as such is a function of the gradient. The first term captures the curvature undercooling and acts a limiting factor to how small the cell size can be ($\Delta T_{curvature} \propto \Gamma/R$). The central term is representative of compositional effects such as constitutional undercooling resulting of the solute profile ahead of the S-L interface. Pe is the solutal Peclet number (Pe=RV/2D) with Iv being the Ivantsov solution for solute transport (Iv(Pe)=Pe Exp(Pe)Expint(Pe), where Expint is the exponential integral function [38,39]. The Peclet number is a ratio of diffusion time over advective time with both athe thermal and solutal effects having an associated value. In metals, the thermal peclet number is small and has been ignored in the current case but can be accounted for if needed [29]. Eqn. 6. is solved iteratively in Matlab® to solve for a value of tip radius for a given gradient and solidification velocity.

$$\frac{4\pi^2\Gamma}{R^2} + \frac{2}{R}\sum \frac{Pe_i\, m_i(V)\, c_0\, (1-k_i)\, \xi\,(Pe_i,k_i)}{1-[(1-k_i(V))Iv(Pe_i)} + G = 0 \qquad (6)$$

Furthermore, the temperature of the cellular dendritic tip and the accompanying solidus and liquidus temperature can be modeled as function of the solidification velocity as well. The solidus and liquidus temperatures (Eqn 7 and 8 respectively) are a function of the melting temperature of the pure solvent (T_m) with terms to account for the constitutional undercooling and attachment undercooling. The attachment undercooling is the ratio of velocity to interface

kinetic coefficient (μ) and therefore is only relevant at high solidification velocities such as in rapid solidification [24].

$$T_s(V) = T_M + \sum \frac{m^i(V)c_0^i}{k^i(V)} - \frac{V}{\mu} \qquad (7)$$

$$T_l(V) = T_M + \sum m^i(V)c_0^i - \frac{V}{\mu} \qquad (8)$$

The cellular tip temperature (Eqn. 9) is based on a similar principal but accounts for the solute profile in the melt ahead of the dendritic tip by the addition of the Ivantsov solution as well as adding an additional term for the curvature undercooling.

$$T_{tip} = T_M + \sum \frac{m^i(V)c_0^i}{1-(1-k^i(V)Iv(Pe^i)} - \frac{2\Gamma}{R} - \frac{V}{\mu} \qquad (9)$$

The result is that as the velocity increases the solidus and liquidus trend towards the same value as the solute is retained in the solid phase. The dendritic tip temperature is more complicated but trends toward an intermediate temperature before converging with the solidus temperature as the partition coefficients approach unity and the tip radius approaches infinity.

4.3.3 Grain Nucleation

The formation of a columnar or equiaxed microstructure during solidification is a function of the thermal gradient present during solidification as well as material properties such as the undercooling needed to nucleate new grains in front of the solid-liquid interface. The most widely used model was developed by Hunt [40] and correlates the thermal gradient to the constitutional undercooling and nucleation undercooling. The Hunt model has been used previously for rapid solidification conditions by previously for understanding the conditions to control the grain morphology[41–43].The Hunt model is two equations based on equiaxed grain fraction (ϕ_e) with the condition needed for fully columnar (ϕ_e=0.0066) or fully equiaxed (ϕ_e=0.66) acting as the controlling terms for what microstructure dominants. The gradient needed

to form each is then related to a function that depends on the nucleation site density (N_0), undercooling to heterogenous nucleation temperature (ΔT_N), and undercooling ahead of columnar growth front (ΔT_c).

$$G_{equiaxed} < 0.617 N_0^{\frac{1}{3}} \left(1 - \frac{(\Delta T_N)^3}{(\Delta T_c)^3}\right) \Delta T_c \quad (10)$$

$$G_{columnar} < 0.617\ (100 N_0)^{\frac{1}{3}} \left(1 - \frac{(\Delta T_N)^3}{(\Delta T_c)^3}\right) \Delta T_c \quad (11)$$

$$\Delta T_c = \sum m(v)_i k(v)_i \Delta C_i \quad (12)$$

$$\Delta C_i = C_0^i \left(1 - \frac{1}{1-(1-k_i(V))*Iv(Pe^i)}\right) \quad (13)$$

4.3.4 Thermal profile and melt pool characteristics

The Rosenthal model was used to model the steady-state temperature field of a moving heat source to provide an understanding of the thermal profile developed during laser welding [21,43–45]. This model has several assumptions that limit the accuracy of the predictions such as not incorporating latent heat during solidification as well as assuming a point heat source and a hemispherical melt pool morphology. However, the Rosenthal model has been used extensively in the field of laser welding as the accuracy of model away from the heat source has been found to have a strong agreement with experimental work [21,43,45]. There are however issues with relying on a analytical model with numerical solutions able to capture the conditions more accurately [46]. The 2-D model is described as follow:

$$T = T_0 + \frac{cP}{2R\pi k_t} \exp\left(\frac{-v(R-x)}{2\alpha}\right) \quad (14)$$

where the velocity of the laser (v) is in the x direction and the radial distance away from the heat source calculated by $R=\sqrt{x^2 + z^2}$. The laser powder (P) then produces a thermal field in the material that can be calculated in Matlab®. The thermal gradient can subsequently be solved for

in the x and z direction allowing for the calculation of an average gradient ($G_{avg} = \sqrt{(G_x^2 + G_z^2)}$) [21]. The solidification velocity is then assumed to be in the opposite direction of the thermal gradient (visualized as black arrows in Figure 4.1) therefore and can be estimated by the geometric relationship between gradient and laser velocity.

$$V = vcos\left(tan^{-1}\left(\frac{G_z}{G_x}\right)\right) \qquad (15)$$

The results of Eqn. 14 and 15 then give an estimate of the thermal and solidification parameters for a steady state weld.

4.4.0 Results

The Ti-5553 etched samples for powder, splat quenched, and laser welded demonstrate the fundamental differences in solidification structure in the same alloy from variation in solidification conditions. The as-atomized powder demonstrates a cellular dendritic structure when etched but is not forming a dendritic structure with secondary dendritic arms. The splat quenched samples exhibit a range of solidification structure with both columnar and equiaxed grains regions through its cross section. The centerline in the thickest regions of the splat quenched samples demonstrated cellular-dendritic structure, while the equiaxed grains structure near the copper platens were not seen to have cells present after etching. The laser welded sample demonstrates cells through the entire weld that have grown from the unmelted titanium substrate. However, the edge of the weld pool demonstrates planar solidification likely due to the high thermal gradient and low solidification velocity at this location of the weld. The arc melted substrate has grains that are on the order of 250 μm and so the laser weld is seen to be solidifying effectively from a single crystal substrate. The laser welded sample also demonstrates rotation of the cells from perpendicular to the weld line to aligned with the direction of laser scan direction as expected from Eqn. 15.

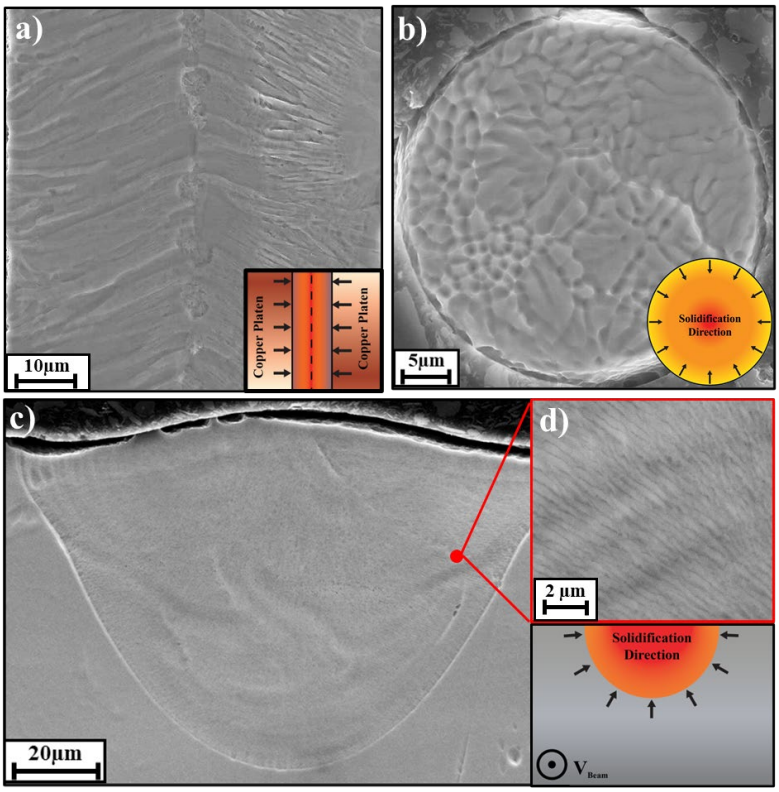

Figure 4.2 Etched images of (a) splat quenched foil, (b) plasma atomized powder, (c) laser weld with inset of cell structure, and (d) cellular structure of droplet.

Examination of the grain structure through EBSD reveals that the material displays fundamental differences in grain structure between the different solidifcation conditions. The powder demonstrates grains an order of magnitude larger than the cellular structure seen in the etched images potentially meaning the post-solidifcation cooling rate in plasma atomized powders is low enough for grian growth to occur or that the there is very low inoculants in the powder limiting the nucleation [47]. The splat quenched foil demonstrates a mixture of columnar and equiaxed grains that was seen in the etched images but with a clearer view that the near surface grains are all equiaxed with the amount of columnar growth increasing towards the midline of the sample. The laser welded sample is seen to grow off of the unmelted material

below therfore retaining the orientation of the base material resulting in columnar grain growth. There is an increase in the misorientation in top-central region of the laser weld that is due to the different regions of the melt pool meeting with slight variation in orientation. These observations are similar to their solidification morphology with the laser weld and powder largely containing very few grians with clear solidifcation structrues within. The EBSD of the splat quench sample does clarify that the columnar strutcures present on the order of ~1µm are grains that have much smaller,

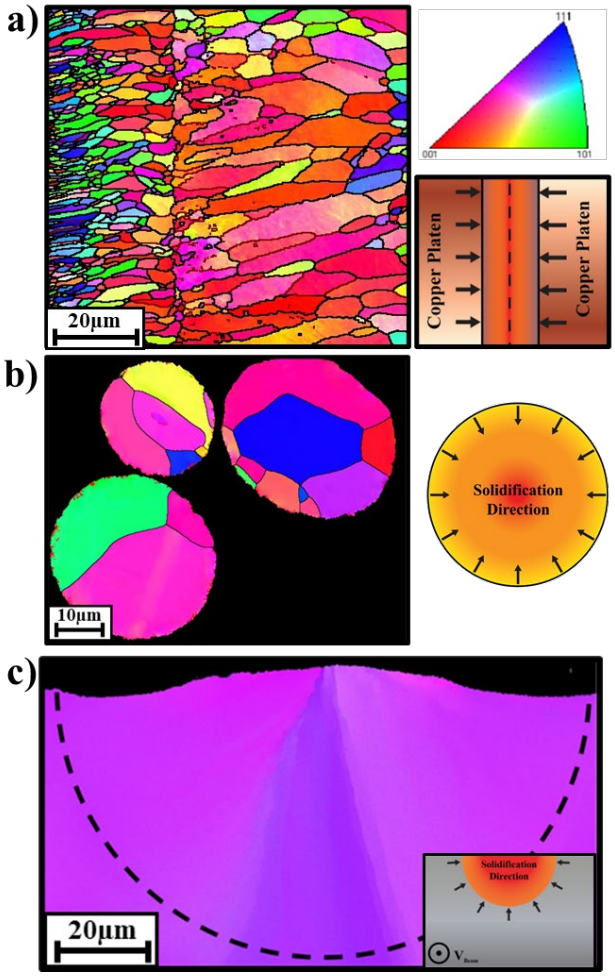

Figure 4.3 Inverse pole figure (IPF) maps of the BCC titanium oriented in the vertical direction of each image in the three rapidly solidified conditions demonstrating the drastic difference in crystallite structure.

The Fluent simulations of the splat quenching process demonstrate the significant variance in the cooling rate that develops in the splat quenched foils (Figure 4.4) [48]. The changes in cooling condition have marked effects on the microstructure with the higher cooling rate seen at the edge of the splat demonstrating a columnar grain morphology without signs of cellular dendritic structure as seen in the inset image in Figure 4.4. The central region has a lower overall cooling rate and resultingly demonstrates cellular dendritic structure near the midline of the splat. Additionally, the lower cooling rate has an associated effect of reducing the solidification velocity and gradient resulting in the presence of both equiaxed and columnar grains while the edges demonstrated only columnar grain structure. The change in heat transfer coefficient was found to occur due to the difference between contact with the copper platens that occurs between the center of the splat that is formed by the molten sphere impinging upon the platens and the edge of the splats that are formed by jetting of liquid material during the final collision of the platens. The jetting material has a low contact pressure with the platens until the platens collide resulting. The result means that the material cooling rate is controlled by the pressure of the platen collision while the thicker central portion of the sample has a significant portion of the cooling occurring prior to collision. The decreased thickness and increased heat transfer coefficient lead to an overall higher cooling rate that promotes planar solidification in the edge of the sample.

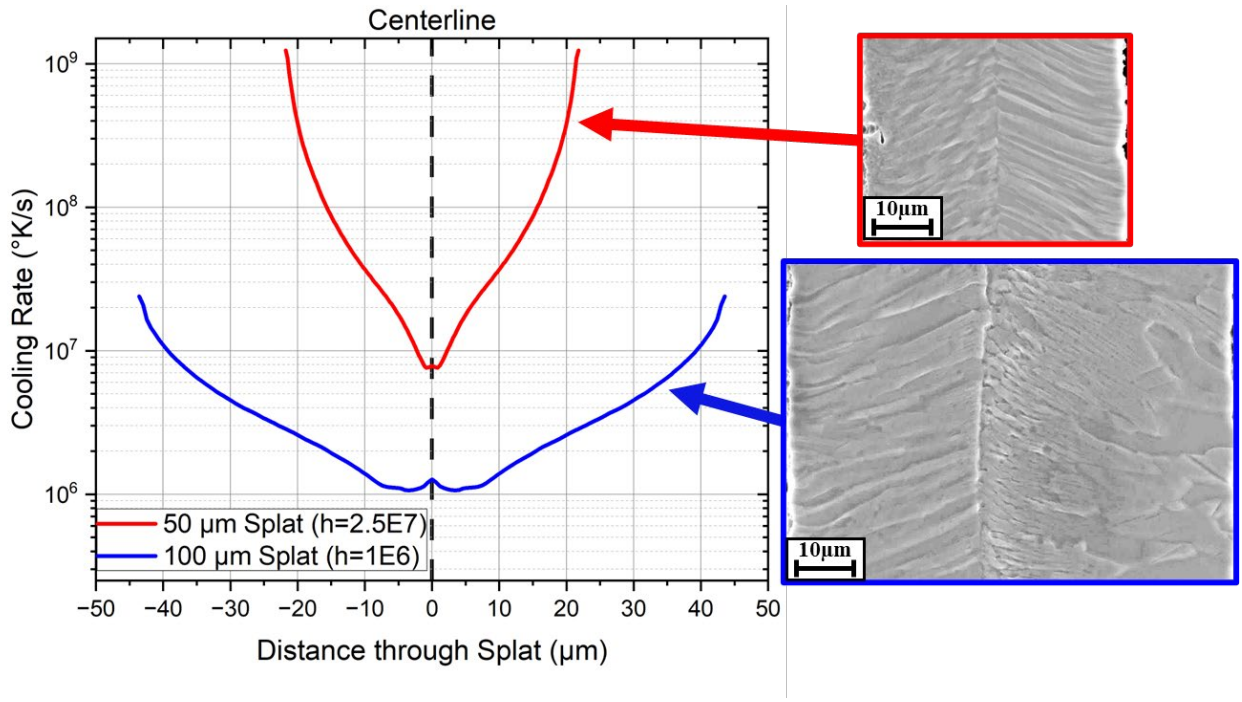

Figure 4.4 Simulated cooling rates at two representative radial position in a splat quenched samples from the center (thickness=100 µm) and edge (thickness=50 µm). SEM micrographs of etched representative microstructures are highlighted with arrows. The 100µm thick central region of a Ti-5553 splat displayed cells, while the thinner region found at the edge did not due to the decreased thickness and increased heat transfer coefficient ($W/m^{2}°K$) resulting in an increased cooling rate.

The use of a 2-D Rosenthal steady-state model reveals that the cooling rate observed for the laser welded samples is on the order of 2-5 10^{6} °C/s at the edge of the melt pool. The Rosenthal model is plotted in Figure 5a demonstrating the steady-state thermal profile around the heat source. A significant region of the melt pool is well in excess of the melting point due in part both to the physical heat transfer of the laser remelting but also due to the limitations of relying on a point source in the analytical model. The Rosenthal model has other limitations such as lack of phase transformation or introduction of a latent heat term that limit the useful of

the model to accurately predict the conditions at the solid liquid interface. The estimated cooling rate and solidification velocity as a function of depth are plotted in Figure 5b, where the cooling rate is actually fairly consistent throughout most of the molten pool while the solidification velocity increases quite significantly throughout the depth reaching the laser raster speed near the top of the weld. In particular examination of 25 µm and 50 µm below the surface of the weld were done to understand the variation occurring throughout the solidification event. The solidification velocity for the two regions did vary significantly with 25 and 50 µm demonstrating 0.33 and 0.15 m/s respectively. The average thermal gradient decreased as the surface was approached with the varying from 15.5-7.1*10^6 °K/m between the 50-25 µm depths. However, the associated cooling rate was nearly identical between the two locations though with the 25 µm position having a 4% increase in cooling rate.

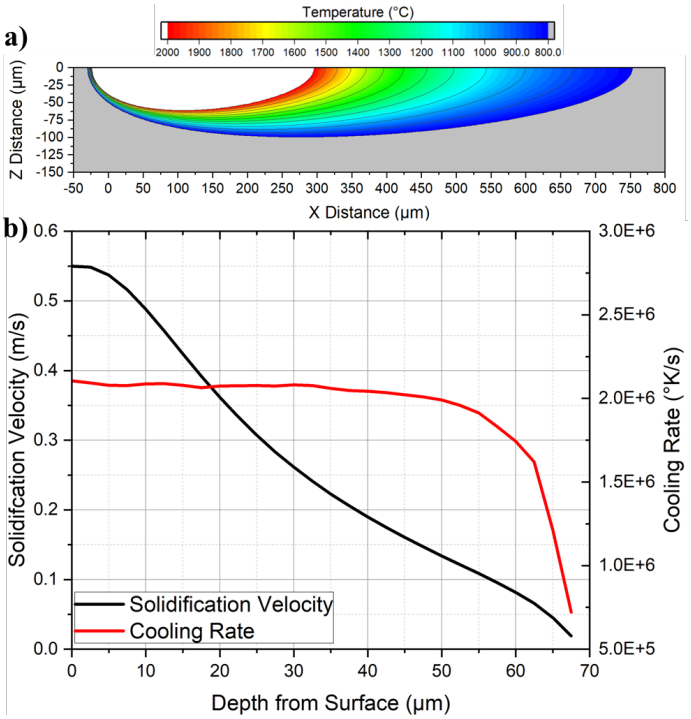

Figure 4.5 (a) 2-D Rosenthal solution for Ti-5553 weld (P=110W V=0.55 m/s) with (b) the calculated solidification velocity and cooling rate calculated from within the solidification

interval plotted from the surface down to the root. The direction of melt pool travel is from right to left.

Plotting of the partition coefficient and liquidus slope demonstrates the retention of solute as a function of velocity. As the velocity increases the partition coefficient of the various solute trends towards unity meaning a reduction in the overall segregation in the solidified material. Figure 6. has both the functions for the local equilibrium model based upon the continuous growth model developed by Aziz et al. [28] and hyperbolic local nonequilibrium model [32] to demonstrate the difference that occurs in the partition coefficient due to differences in solidification assumptions. A table of the k values as a function of velocity from the local nonequilibrium model can be seen in Table 4.3. Examination of the partition coefficients (literature values) in either model demonstrates that the vanadium, molybdenum, and aluminum have limited segregation in this alloy. As such, the chromium and iron are the most heavily segregatory as expected. Of interest is that the elements are predicted to reach the limits of their ability to diffuse at the S/L interface at different solidification velocities with molybdenum being the first to reach a diffusionless state. Additionally, the slope of the liquidus curve (Thermocalc), Figure 6b, has also been plotted as a function of velocity demonstrating that iron and chromium become more potent at undercooling as velocity increases while the other three solute additions have limited change in liquidus slope in addition to a low partition coefficient. The change of the m value can be seen largely to effect molybdenum, chromium, and iron with iron becoming

increasingly more potent as the solute is retained in the matrix at high solidification velocities.

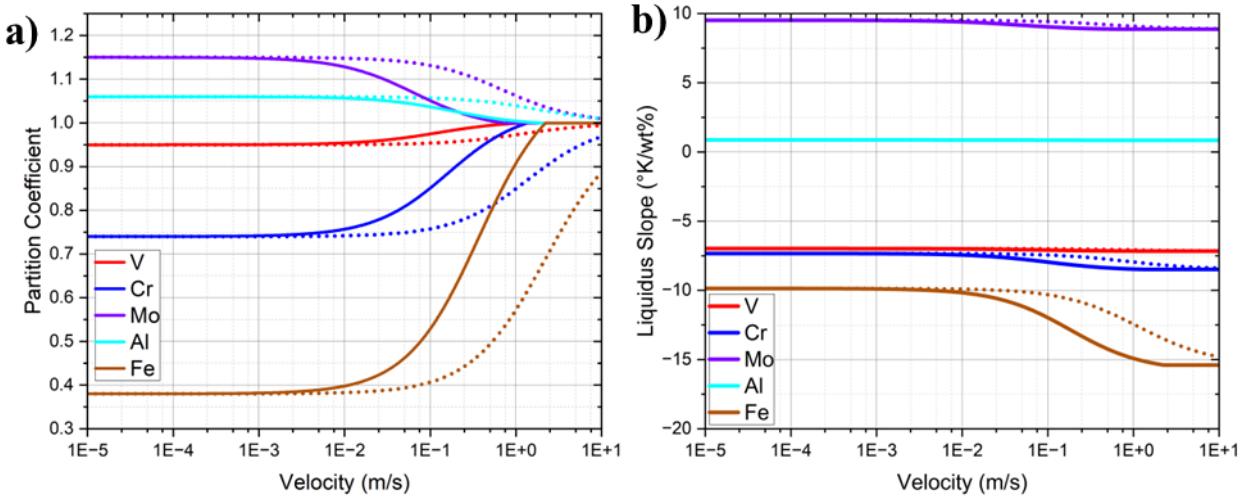

Figure 4.6 Plots of (a) partition coefficient and (b) liquidus slope as a function of solidification velocity for each of the solute addition with the local equilibrium approach (dotted lines) and the hyperbolic local nonequilibrium approach (solid lines).

Table 4.3 Hyperbolic partition coefficients as a function of solidification velocity

	Partition Coefficient (Hyperbolic Diffusion)				
Solidification Velocity	**Al**	**V**	**Mo**	**Cr**	**Fe**
1 µm/s	1.060	0.950	1.150	0.740	0.380
0.01 m/s	1.057	0.954	1.128	0.757	0.398
0.1 m/s	1.037	0.975	1.051	0.851	0.529
0.25 m/s	1.022	0.987	1.020	0.916	0.667
0.5 m/s	1.012	0.994	1.005	0.960	0.795
0.75 m/s	1.007	0.997	1.000	0.979	0.863
1.0 m/s	1.004	0.999	1.000	0.990	0.908
2.5 m/s	1.000	1.000	1.000	1.000	1.000

Furthermore, the marginal stability limit reveals the impact of solidification velocity on the expected radius of the cellular-dendritic structure. There is a breakdown at both the high velocity region due to localization of the solute diffusion as well as at the low velocity regions due to the high thermal gradients expected during rapid solidification techniques as seen in

Figure 4.7a and b. Figure 4.7b also has the calculated velocity limit of diffusion for chromium and molybdenum (V_d) to highlight the expected velocities in comparison to these values. The expected liquidus and solidus can also be seen to change at the high solidification range as solute entrapment begins to take effect. As the velocity increases the reduction in segregation result in the solidus and liquidus temperatures trending towards each other where diffusionless solidification would occur. Also calculated is the temperature at tip of the dendrite demonstrating that there is a change in the temperature as a function of velocity due to increased undercooling associated with curvature and buildup of solute at the interface prior to the initiation of solute entrapment. The increase in cell size and entrapment of solute are both a result of entering the rapid solidification regime and result in an increase dendritic tip temperature. There is also a breakdown in tip temperatures at low velocities to the solidus temperature due to the revision back to planar stability with the limit relating to the gradient developed in the material. While a gradient of 0 °K/m is unachievable, the thermal gradient in many applications is orders of magnitude lower than the 10^7 °K/m expected in laser welding. Therefore G=0 °K/m is used an equilibrium value with processes breaking down somewhere along the length of the curve depending on there associated thermal gradient. The plotting of the expected liquidus and solidus for the alloy can be used to predict the onset of planar solidification at the intersection of the two values.

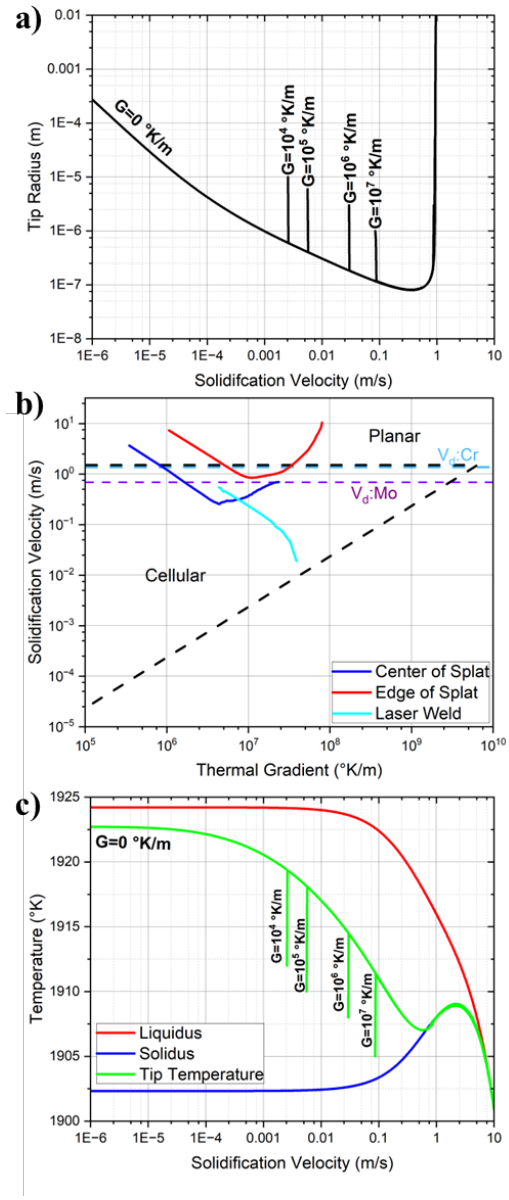

Figure 4.7 (a) KGT marginal stability for Ti-5553 demonstrating the limit of expected solid-liquid perturbation stability occurring on the order of 1 m/s with (b) the simulated solidification history of the splat quenched, and laser welded sample overlayed unto the expected cellular to planar transition map with horizontal lines at the predicted limit of diffusion for the molybdenum and chromium solutes. (c) Plot of the effect of solidification velocity on tip temperature as well as the solidus and liquidus temperature.

The solidification condition of the powder is more complicated than the other solidification conditions due to the deep undercooling that can occur due to the lack of a solid substrate. The cooling rate of plasma atomized powder is generally reported as on the order of 100-1000 °C/s but work by Birt et al. modeled the cooling rate seen by various powder sizes during plasma atomization. The convective heat transport dominates during the initial solidification process with the cooling decreasing rapidly with time as the velocities of the powder decreases [17]. The powder then resultingly demonstrates a unique microstructure as the segregation and cell boundaries are formed from the rapid solidification that is achieved from the combination of undercooling of the droplet needed to nucleate the solid phase and the high level of convective heat transfer. However, the grain size is subjected to grain growth due to being held at an elevated temperature as the cooling rate drops. The result is grains, Figure 3b, that are not correlated to the equiaxed cell structure seen from the etching. With the average cell size being measured as 2.0-2.2 μm for 30-40 μm powder a the KGT model points to a solidification velocity of ~1.0 10^{-3} m/s. Comparing this solidification velocity to those found during undercooling experiments in titanium by Walder et al. [39] the total undercooling required to reach this solidification velocity is 6.3 °K, Figure 8. As the undercoolings were only found to deviate from a power law fit at undercoolings above 100°C the power law fit was used to estimate the undercooling experienced by the powder. The undercooling is in good agreement for values on the order of 5°K that been used previously to model equiaxed grain nucleation in titanium AM simulations [14,49]. These estimations are only accurate for near the surface of the powder as the gradient and velocity will drop significantly once growth begins into the powder interior.

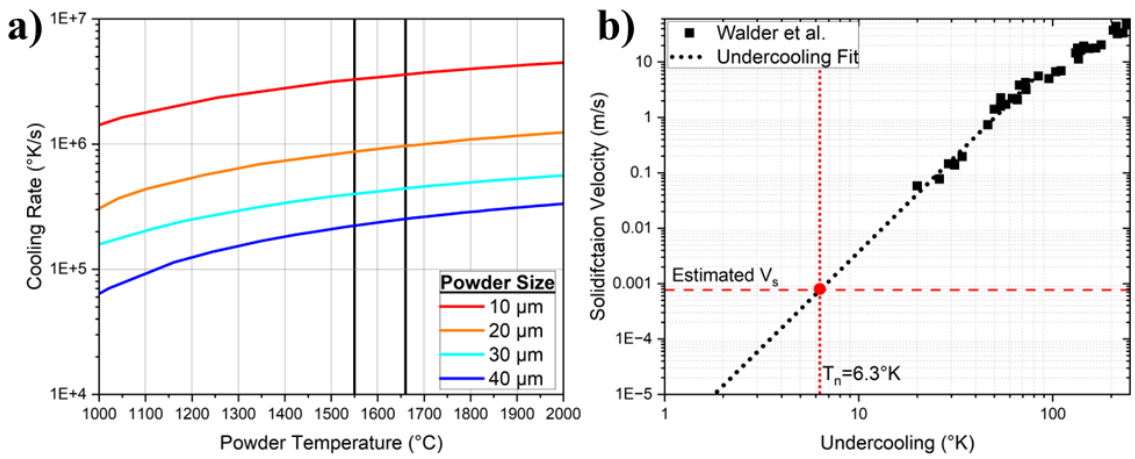

Figure 4.8 (a) Cooling rates modeled for titanium powder produced by plasma atomization at the solidification interval for Ti-5553 [17]. (b) Titanium undercooling data corelated to solidification velocity that predicts that an undercooling of 6.3°K is needed to produce the solidification predicted for the Ti-5553 powder [39].

Plotting of the Gulliver-Scheil equation demonstrates the significant differences in undercooling, segregation, and morphology of the material as it solidifies. Figure 9a is the expected chromium segregation changes from the near equilibrium values predicted at a solidification velocity of 10 µm/s as compared to higher values in the range of 0.1-1.0 m/s. Above a solidification velocity of 0.5 m/s, the chromium is expected to fluctuate less than 0.5 wt% meaning that in the laser weld and splat quench sample the segregation will be much smaller than equilibrium. Figure 9b highlights just two solidification velocities at 1 µm/s and 0.5 m/s for the main three beta stabilizers in the alloys, namely chromium, molybdenum, and vanadium. At 0.5 m/s the molybdenum and vanadium segregation are limited to less than 0.25 wt% change at the interdendritic region and further decreases as the velocities increase to splat quenching or laser welding velocities. The result of these changes is less segregation at the cells

and a smaller solute gradient in the solidification structure resulting in a higher uniformity in the chemical composition and solidification structure.

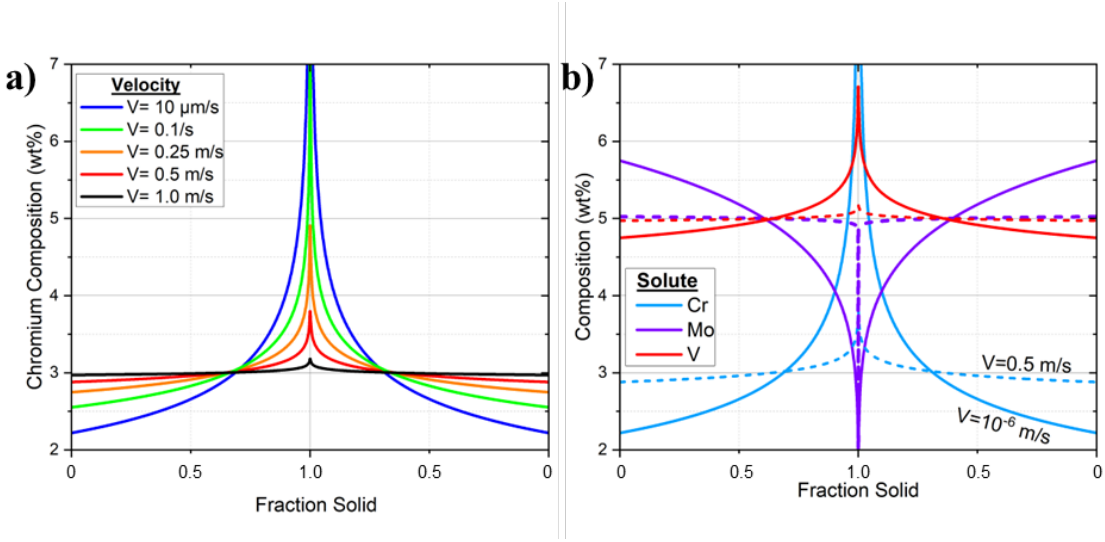

Figure 4.9 Scheil plots demonstrating the change in segregation behavior across the fraction of solid for various velocities. (a) Comparison of just the expected chromium segregation for numerous solidification velocities. (b) The beta stabilizing solutes as compared between a near equilibrium solidification (1 µm/s) and at 0.5 m/s.

EDS line scans across fib liftout demonstrates the significant reduction in segregation that occurs as the solidification velocity is increased. The segregation of molybdenum and chrome can be easily distinguished in the 45 µm powder particle due to the low solidification velocity estimated to be on the order of $5x10^{-4}$ m/s. That solidification velocity aligns with what near equilibrium values for this system. The slowest solidifying regions of the splat quench have a solidification velocity near 0.25 m/s and the EDS demonstrates fluctuations of chromium, but magnitude of fluctuation is greatly reduced. The laser welded sample at 0.55 m/s did not demonstrate enough fluctuation in the composition to result in an easily detectable change.

Therefore, the segregation has decreased significantly in the region of 0.25-0.55 m/s that can be appreciable be correlated to the trend toward unity of the partition coefficient at these velocities.

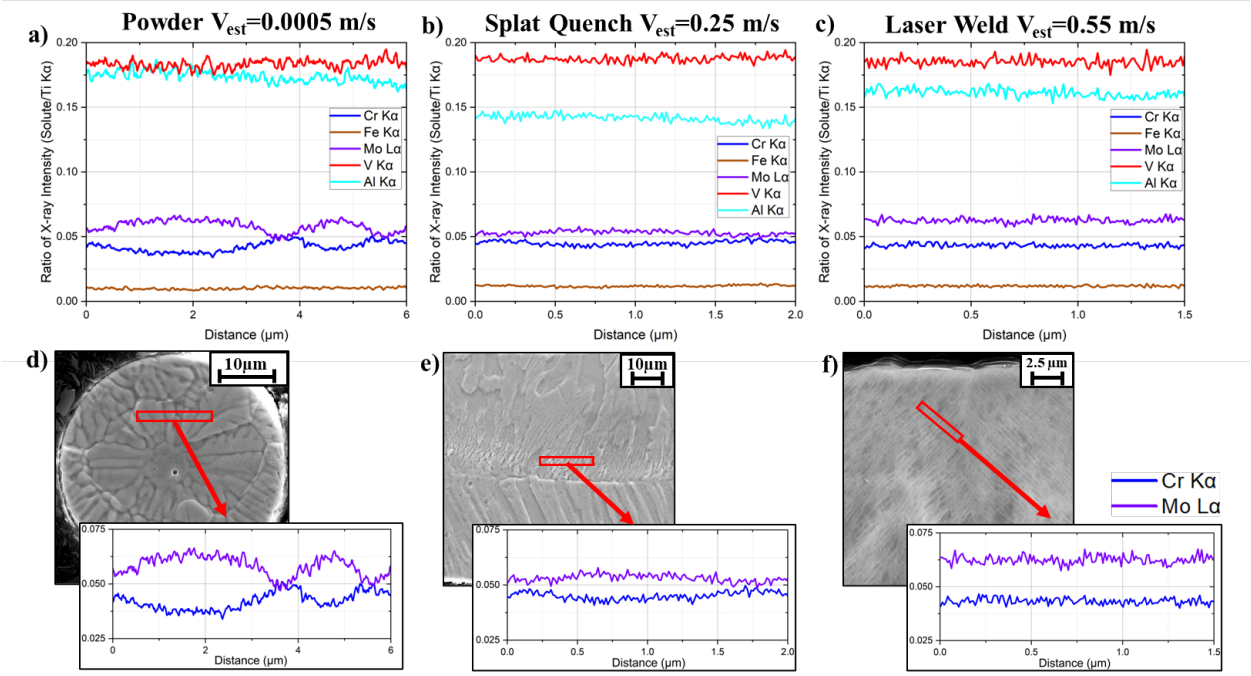

Figure 4.10 Energy dispersive spectroscopy line scan data from (a) center of 50 μm powder, (b) midline of 100μm splat quenched sample, and (c) top of 0.55 m/s laser welded sample demonstrating the decrease in segregation as a function of solidification velocity. The ordinate is the counts of the solute divided by the Ti Kα counts of the matrix to normalize by specimen thickness. In addition to (d-f) SEM images of nominal TKD sample lift out position with highlighted EDS curves for the Mo and Cr lines across the cells highlighting the difference in the three RS conditions.

With the ability to now probe a significant area of the solidification space in terms of solidification velocity and thermal gradient, the columnar to equiaxed transition for this alloy can be mapped, Figure 11a. The use of the Hunt's model [40] allowed for capturing both the gradient where the columnar grains began to stabilize as well as the velocity where only equiaxed grains were achieved. The overlap of splat quenched material, substrate cooled droplet, and laser weld

provide key fitting parameters with the general shape outlined by Eqn. 10 and 11. The fitting parameters are outlined in Table 2 demonstrating that there is a higher than typical nucleation undercooling as compared to other more studied alloys such as 0.75 °K used for Al-Cu in Hunt's original work [40]. Additionally, the transition found for effect of gradient on the material is a result of the nucleation density that was fitted to a value of 10^{17} sites per meter cubed that was found from the smallest grain size found in the splat quenched samples of 3 µm. Of interest is that due to the retention of solute at solidification velocities near unity, the constitutional undercooling reduces, and columnar grains are predicted to dominant at higher solidification velocities. This can be seen in the 50 µm splat quench samples seen to only have columnar grains.

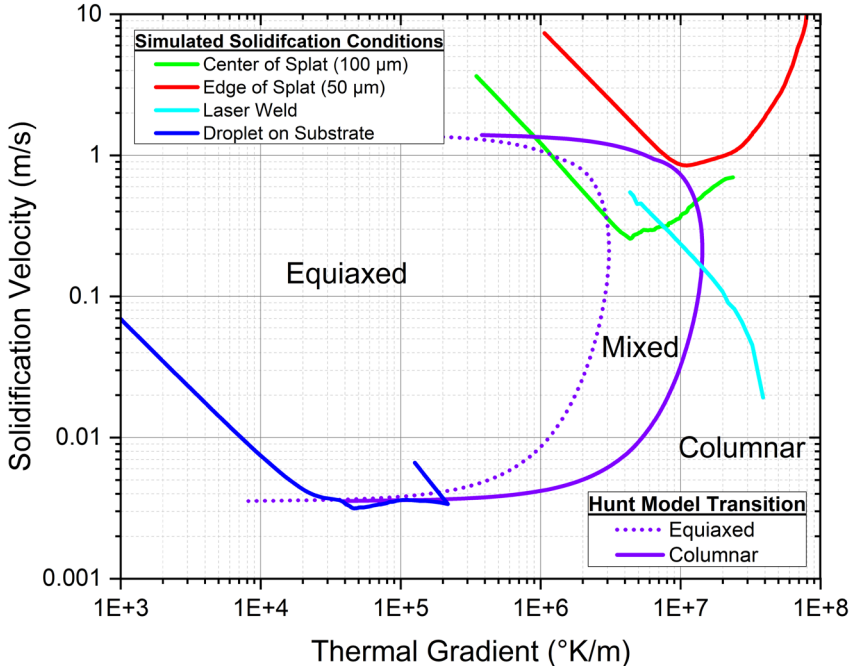

Figure 4.11 (a) Map of thermal gradient versus solidification velocity across splat quenching, single laser track remelting, and molten droplet. The plotted columnar to equiaxed transitions (Eqn 10-13) are plotted onto the map to demonstrate the change in solidification structure from columnar to equiaxed throughout the various solidification processes.

4.5.0 Discussion

The metastable beta titanium alloy Ti-5553 was explored using rapid solidification techniques and analytical models to characterize the solidification behavior and segregation as the solidification velocity beyond the limits of the solid-liquid interfacial equilibrium. The bulk of analysis for titanium alloys are focused on Ti-6Al-4V that demonstrates limited segregation as both vanadium and aluminum demonstrate k values on the order of unity. The use of chromium and iron is generally limited in typical titanium alloys due to the higher segregation potential leading to the formation of intermetallics that are difficult to dissolve back into solution and negatively affect mechanical performance. To provide further exploration into the ability to retain these beta stabilizers, the effect of velocity on the expected partition coefficient was analyzed. Special attention was paid to understanding when the transition to planar solidification would occur and how the different solutes differ in their response. Beyond that predictions were made to the tip radius and columnar to equiaxed transition (CET) to provide description of the microstructures expected to develop during RS processing.

The use of varying solidification techniques allowed for exploration of a wider range of solidification conditions and variance between gradient and solidification velocity. The growth from the unmelted substrate in the laser welded sample is established early in solidification due to the low undercooling for growth of the solid-liquid interface from the unmelted titanium as well as the estimated high undercooling estimated for nucleation of grains in the melt. The other solidification techniques do not have this ease of isomorphous growth an unmelted substrate due to either relying on undercooling to initiate solidification (atomization) or cooling on an dissimilar metal in splat quenching. Therefore, the atomization and splat quenched samples are expected to have higher undercoolings in the melt to nucleate grain growth that promotes the

growth of equiaxed grains since there was not found to be any strong inoculants in the titanium alloy. Additionally, the relationship between the velocity and gradient are different as seen graphically in Figure 1, where in the laser welded sample the two parameters are inversely connected while in the splat quenched samples both decrease as the material solidifies. The G and V were simulated then correlated to the KGT stability model to look at the quality of the model to predict cell sizes. The smallest measured cell radius in the splat quenched samples was 0.11±0.03 μm that puts this size in near the projected minimum tip radius of 0.08 μm estimated using Eqn. 6. This minimum tip radius is estimated to occur at a solidification velocity of ~0.87 m/s. The projected velocity for diffusionless solidification using KGT has been found previously in AM applications to be an conservative estimate with the inflection point of the solidus line ($dT_s/dV = 0$) being found to be a better estimate for the transition to diffusionless solidification [34]. The maximum of the solidus temperature occurred at 2.29 m/s when considering complete solute entrapment at values above the diffusional limit while when using the local equilibrium model a velocity of 2.19 m/s can be reached before planar solidification though the partition coefficient drops to near unity in the proximity of 1.0 m/s. In the case of Ti-5553, what was found is that the solute segregation with multiple additions complicates the matter as the diffusional limit of elements such as molybdenum (0.71 m/s) are well below the limits of other solutes such as iron (2.22 m/s) and chromium (1.37 m/s). The individual solutes are limited by their own diffusional interaction with the solid-liquid interface meaning that at increasing solidification it should be seen that segregation of the slower elements should eliminated while the higher diffusion elements are still able to segregate [35]. The conclusion from these estimates is that though the definitive limit for fully planar solidification to occur can vary based on what

metric is used to estimate the value, solidification velocities over the region 1-2.5 m/s are expected to demonstrate planar solidification.

Examining the segregation through energy dispersive spectroscopy (EDS) clearly revealed the solute segregation decreased when the solidification velocity increased. Using the Gulliver-Scheil model with the velocity dependent partition coefficient and liquidus slope reveals that on the order of 0.50 m/s there is a drastic decrease in the segregation profile for all solute resulting in the difficulty perceiving elemental partitioning with EDS. This leads to the belief that the solidification conditions seen in laser based AM processes are able to incorporate significantly higher solute additions as compared to casting and slower AM processes such as DED [50]. The drop in partitioning is seen to happen close to the diffusional limit of a solute meaning that the solidification velocity seen in the laser weld and splat quenched sample on the order of 0.1-1.0 m/s results in higher retention of solute retained in the matrix but an order of magnitude decrease to 0.01 m/s or slower would lead to segregation closer to what is seen during casting. This drop can clearly be seen in the comparison between the elemental segregation of the powder as compared to the two rapid solidification conditions.

The solidification structure predicted by the marginal stability model is useful in understanding the solidification structure especially at low solidification velocities but has significant areas of weakness due to the variance that can occur in partition coefficient and diffusional limits of solute. The concept of interfacial stability in solidification is inherently a complex problem due to the numerous sources of undercooling and the nature of diffusion, anisotropy in attachment mechanics, and nucleation that are all dependent on the local composition of the melt. As such, models inherently have assumptions such as the definition of diffusional velocity or lack of solute interactions allowing for significant variation of the stability

of cell size at high velocities. The variation decreases the confidence of predicting an absolute limit for planar solidification but provides a transition region for informing the degree of segregation and if planar solidification could potentially form. The microstructure also demonstrates a lack of sensitivity to significant variations of solidification velocity such as the smallest cells measures only formed after planar solidification in the splat quenched samples but the increasing velocity of the laser welding not demonstrating a similar change in size as a function of velocity change throughout the weld depth. This has been seen before in modeling of the solidification structure in laser welded samples where the predicted structure should turn into planar solidification but retains a similar cell size [9,34]. This can be either to inherent problems in the model or the stability of planar growth with limited driving force to form that has been found to result in banding or in this case a lack of driving force for elimination of the existing cell structure at velocities near the theoretical limit of cellular growth [51]. In regard to solute interactions, while this alloy is not an ideal dilute-binary this system does not have significant activity in any solute (maximum activity for a solute at $T_{solidus}$ was 0.0014 for chromium) to believe there is enough solute cross interaction to display fundamental differences in how individual solute atoms diffuse as compared to their binary counterparts.

To stand as a comparison to the rapidly solidified material, a droplet of Ti-5553 cooling on a flat copper substrate that demonstrated a dendritic structure. In comparison to even the powder, the solidification structure in the droplet is dendritic with secondary dendrite formation between the primary dendritic cores. Even the secondary dendrite arm spacing (SDAS) has a spacing significantly larger than the RS processed materials. Across the height of the droplet the SDAS ranges from 7.5-12.0 μm in comparison to the splat quench sample that demonstrated largely submicron cell sizes. The dendritic microstructure also results in porosity and beta fleck

formation (Ti-(Cr,Fe) intermetallic formation) in the interdendritic region as the slow solidification velocity allows ample time for diffusion at the solid-liquid interface to occur. the change in structure is drastic, which can be explained by the difference in cooling rate being over three orders of magnitude in difference when simulated. So, the transition in solidification structure occurs over order of magnitude variation with the cooling rate of the powder at 10^5 °K/s still being high enough to eliminate secondary dendrite arm formation. The simulated solidification conditions for the droplet can be seen in Figure 4.11.

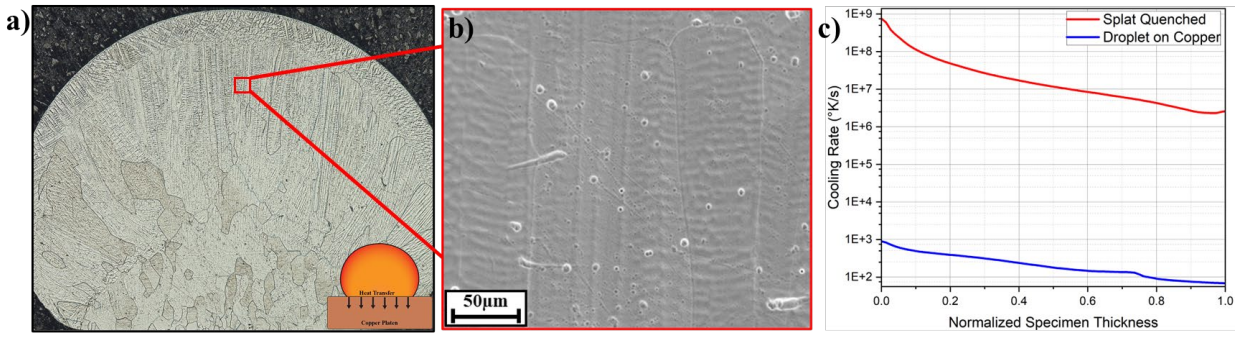

Figure 4.12 Droplet of Ti-5553 on copper substrate (a) optical image, (b) SEM image of dendritic structure, and (c) cooling rate simulation compared to the splat quenching process (thickness=2000 µm, h=10^3 W/m^2°K).

The characteristic length (λ) can be plotted across a range of cooling rates allowing a tool to offer an empirical tool to understand the cooling and solidification conditions of a processing route. can be plotted to allow for estimation and understanding of the solidification structure as a function of the processing parameters. Figure 13a displays the measured cellular-dendritic size as a function of the calculated cooling rate with a power law fit of $\lambda=454CR^{-0.453}$ that provided an R^2 value of 0.945. The error in fitting is due to the inherent difficulty using cooling rate to predict cell spacing as well as the limited values of cell spacing from lower solidification velocities and cooling rates measured in this study. Furthermore, Figure 13b has the cell radius

from the KGT model plotted with experimental cell spacing overlayed demonstrating the capturing of the overall trend of the solid liquid face stability. The solidification veloicty and thermal gradient were calculated from either analytical models or numerical simulations Furthermore, Both of these models have areas of concern as the rapid solidification response of any material is difficult to model accurately and succinctly but provide a guide for further solidification research.

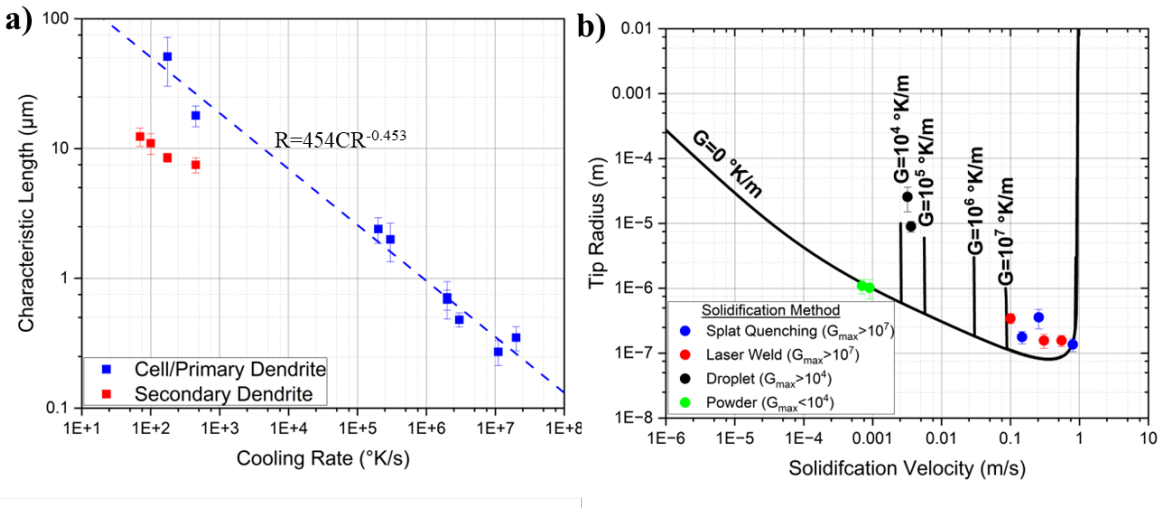

Figure 4.13 (a) Correlation between the cells sizes measured correlated to the calculated cooling rates in both the dendritic region, seen in the substrate cooled droplet, and the cellular region, laser welding, powder, splat quenching. (b) The same cellular-dendritic sizes correlated to the KGT interfacial stability model.

The solidification condition across several rapid solidification have been examined in the current study to present a wide ranging view of rapid solidification for the beta stabilized titanium alloy system. Each process possesses a unique solidification profile that relate to the mode of heat transfer mechanism used either through convection to a gas, conduction through a

platen, or conduction through an unmelted bulk substrate. The differences in cooling rate, solidification velocity and solidification structure have been examined offering the ability to evaluate the drop in segregation from nearly equilibrium values seen in the solidified droplet to several regions in the splat quenched sample that were not seen to have cells when etched likely due to planar solidification. The ability to have cells that demonstrate minimal solute segregation and therefore being unable to be etched cannot be ruled out but the numerical simulation providing an estimate of solidification velocity at the edges of the splat in the region of 10 m/s does position the material above the expected region for cells to form.. The varying solidification parameters also allowed for fitting of a columnar to equiaxed grain model demonstrating that the high undercooling needed to nucleate grains ahead of the solid-liquid interface is the primary driving force for the tendency to form columnar grains during AM processing of titanium. Finally, the combination of a stability model and empirical measurements were used to map out the cell spacing as a function of projected cooling rate and solidification velocity that had not been previously done for this class of titanium alloys.

4.6.0 Conclusions

In this paper, the rapid solidification of beta titanium alloy Ti-5553 was analyzed, characterized, and modeled to describe the general solidification conditions of the alloy family. The use of splat quenched, laser welded, and plasma atomized samples of the same alloy allowed for correlation between the various processing routes and their final solidification structure.

- Comparison between EDS segregation data and analytical models reveal that the high velocities offered by laser based AM process reduce the segregation seen in the titanium

alloy even on the order of 0.1 m/s to within the noise of EDS, while slower processes such as atomization and arc based AM processes still have detectable segregation.

- The limit of planar stability at high solidification velocities was likely reached by splat quenching but did not occur during laser welding where cells could be seen throughout the weld.
- The solidification structure of the laser weld, powder, and splat quench sample allowed for the fitting of a columnar to equiaxed grain structure map that demonstrated a significant undercooling needed to nucleate equiaxed grains revealing the difficulty of eliminating columnar grain growth in titanium alloys such as Ti-5553 and Ti-64.
- The KGT marginal stability criterion was fit to the alloy system describing the cellular structure in terms of solidification velocity but limitations in the understanding of the limit of diffusion of solute species at the transition from cellular to planar solidification result in the model acting as a medium fidelity predictive tool.
- The calculated cooling rate for the various solidification techniques allowed for fitting of a cooling rate to cell size relationship of $\lambda=454CR^{-0.453}$.

References

[1] G. Lutjering, C. Williams, James, Titanium, 2nd Edition, 2nd Editio, Springer, New York, 2007. https://doi.org/https://doi.org/10.1007/978-3-540-73036-1.

[2] P. Yang, K.L. Johnson, J.D. Carroll, J.L. Buckner, M.A. Blea-Kirby, C. Groves, E.N. Coker, Thermophysical properties of additively manufactured Ti-5553 alloy, Addit. Manuf. 76 (2023) 103769. https://doi.org/10.1016/j.addma.2023.103769.

[3] D. Sharma, S.R. Kada, D. Fabijanic, D. Parfitt, B. Chen, B. Roebuck, M.E. Fitzpatrick, M.R. Barnett, The ageing response of direct laser deposited metastable β-Ti alloy, Ti–5Al–5Mo–5V–3Cr, Addit. Manuf. 48 (2021) 102384.

https://doi.org/10.1016/J.ADDMA.2021.102384.

[4] H. Schwab, M. Bönisch, L. Giebeler, T. Gustmann, J. Eckert, U. Kühn, Processing of Ti-5553 with improved mechanical properties via an in-situ heat treatment combining selective laser melting and substrate plate heating, Mater. Des. 130 (2017) 83–89. https://doi.org/10.1016/J.MATDES.2017.05.010.

[5] H. Schwab, F. Palm, U. Kühn, J. Eckert, Microstructure and mechanical properties of the near-beta titanium alloy Ti-5553 processed by selective laser melting, Mater. Des. 105 (2016) 75–80. https://doi.org/10.1016/J.MATDES.2016.04.103.

[6] C. Hicks, T. Konkova, P. Blackwell, Influence of laser power and powder feed rate on the microstructure evolution of laser metal deposited Ti-5553 on forged substrates, Mater. Charact. 170 (2020) 110675. https://doi.org/10.1016/J.MATCHAR.2020.110675.

[7] C.H. Ng, M.J. Bermingham, L. Yuan, M.S. Dargusch, Towards β-fleck defect free additively manufactured titanium alloys by promoting the columnar to equiaxed transition and grain refinement, Acta Mater. 224 (2022). https://doi.org/10.1016/j.actamat.2021.117511.

[8] D. Zhang, D. Qiu, M.A. Gibson, Y. Zheng, H.L. Fraser, A. Prasad, D.H. StJohn, M.A. Easton, Refining prior-β grains of Ti–6Al–4V alloy through yttrium addition, J. Alloys Compd. 841 (2020) 1–7. https://doi.org/10.1016/j.jallcom.2020.155733.

[9] J.D. Roehling, A. Perron, J.L. Fattebert, T. Haxhimali, G. Guss, T.T. Li, D. Bober, A.W. Stokes, A.J. Clarke, P.E.A. Turchi, M.J. Matthews, J.T. McKeown, Rapid Solidification in Bulk Ti-Nb Alloys by Single-Track Laser Melting, Jom. 70 (2018) 1589–1597. https://doi.org/10.1007/s11837-018-2920-2.

[10] C.R.M. Afonso, J.M. Chaves, O. Florêncio, Effect of Rapid Solidification on Microstructure and Elastic Modulus of β Ti–xNb–3Fe Alloys for Implant Applications, Adv. Eng. Mater. 19 (2017) 1600370. https://doi.org/10.1002/ADEM.201600370.

[11] A. Almeida, D. Gupta, C. Loable, R. Vilar, Laser-assisted synthesis of Ti-Mo alloys for biomedical applications, Mater. Sci. Eng. C. 32 (2012) 1190–1195.

https://doi.org/10.1016/j.msec.2012.03.007.

[12] C.H. Ng, M.J. Bermingham, D. Kent, M.S. Dargusch, High stability and high strength β-titanium alloys for additive manufacturing, Mater. Sci. Eng. A. 816 (2021) 141326. https://doi.org/10.1016/J.MSEA.2021.141326.

[13] C.H. Ng, M.J. Bermingham, D. Kent, M.S. Dargusch, High stability and high strength β-titanium alloys for additive manufacturing, Mater. Sci. Eng. A. 816 (2021). https://doi.org/10.1016/j.msea.2021.141326.

[14] C.H. Ng, M.J. Bermingham, L. Yuan, M.S. Dargusch, Towards β-fleck defect free additively manufactured titanium alloys by promoting the columnar to equiaxed transition and grain refinement, Acta Mater. 224 (2022) 117511. https://doi.org/10.1016/J.ACTAMAT.2021.117511.

[15] P.A. Kobryn, S.L. Semiatin, Mechanical Properties of Laser-Deposited Ti-6Al-4V P.A. Kobryn and S.L. Semiatin Air Force Research Laboratory, AFRL/MLLMP, Wright-Patterson Air Force Base, OH 45433-7817, in: Int. Solid Free. Fabr. Symp., Austin, TX, 2001: pp. 179–186.

[16] W. Kurz, R. Trivedi, Rapid solidification processing and microstructure formation, Mater. Sci. Eng. A. 179–180 (1994) 46–51. https://doi.org/10.1016/0921-5093(94)90162-7.

[17] A.M. Birt, V.K. Champagne, R.D. Sisson, D. Apelian, Microstructural analysis of Ti-6Al-4V powder for cold gas dynamic spray applications, Adv. Powder Technol. 26 (2015) 1335–1347. https://doi.org/10.1016/j.apt.2015.07.008.

[18] Z.A. Hasenbusch, G. Harvill, K. Ziska, A. Deal, B. Brown, L. Nastac, L.N. Brewer, Influence of Molybdenum on Rapid Solidification Microstructure and Microsegregation in Primary Ferrite Solidified Stainless Steel, Metall. Mater. Trans. A Phys. Metall. Mater. Sci. 54 (2023) 4834–4849. https://doi.org/10.1007/s11661-023-07206-6.

[19] S. Krishnamurthy, A.G. Jackson, H. Jones, F.H. Froes, Beta-Eutectoid decomposition in rapidly solidified titanium-nickel alloys, Metall. Trans. A 1988 191. 19 (1988) 23–33. https://doi.org/10.1007/BF02669812.

[20] Z.A. Hasenbusch, A. Deal, B. Brown, D. Wilson, L.N. Brewer, Z.A. Hasenbusch, A. Deal, B. Brown, D. Wilson, L. Nastac, L.N. Brewer, A Comparison of Solidification Structures and Submicroscale Cellular Segregation in Rapidly Solidified Stainless Steels Produced via Two-Piston Splat Quenching and Laser Powder Bed Fusion A Comparison of Solidification Structures and Submicroscale Cellula, Microsc. Microanal. 29 (n.d.) 1328–1349. https://doi.org/10.1093/micmic/ozad065.

[21] M. Yun, I.-H. Jung, Development of a rapid solidification model for additive manufacturing process and application to Al-Si alloy, Acta Mater. 265 (2023) 119638. https://doi.org/10.1016/j.actamat.2023.119638.

[22] A. Mitchell, A. Kawakami, Segregation and Solidification in Titanium Alloys, (2007) 173–176.

[23] S. Kavousi, B.R. Novak, J. Hoyt, D. Moldovan, Interface kinetics of rapid solidification of binary alloys by atomistic simulations: Application to Ti-Ni alloys, Comput. Mater. Sci. 184 (2020). https://doi.org/10.1016/j.commatsci.2020.109854.

[24] S. Kavousi, B.R. Novak, M.A. Zaeem, D. Moldovan, Combined molecular dynamics and phase field simulation investigations of crystal-melt interfacial properties and dendritic solidification of highly undercooled titanium, Comput. Mater. Sci. 163 (2019) 218–229. https://doi.org/10.1016/j.commatsci.2019.03.024.

[25] A. Mitchell, A. Kawakami, S.L. Cockcroft, Segregation in titanium alloy ingots, High Temp. Mater. Process. 26 (2007) 59–77. https://doi.org/10.1515/HTMP.2007.26.1.59/MACHINEREADABLECITATION/RIS.

[26] M. Keller, A. Chaudhary, S. Kelly, S. Medieros, ABSORPTION COEFFICIENT CHARACTERIZATIONINTI-6AL-4V LASER ADDITIVE MANUFACTURING, Pacific Int. Conf. Appl. Lasers Opt. 1 (2006) 668–675. https://doi.org/10.2351/1.5060759.

[27] L. Nastac, Y. Pang, C.E. Shamblen, Estimation of the Solidification Parameters of Titanium Alloys, Trans. Am. Foundry Soc. 109 (2001) 1–16.

[28] M.J. Aziz, T. Kaplan, Continuous Growth Model for Interface, Acta Metall. Mater. 36

(1988) 2335–2347.

[29] P.K. Galenko, D. Jou, Rapid solidification as non-ergodic phenomenon, Phys. Rep. 818 (2019) 1–70. https://doi.org/10.1016/j.physrep.2019.06.002.

[30] S.L. Sobolev, An analytical model for local-nonequilibrium solute trapping during rapid solidification, Trans. Nonferrous Met. Soc. China (English Ed. 22 (2012) 2749–2755. https://doi.org/10.1016/S1003-6326(11)61528-8.

[31] P. Galenko, Solute trapping and diffusionless solidification in a binary system, Phys. Rev. E - Stat. Nonlinear, Soft Matter Phys. 76 (2007) 1–9. https://doi.org/10.1103/PhysRevE.76.031606.

[32] S.L. Sobolev, Nonlocal diffusion models: Application to rapid solidification of binary mixtures, Int. J. Heat Mass Transf. 71 (2014) 295–302. https://doi.org/10.1016/j.ijheatmasstransfer.2013.12.048.

[33] D. Tourret, J. Klemm-Toole, A.E. Castellanos, B. Rodgers, G. Becker, A. Saville, B. Ellyson, C. Johnson, B. Milligan, J. Copley, R. Ochoa, A. Polonsky, K. Pusch, M.P. Haines, K. Fezzaa, T. Sun, K. Clarke, S. Babu, T. Pollock, A. Karma, A. Clarke, Morphological Stability of Solid-Liquid Interfaces Under Additive Manufacturing Conditions, Acta Mater. 250 (2023) 118858. https://doi.org/10.1016/j.actamat.2023.118858.

[34] D. Tourret, J. Klemm-toole, A.E. Castellanos, B. Rodgers, G. Becker, A. Saville, B. Ellyson, C. Johnson, B. Milligan, J. Copley, R. Ochoa, A. Polonsky, K. Pusch, M.P. Haines, K. Fezzaa, T. Sun, K. Clarke, S. Babu, T. Pollock, A. Karma, A. Clarke, Morphological Stability of Solid-Liquid Interfaces Under Additive Manufacturing Conditions, Acta Mater. (2023) 118858. https://doi.org/10.1016/j.actamat.2023.118858.

[35] S.L. Sobolev, L. V. Poluyanov, F. Liu, An analytical model for solute diffusion in multicomponent alloy solidification, J. Cryst. Growth. 395 (2014) 46–54. https://doi.org/10.1016/j.jcrysgro.2014.03.009.

[36] K.A. Jackson, K.M. Beatty, K.A. Gudgel, An analytical model for non-equilibrium

segregation during crystallization, J. Cryst. Growth. 271 (2004) 481–494. https://doi.org/10.1016/j.jcrysgro.2004.07.073.

[37] W. Kurz, B. Giovanola, R. Trivedi, Theory of Microstructural Development During Rapid Solidification., Acta Met. 34 (1986) 260–267. https://doi.org/10.1007/978-94-009-4456-5_24.

[38] D.M. Herlach, Containerless Undercooling and Solidification of Pure Metals, Annu. Rev. Mater. Sci. 21 (1991) 23–44.

[39] S. Walder, P.L. Ryder, A simple technique for the measurement of dendritic growth rates in undercooled metallic melts and its application to Ni and Ti, Mater. Sci. Eng. A. 203 (1995) 197–202. https://doi.org/10.1016/0921-5093(95)09857-7.

[40] J.D. Hunt, Steady state columnar and equiaxed growth of dendrites and eutectic, Mater. Sci. Eng. 65 (1984) 75–83. https://doi.org/10.1016/0025-5416(84)90201-5.

[41] M. Gäumann, R. Trivedi, W. Kurz, Nucleation ahead of the advancing interface in directional solidification, Mater. Sci. Eng. A. 226–228 (1997) 763–769. https://doi.org/10.1016/s0921-5093(97)80081-0.

[42] M. Haines, A. Plotkowski, C.L. Frederick, E.J. Schwalbach, S.S. Babu, A sensitivity analysis of the columnar-to-equiaxed transition for Ni-based superalloys in electron beam additive manufacturing, Comput. Mater. Sci. 155 (2018) 340–349. https://doi.org/10.1016/j.commatsci.2018.08.064.

[43] M. Gäumann, C. Bezençon, P. Canalis, W. Kurz, Single-crystal laser deposition of superalloys: Processing-microstructure maps, Acta Mater. 49 (2001) 1051–1062. https://doi.org/10.1016/S1359-6454(00)00367-0.

[44] D. Rosenthal, The Theory of Moving Sources of Heat and Its Application to Metal Treatments, J. Fluids Eng. Trans. ASME. 68 (1946) 865. https://doi.org/10.1115/1.4018625.

[45] U. Scipioni Bertoli, B.E. MacDonald, J.M. Schoenung, Stability of cellular microstructure

in laser powder bed fusion of 316L stainless steel, Mater. Sci. Eng. A. 739 (2019) 109–117. https://doi.org/10.1016/j.msea.2018.10.051.

[46] Z. Yan, W. Liu, Z. Tang, X. Liu, N. Zhang, M. Li, H. Zhang, Review on thermal analysis in laser-based additive manufacturing, Opt. Laser Technol. 106 (2018) 427–441. https://doi.org/10.1016/j.optlastec.2018.04.034.

[47] X. Liang, E.J. Lavernia, Solidification and microstructure evolution during spray atomization and deposition of Ni3Al, Mater. Sci. Eng. A. 161 (1993) 221–235. https://doi.org/10.1016/0921-5093(93)90517-I.

[48] L. Nastac, Splat Quench Mapping of Titanium Additive Manufacturing: Fluent Modeling and Analysis, 2024.

[49] C. Jasien, A. Saville, C.G. Becker, J. Klemm-Toole, K. Fezzaa, T. Sun, T. Pollock, A.J. Clarke, In Situ X-ray Radiography and Computational Modeling to Predict Grain Morphology in β-Titanium during Simulated Additive Manufacturing, Metals (Basel). 12 (2022) 1–15. https://doi.org/10.3390/met12071217.

[50] C.H. Ng, M.J. Bermingham, M.S. Dargusch, Eliminating segregation defects during additive manufacturing of high strength β-titanium alloys, Addit. Manuf. 39 (2021). https://doi.org/10.1016/j.addma.2021.101855.

[51] W. Kurz, R. Trivedi, Banded solidification microstructures, Metall. Mater. Trans. A Phys. Metall. Mater. Sci. 27 (1996) 625–634. https://doi.org/10.1007/BF02648951.

CHAPTER 5 – SUMMARY, CONCLUSIONS AND FUTURE WORK

5.0.0 Summary

This dissertation has been focused on the growing need for material studies at rapid solidification conditions. The need has grown as the field of additive manufacturing (AM) has developed due to the inherent solidification and cooling conditions that are generated in high power density melting techniques used in beam-based AM processes. This dissertation focused on three areas of study in the field of rapid solidification and alloy design. The first was focused on exploration and elucidation of the use of splat quenching as a means to study rapid solidification of AM alloys. The second chapter was then related to using the splat quenching process to evaluate the stability to compositional variance on the as-quenched phase content of the Ti-5553 compositional space. The final chapter was implementing splat quenching alongside other solidification processing techniques to study and model the solidification response in Ti-5553 throughout a range of conditions. The culmination of the work can be seen largely summarized in three main contributions:

- Providing an increased understanding of splat quenching as a technique for alloy design and compositional control in rapid solidification.
- Exploration of the Ti-5553 alloy space through the use of splat quenching to investigate the stability of the current compositional standard (AMS 7026).
- Furthering the fundamental solidification understanding of the beta titanium family as a whole.

5.1.0 Splat Quenching

Splat quenching is a technique that has a potential to be a valuable tool for high throughput alloy design for AM applications but lacks a clear understanding of the heat transfer that underlines the technique. As such, Chapter 2 of this dissertation highlights this need and seeks to address it by a combination of analytical models, experimental results, and heat transfer simulation techniques. Adapting analytical models developed for thermal spray processes allowed for an understanding of the effect of processing variables such as superheat, substrate material, and impact velocity as well as the effect of material properties such as thermal conductivity, surface tension, and density resulting splat quenched sample. As expected, increasing the platen velocity results in a higher impact pressure and thereby a thinner foil as a result, but interestingly the contact pressure is also linearly related to the density of the liquid. Thereby, as seen experimentally, the higher density materials such as SS316 or In625 with densities of 7340 and 7600 kg/m3 respectively have nearly half the thickness of a Ti-5553 splat with a density of 4315 kg/m3.

The dynamic event of the splatting process was highlighted as a reason for variance in thickness throughout the sample that offered a wider range of solidification conditions that can be observed in a single sample. The droplet is partially cooled during the deformation process but at much lower heat transfer rates as compared to the edges of the splat that are formed by jetting upon collision of the platens. The importance of the melt superheat comes into play here as solidification can occur prior to the platen collision. The result of this two stage cooling is a gradient in pressure along the radius of the samples. This process also results in a radial reduction in splat thickness as well. The heat transfer coefficient could be calculated from Eqn.

X, given below, and was originally developed for thermal spray processing to offer an estimate as a function of pressure and material properties of the melt.

$$h = \frac{k_w \rho_c}{R_a[\rho_c + \pi\sigma/(4R_a)]} \quad (1)$$

A splat quenched foil was found to be a window across a range of rapid solidification conditions due to variation in splat thickness and heat transfer coefficient both radially and through thickness. As a testing and screening tool for rapid solidification response, a wider window does allow for an increase in the understanding provided by a singular sample. FLUENT simulations allowed for an understanding of the cooling rate across a range of conditions including variation in thickness, heat transfer coefficient, and material splatted. The range of cooling rate is from 10^6-10^9 °K/s with the thickness of the sample and the heat transfer coefficient offering significant changes to the expected cooling rates. The doubling of the splat thickness resulted in nearly half an order of magnitude cooling rate drop at the center, while an order of magnitude drop in heat transfer coefficient resulted in only halving the cooling rate. Experimental cell size data similarly demonstrated that both the thickness and heat transfer coefficient can be modified by testing parameters such as platen velocity to push the alloy into regions that better reflect the desired rapid solidification processes.

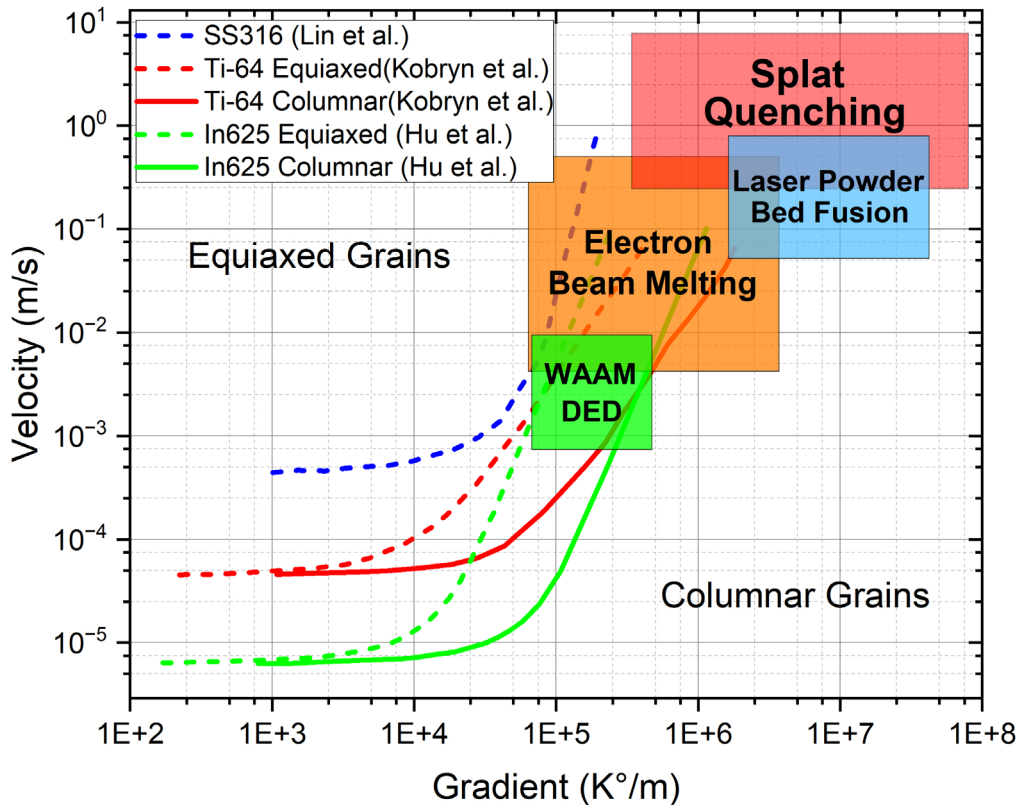

Figure 5.1 Map of the typical thermal gradients and soldiifcation veloicties for different additive manufacturing techniques in comparision with splat quenching [26–30]. There is signficant overlap for laser and electron beam techniques and splat quenching, while lower power density techniques such as directed energy deposition and wire arc additive manufacturing are much slower than what is achieved in splat quenching.

5.2.0 Martensitic stability

Metastable beta alloys such as Ti-5553 are compositionally placed in an interesting intersection between martensite phase formation and BCC phase retention that can affect the finished component both crystallographically and mechanically. As such, exploration of the alloy composition was conducted using the splat quenching technique outlined in Chapter 2 with particular attention to the formation of martensite in the as-splat quenched condition. The stability of the metastable BCC alloy was tested using the splat quenching technique with a focus

to the composition region outlined by AMS 7026. A sensitivity to martensite was found in the beta-solute-lean region outside the AMS 7026 standard. The SQ approach allowed for a sampling of the alloy space that could then be used to validate models such as molybdenum equivalency and martensitic start temperature to the phases found in the alloys after splat quenching. X-ray diffraction revealed the phases of the splat quenched foils as well as allowing for tracking of lattice parameters changes across the compositions.

The 19 alloys created for this study were used to calibrate martensite models with the martensitic start temperature and martensite nucleation parameter proving able to separate the martensitic from the stable alloys. Empirical models such as the molybdenum equivalency were used to separate the alloys, but the overlap of the martensitic and BCC alloys meant that the usability of these models was limited. The use of a martensitic start temperature offered a more reliable metric as the empirical equation was based off the martensitic transformation itself and not the equilibrium phase content like the molybdenum equivalency. However, both the empirical nature of the martensitic start temperature and its lack of interstitial elements limited the appeal of this approach. A martensitic driving parameter was previously developed by Bignon et al. that addressed both of these concerns. The use of thermodynamic principals like the T_0 temperature along with structural terms such as a shear modulus and lattice parameter offer a more controlled and physics based model to estimate the potential for martensite formation. The model was found to correlate well with the experimental data and could be easily modeled to include interstitial data through the use of CALPHAD for T_0 temperature and literature values for the changes to the shear modulus as a function of oxygen. Interestingly, the T_0 temperature was found to be able to separate the martensitic transition on its own due to the small change in shear modulus and lattice parameter in the compositional standard. Therefore, the final result of

this chapter is establishing limits of BCC stability to provide the compositional stability of the BCC phase in the Ti-5553 alloy for use in industrial application as well as further validate and refine the martensitic predictive tools in metastable beta titanium alloys.

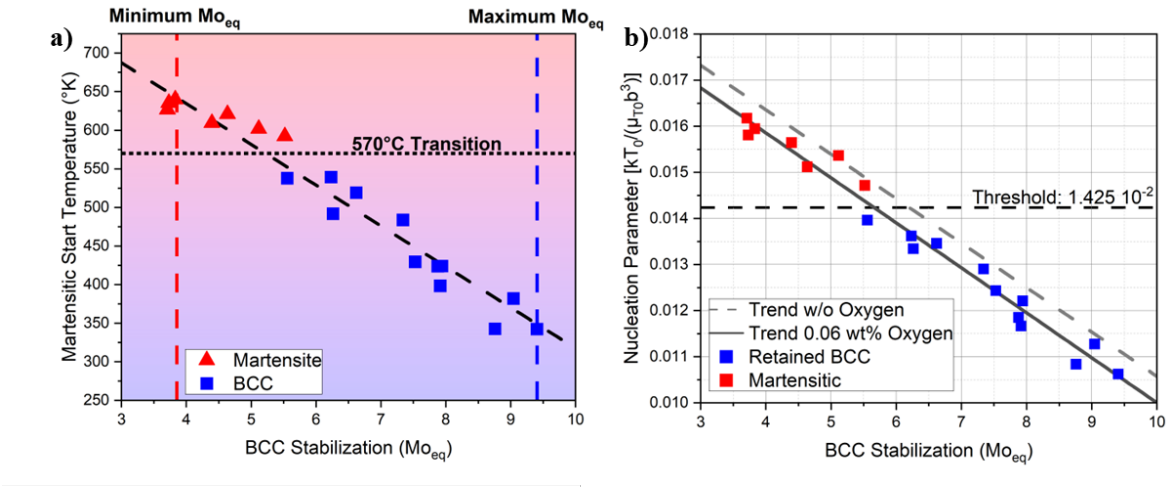

Figure 5.2 (a) Martensitic start temperature correlated to molybdenum equivalency for the Ti-5553 based alloys with delineation for the edges of the AMS 7026 composition standard. (b) Martensitic nucleation parameter as a function of BCC stabilization of the Ti-5553 alloys highlighting the experimentally determined threshold for forming martensite across the Ti-5553 based alloys as well as the effect of oxygen in lowering alloys toward BCC stabilization

5.3.0 Rapid Solidification

Chapter 4 took a wide breadth of the rapid solidification conditions for Ti-5553 to provide an understanding of the segregation and solidification structure that form in rapid solidification processes such as additive manufacturing. Three rapid solidification techniques, plasma atomization, laser welding, and splat quenching addressed several key solidification phenomena, namely partition coefficient, tip radius, tip undercooling, expected segregation, and the columnar to equiaxed transition. Using these experimental techniques the solidification

behavior of Ti-5553 was characterized and compared to models to elucidate the solidification behavior in processes such as atomization, welding, and additive manufacturing. Titanium as an alloy class especially beta titanium alloys are an underserved area of research in the field of solidification. Therefore, there is a significant need to understand and characterize the solidification response of titanium at the high solidification velocity and thermal gradient that are inherent in the modern processing routes utilized today. The evaluation of the breadth of solidification parameters allows for a conceptual understanding of the Ti-5553 solidification behavior.

The segregation is the most important parameter to understand in the solidification of the titanium alloys due to the potential for detrimental intermetallic formation due to iron and chromium additions. Several models have been developed to capture the effect of solidification velocity on the partition coefficient, varying from numerical solutions with minimal assumption to analytical models assuming local equilibrium. However, a local nonequilibrium model has been developed by Sobolev et al. that was seen to more strongly capture the transition experimentally observed in this dissertation [2]. Implementing the model furthermore allowed for investigation on the relative changes of the various solute additions as a function of solidification velocity. Slower diffusing solutes such as molybdenum may be fully entrapped at velocities that may still experience segregation of faster diffusing solutes such chromium or iron. The drop in segregation was seen experimentally through the use of EDS line scans across cells in powder, splat quenched samples, and a laser weld. The laser welded sample (V=0.55 m/s) did not display enough segregation to be detected by EDS even with the presence cells clearly being seen from etching. So, EDS, while an imperfect tool, does demonstrate a decrease in partition coefficient as a function of solidification velocity to regions that are difficult to measure.

The dendritic tip radius is a valuable tool to understand the length scale variance as a function of solidification velocity and thermal gradient that was implemented for the first time for a beta titanium alloy to understand rapid solidification conditions on the solidification structure. The use of the KGT marginal stability model was implemented for the Ti-5553 alloy that incorporates the constitutional and curvature undercooling to predict the stability of limit of the solid-liquid interface [3,4]. The use of the model then allows for a conservative estimate of the cell size as a function of solidification velocity that can be used to solve for solidus, liquidus, and tip undercooling temperatures to see the effect that the solidification velocity has on these important alloy parameters. The key trend noticed both in these parameters as well as in the partition coefficient is a narrowing of difference between the solid and liquid both due to a reduction in solute segregation as well as the solidus and liquidus temperatures converging to the T_0 temperature. With a deeper understanding of the change in constitutional undercooling as a function of solidification velocity, a modification of Hunt's model can be used to attempt to predict the columnar to equiaxed transition, Figure 5.3a. The ability to plot the constitutional undercooling as a function of velocity gave a unique ability to capture the higher velocity region of the CET map as seen below, where columnar is expected to dominant at high solidification velocity due to the reduction in undercooling from solute segregation. At even higher solidification velocities other phenomenon begin to dominant including attachment kinetics. The result is that through the various solidification methods, the CET space is outlined with powder, droplet, and the center of the splat quenched samples demonstrating equiaxed grains while the laser weld and thinner splat quenched regions having a columnar structure. Of interest is that the undercooling needed to nucleate equiaxed grains is much higher than other alloys such as Al-Cu meaning that the columnar grains dominant at low velocities as well as high thermal gradients.

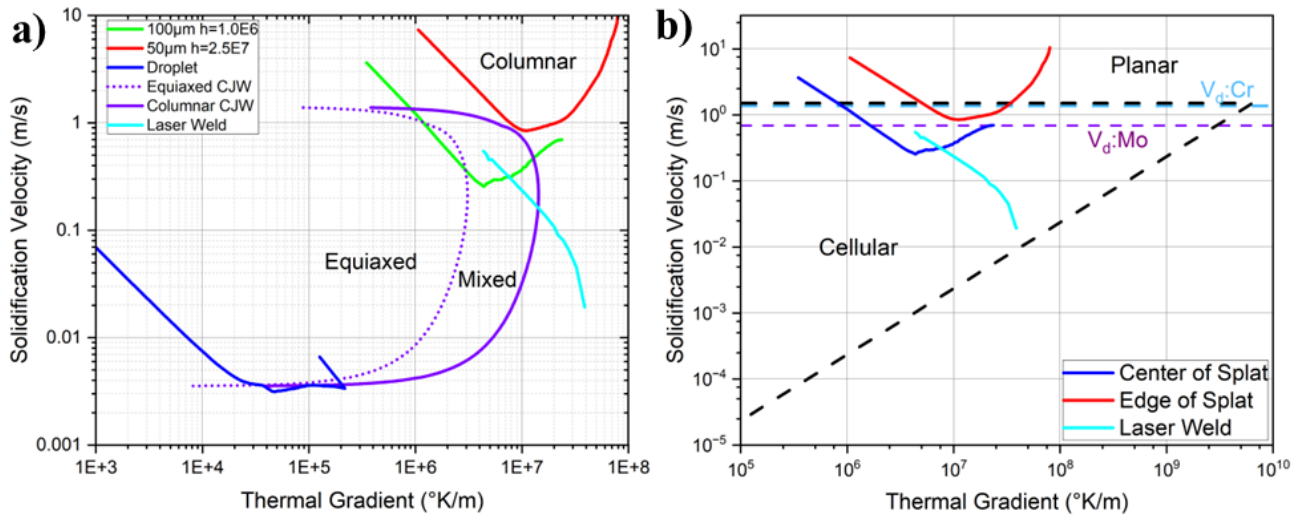

Figure 5.3 (a) Map of thermal gradient versus solidification velocity across splat quenching, single laser track remelting, and molten droplet. (b)The plotted columnar to equiaxed transition are plotted onto the map to demonstrate the change in solidification structure from columnar to equiaxed throughout the various solidification processes. The limit of diffusion of Cr and Mo (V_d) is plotted to demonstrate that Mo is predicted to be fully trapped at higher velocities while Cr may still segregate.

Through a combination of models, this work is the to provide an understanding of the solidification morphology of Ti-5553 correlating the cell size to cooling rate and solidification velocity. Measurement of the cell size allowed for correlation to the marginal stability prediction as well as the cooling rate to provide an understanding of the evolution of the solidification structure at rapid solidification conditions. The marginal stability model is not a wholly accurate tool for prediction of the cell size especially in rapid solidification conditions due to several limitations in the model's approach such as anisotropy of attachment. In spite of this, the marginal stability does largely provide a tool to understand the limits on cellular growth that reasonable agreed with the appearance of cells in the splat quenched model that was seen

through simulation to range in solidification velocity from 0.25-10 m/s. Additionally, the empirical approach of plotting cooling rate to characteristic length also provides a way to view the transition in solid-liquid perturbation size as a function of cooling rate. The end result of this chapter is a combination of experimental measurements ranging from segregation across cell boundaries as well as the cell spacing that is correlated to simulated cooling rates and solidification velocity. These measurements provide a background in the solidification behavior of titanium that is limited in supply from the existing literature.

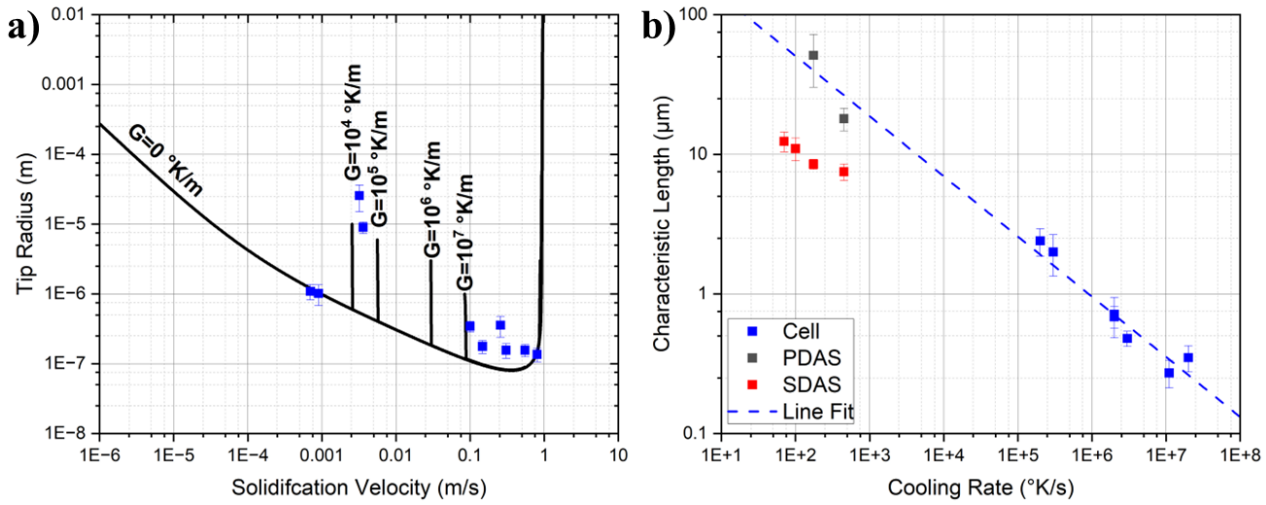

Figure 5.4 (a) The same cellular-dendritic sizes correlated to the KGT interfacial stability model. (b) Correlation between the cells sizes measured correlated to the calculated cooling rates in both the dendritic region, seen in the substrate cooled droplet, and the cellular region, laser welding, powder, splat quenching.

5.4.0 Recommendations for future work

Future work to build upon the foundation of this dissertation could expand in three key areas. The first is adapting and developing a method for calibrating and subsequently modelling the partition coefficient of solute across the solidification regime. The second is to modify the rapidly solidified material with additional heat input to model the elevated temperature the AM

build retains as well as the subsequent heat treatment applied to the material. The final area of interest in the titanium alloy space would be to study the formation of the omega phase as a function of composition variation to understand its formation in Ti-5553. These possible ideas are subsequently laid out in detail, but each provides a clear direction of continuing growth of the field of additive manufacturing and result in a deeper understanding of the titanium alloy systems for further development in composition and processing route.

5.4.1 Segregation

The segregation of solute in an additive manufacturing alloy is difficult to predict but critical for understanding the limits on the alloy design and to provide the highest quality final component without the detriment of unwanted phase development. The core of existing partition coefficient data is generated from slow solidification process that allow for controlled growth that can then be measured over millimeters, such as work by Mitchell et al. in Figure 5.11. This data provides a (near) equilibrium value that is fundamentally important but the reduction in partition coefficient as a function of velocity is difficult to model in any system let alone titanium due to the limited experimental data to accurately model. There have been previous works, especially in semiconductors, that have used repeatable solidification events to map out the segregation across cells by laser pulse experiments [5,6]. Other processes, such as directional furnaces, could be envisioned to provide similar data but the issue with many of these techniques is the cleanliness required of titanium alloys, as well as, the difficulty to control the solidification velocity at speeds near or above 1 m/s [7]. While splat quenching was used extensively in this dissertation, this technique inherently has variation from sample-to-sample and several assumptions that provide a range of solidification velocities rather than a set repeatable value. Thus, a laser controlled method offers the ability to retain the cleanliness needed, fine control of

heat input, and immediately applicable thermal models to provide solidification velocity estimations.

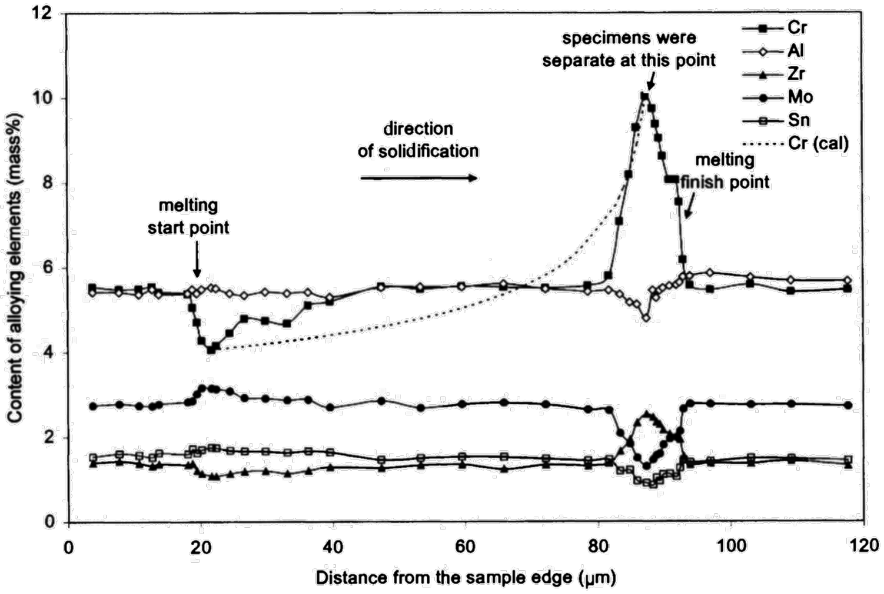

Figure 5.5 Segregation data from zone melted Ti-17 alloy (Ti-5Al-2Sn-2Zr-4Mo4Cr) [8].

The development and use of laser remelting experiment to provide a systematic study of segregation in an alloy system has immediate benefits for the current alloy but will also benefit the field of alloy design in RS techniques by providing limits to expected segregation during processing. The combination of thermal models such as Rosenthal or higher fidelity numerical models would provide the window of solidification velocity and thermal gradients needed to understand the solidification conditions at points that could then be processed through a technique such as atom probe tomography (APT) that is able to do mass spectroscopy on locally chosen material volumes. The precise nature of the material volume selected would then allow for sampling across cell to quantitatively understand the solute profile. The experimental processes could then be implemented across several laser remelting across the range of 0.1 to 1.5 m/s to accurately plot and fit this region of space that was found to be the transition to planar solidification in Chapter 4.

5.4.2 Heat input evolution of the rapidly solidified microstructure

The core of this dissertation is focused on the initial solidification and cooling event; however, the building of an additively manufactured component involves extended heat input from subsequent layers that can affect the final microstructure. The metastable beta titanium family, as a whole, has a sensitivity to low temperature ω phase transformations that can be in seen in differential scanning calorimetry to occur between 100°C and 500°C [9–11]. Whether by build table preheat or by heating of the material by subsequent layers, additional heat is input into the material especially in the case of electron beam additive manufacturing, where due to its vacuum environment, temperatures can reach the range of 600-750°C and rapid cooling is challenging [12]. The next step for the work presented in this dissertation would be to take the rapidly solidified material and apply various heat treatment steps to simulate the exposure time for AM processes.

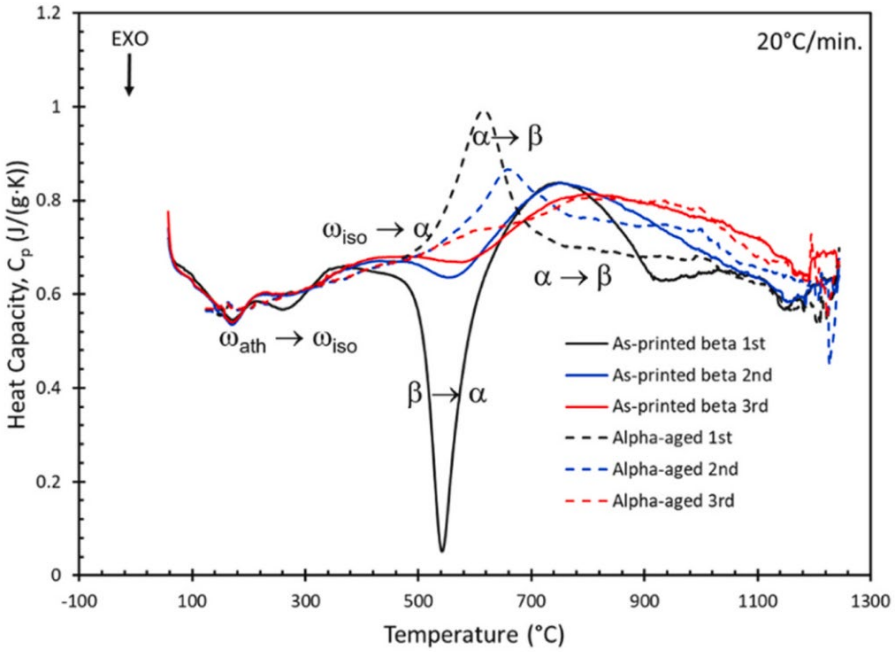

Figure 5.6 Heat capacity of AM Ti-5553 in the as-printed and aged condition [9].

Particular attention on the formation of the ω phase is difficult due to its small size, requiring the use of nanoscale characterization techniques. The small size (~10 nm) of the ω phase results in significant line broadening that means identification in XRD becomes difficult. However, the ω phase has key diffraction markers in electron diffraction that are easily seen in the <110> zone axis orientation. The creation of numerous TEM samples is possible and could result in seeing the presence of the ω phase as a function of heat input. However, the same could be done with in situ TEM heating through the use of a platform such as the DENS "wildfire" chip. The "wildfire" chip allows for attachment of a TEM sample to a micro-electro-mechanical system (MEMS) that can provide heating up to 1300°C, allowing for modeling the temperature exposure in an AM component. The material response in diffraction space could then be analyzed in real time to detect and monitor the growth of the omega phase. Additional imaging and x-ray energy dispersive spectroscopy can be employed to map the chemical segregation and the evolution of the rapidly solidified material.

5.4.3 Compositional control of omega formation

The subject of Chapter 3 was focusing on the formation of martensite in the metastable beta titanium alloy Ti-5553, however, the omega phase plays a more important role in determining the mechanical properties of the manufactured component and needs additional study. The role of composition on the presence and stability of the ω phase is unknown for the Ti-5553 composition space. Therefore, the constraints on the alloy's composition are suited to prevent martensite and to promote the precipitation of the HCP α phase during heat treatment. The formation and development of the ω phase is complicated, having both an athermal displacive method of formation, as well as thermally activated varieties that is related to solute segregation to the phase boundary. The athermal variety forms upon quenching at high cooling rates and requires a diffraction-based technique such as TEM selected area diffraction to see due

to the lack of segregation. The lack of solute segregation in athermally produced ω phase has been found in Ti-Mo[13] and Ti-V [14], though a complete study has not been conducted for a more complicated alloy (e.g. Ti-5553) with fast diffusing elements such as Cr and Fe. The isothermal omega has been demonstrated to result in the segregation of all solute to the omega-BCC boundary using atom probe tomography (APT) [15–20].

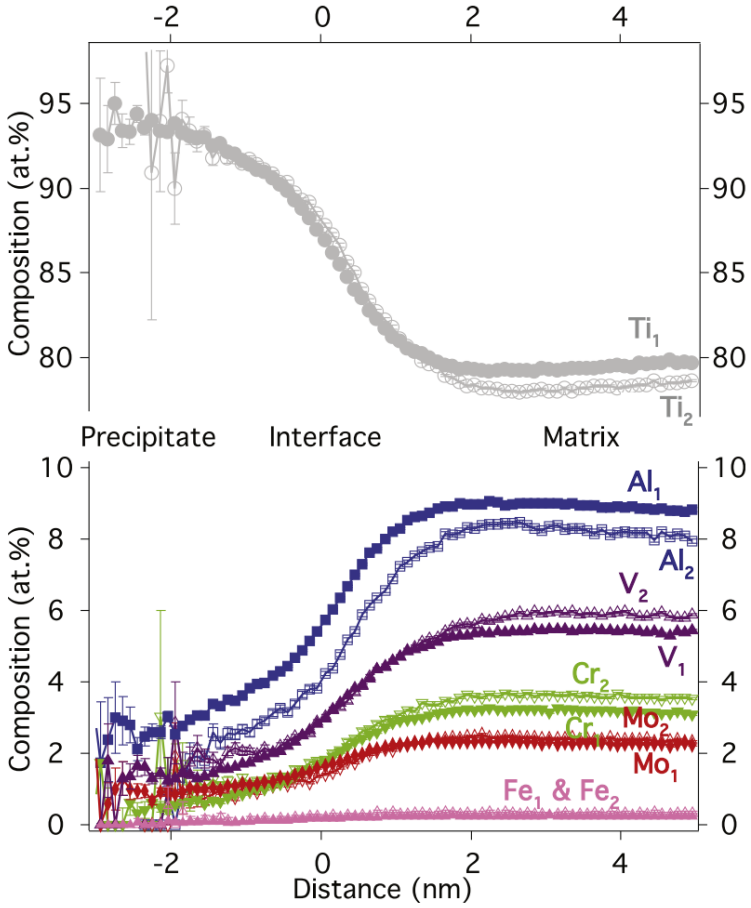

Figure 5.7 Atom probe tomography proxigrams of Ti-5553 held at 300°C for 8 hours demonstrating the segregation of the omega precipitate [21].

The relationship between isothermal and athermal omega phase is still unclear, but important. The trend of the research to look at the thermally activated omega phase leaves questions as to the stability of the athermal variety and fundamental questions on how to avoid

the detrimental phase. The suppression of athermal omega has not been clearly linked to the repression of the thermally activated variety though the theories of solute being diffused from the omega would lead to the belief that there is a relationship. Additionally, the probing of the Ti-5553 composition corners would allow for an understanding of the necessary changes to the alloy could be considered to limit the development of omega either from quenching or heat exposure such as during printing.

5.5.0 Conclusions

In summary, this dissertation is focused on the rapid solidification and quenching of beta titanium alloy Ti-5553 with a focus on understanding the potential of splat quenching to fill a current need for alloy design in additive manufacturing. The current approach to studying alloy design for AM requires atomization and powder processing, requiring significant time, money, and resources that can be greatly reduced through the use of splat quenching. The use of splat quenching can then allow for answering questions such as the formation of secondary phases in common AM alloys such as Ti-5553. The ability to create a wide array of alloy compositions allowed for analysis on the martensite formation with potential for using the same process to analyze omega formation. The use of splat quenched, laser welded, and plasma atomized samples of the same alloy allowed for correlation between the various rapid solidification processing routes and their final solidification structure. The key findings of the dissertation are given here:

- The cooling rates of the splat quenching process were found through simulation and experiment to range from 10^6-10^8 °K/s. These cooling rates position SQ to reach solidification velocities and cooling rates that match and can exceed laser bed powder fusion though well beyond directed energy deposition processes.

- Considerable success was achieved in elucidating the splat quenching processes through the use of analytical models adapted from thermal spray. These analytical models gave several key parameters that could be correlated to the cooling rate of SQ, namely substrate roughness, substrate material, and platen velocity. The substrate roughness was not found to be a critical factor due to material flow at the substrate interface, resulting in a lack of intimate liquid metal-solid substrate contact. The platen velocity, however, did produce a distinct change in splat thickness that offered the most direct control of the SQ cooling rate.
- SQ testing of alloys within the compositional standard AMS 7026 for Ti-5553 revealed no martensitic sensitivity from rapid quenching from the melt. The martensitic start temperature (M_s) and martensite nucleation parameter were the two methods that were found to successfully predict the formation of martensite. A M_s of 570°C and a nucleation parameter of $1.425 \cdot 10^{-2}$ were found to be the transition point for the formation of martensite in the near Ti-5553 alloy space.
- Solidification models were adapted to the Ti-5553 system across a range of solidification velocities present in laser welding, atomization, and splat quenching. Planar stability at high solidification velocities was reached by splat quenching (V=0.1-10 m/s) but did not occur during laser welding (V=0.55 m/s), matching the marginal stability model prediction. The calculated cooling rate for the various solidification techniques allowed for fitting of a cooling rate to cell size relationship of $\lambda = 454 CR^{-0.453}$. The columnar-to-equiaxed grain structure map demonstrated a significant undercooling needed to nucleate equiaxed grains. This result underscores the difficulty of eliminating columnar grain growth for AM processes with titanium alloys such as Ti-5553 and Ti-64.

References

[1] C.J. Li, J.L. Li, Transient contact pressure during flattening of thermal spray droplet and its effect on splat formation, J. Therm. Spray Technol. 13 (2004) 229–238. https://doi.org/10.1361/10599630418158.

[2] S.L. Sobolev, L. V. Poluyanov, F. Liu, An analytical model for solute diffusion in multicomponent alloy solidification, J. Cryst. Growth. 395 (2014) 46–54. https://doi.org/10.1016/j.jcrysgro.2014.03.009.

[3] D. Tourret, J. Klemm-toole, A.E. Castellanos, B. Rodgers, G. Becker, A. Saville, B. Ellyson, C. Johnson, B. Milligan, J. Copley, R. Ochoa, A. Polonsky, K. Pusch, M.P. Haines, K. Fezzaa, T. Sun, K. Clarke, S. Babu, T. Pollock, A. Karma, A. Clarke, Morphological Stability of Solid-Liquid Interfaces Under Additive Manufacturing Conditions, Acta Mater. (2023) 118858. https://doi.org/10.1016/j.actamat.2023.118858.

[4] W. Kurz, P. Gilgien, Selection of microstructures in rapid solidification processing, Mater. Sci. Eng. A. 178 (1994) 171–178. https://doi.org/10.1016/0921-5093(94)90538-X.

[5] J.A. Kittl, M.J. Aziz, D.P. Brunco, M.O. Thompson, Nonequilibrium partitioning during rapid solidification of SiAs alloys, J. Cryst. Growth. 148 (1995) 172–182. https://doi.org/10.1016/0022-0248(94)00836-1.

[6] D.P. Brunco, M.O. Thompson, D.E. Hoglund, M.J. Aziz, H.J. Gossmann, Germanium partitioning in silicon during rapid solidification, J. Appl. Phys. 78 (1995) 1575–1582. https://doi.org/10.1063/1.360251.

[7] J.A. Sarreal, G.J. ABbaschian, The effect of solidification rate on microsegregation, Metall. Trans. A. 17 (1986) 2063–2073. https://doi.org/10.1007/BF02645003.

[8] A. Mitchell, A. Kawakami, S.L. Cockcroft, Segregation in titanium alloy ingots, High Temp. Mater. Process. 26 (2007) 59–77. https://doi.org/10.1515/HTMP.2007.26.1.59/MACHINEREADABLECITATION/RIS.

[9] P. Yang, K.L. Johnson, J.D. Carroll, J.L. Buckner, M.A. Blea-Kirby, C. Groves, E.N. Coker, Thermophysical properties of additively manufactured Ti-5553 alloy, Addit. Manuf. 76 (2023) 103769. https://doi.org/10.1016/j.addma.2023.103769.

[10] Y. Zheng, R.E.A. Williams, H.L. Fraser, Characterization of a previously unidentified ordered orthorhombic metastable phase in Ti-5Al-5Mo-5V-3Cr, Scr. Mater. 113 (2016) 202–205. https://doi.org/10.1016/J.SCRIPTAMAT.2015.10.037.

[11] D. Sharma, D. Parfitt, B. Chen, B. Roebuck, D.A. Venero, S.R. Kada, D. Fabijanic, M.E. Fitzpatrick, Influence of cooling rate on the precipitation kinetics of nanoscale isothermal ω-phase in metastable β-Ti alloy, Ti–5Al–5Mo–5V–3Cr, J. Alloys Compd. 859 (2021) 1–33. https://doi.org/10.1016/j.jallcom.2020.157822.

[12] S. Liu, Y.C. Shin, Additive manufacturing of Ti6Al4V alloy: A review, Mater. Des. 164

(2019) 107552. https://doi.org/10.1016/J.MATDES.2018.107552.

[13] M.J. Lai, T. Li, F.K. Yan, J.S. Li, D. Raabe, Revisiting ω phase embrittlement in metastable β titanium alloys: Role of elemental partitioning, Scr. Mater. 193 (2021) 38–42. https://doi.org/10.1016/j.scriptamat.2020.10.031.

[14] M.S.K.K.Y. Nartu, S. Dasari, A. Sharma, S.A. Mantri, S. Sharma, M. V. Pantawane, B. McWilliams, K. Cho, N.B. Dahotre, R. Banerjee, Omega versus alpha precipitation mediated by process parameters in additively manufactured high strength Ti–1Al–8V–5Fe alloy and its impact on mechanical properties, Mater. Sci. Eng. A. 821 (2021) 141627. https://doi.org/10.1016/j.msea.2021.141627.

[15] S.P. Narra, R. Cunningham, J. Beuth, A.D. Rollett, Location specific solidification microstructure control in electron beam melting of Ti-6Al-4V, Addit. Manuf. 19 (2018) 160–166. https://doi.org/10.1016/j.addma.2017.10.003.

[16] J.A. Ballor, T. Li, F. Prima, C.J. Boehlert, A. Devaraj, A review of the metastable omega phase in beta titanium alloys: the phase transformation mechanisms and its effect on mechanical properties, Int. Mater. Rev. 68 (2023) 26–45. https://doi.org/10.1080/09506608.2022.2036401.

[17] S. Nag, R. Banerjee, R. Srinivasan, J.Y. Hwang, M. Harper, H.L. Fraser, ω-Assisted nucleation and growth of α precipitates in the Ti-5Al-5Mo-5V-3Cr-0.5Fe β titanium alloy, Acta Mater. 57 (2009) 2136–2147. https://doi.org/10.1016/j.actamat.2009.01.007.

[18] Y. Zheng, R.E.A. Williams, D. Wang, R. Shi, S. Nag, P. Kami, J.M. Sosa, R. Banerjee, Y. Wang, H.L. Fraser, Role of ω phase in the formation of extremely refined intragranular α precipitates in metastable β-titanium alloys, Acta Mater. 103 (2016) 850–858. https://doi.org/10.1016/j.actamat.2015.11.020.

[19] J. Coakley, V.A. Vorontsov, N.G. Jones, A. Radecka, P.A.J. Bagot, K.C. Littrell, R.K. Heenan, F. Hu, A.P. Magyar, D.C. Bell, D. Dye, Precipitation processes in the Beta-Titanium alloy Ti-5Al-5Mo-5V-3Cr, J. Alloys Compd. 646 (2015) 946–953. https://doi.org/10.1016/j.jallcom.2015.05.251.

[20] J. Coakley, A. Radecka, D. Dye, P.A.J. Bagot, T.L. Martin, T.J. Prosa, Y. Chen, H.J. Stone, D.N. Seidman, D. Isheim, Characterizing nanoscale precipitation in a titanium alloy by laser-assisted atom probe tomography, Mater. Charact. 141 (2018) 129–138. https://doi.org/10.1016/j.matchar.2018.04.016.

[21] J. Coakley, V.A. Vorontsov, N.G. Jones, A. Radecka, P.A.J. Bagot, K.C. Littrell, R.K. Heenan, F. Hu, A.P. Magyar, D.C. Bell, D. Dye, Precipitation processes in the Beta-Titanium alloy Ti–5Al–5Mo–5V–3Cr, J. Alloys Compd. 646 (2015) 946–953. https://doi.org/10.1016/J.JALLCOM.2015.05.251.

APPENDIX A
MATLAB SCRIPTS

A.1 Marginal Stability Calculation

```
%Variables for Code

V=logspace(log10(10.^-7),log10(1*10.^2),1000);

Vz=V';vabssum=0;vcsum=0;

% V Cr Mo Al Fe

k0= [.95 .74 1.15 1.06 .38];%Mitchell

%k0= [.95 .77 1.28 1.05 .86];%Experimental

%m0= [ -7.0242 -7.3387 9.44 -.8677 -9.8611];

m0= [ -6.98 -7.33 9.44 -1.11 -9.8611];

%m0= [ -7 -11.18 4.88 -3.53 -15.25];

%m0= [ -7 -11.18 4.88 -3.53 -15.25];

c0=[5 3 5 5 .4];

cwt=[5 3 5 5 .4]; cL=[];

D=[5.61096E-09 5.73242E-09 3.67226E-09 9.41765E-09 6.88348E-09];

Pe=[];x=[0 0 0 0 0];

c=[];ctot=[];mtot=[];mv=[];iv=[];

vd=[1,5]; vc=[1,5]; vabs=[1,5];

q=0;

A=25;

R0=.0003;mco=24/35;
```

```
Rz=zeros(1,length(V));

KGTin=[1,5];

KGTsum=0;

xi=[1,5];

q=false;a0=3.27E-10; GT= 7.8*10.^-8; %7.8*10.^-8;

TipT=[]; Tm=(1670+273); Tsum=0;

Tsv=[]; Tlv=[]; Ts=0;Tl=0;

mu=.74; %Kavousi 2019

G=10^6;%Thermal Gradient

%Calculation of velocities values for each solute

for i = 1:5

%vd (i) =.207*(log(1/k0(i))/(1-k0(i)))*D(i)/(1.0*10.^-9);

%vd (i) =0.207*(log(1/k0(i))/(1-k0(i)))*D(i)/(2.6*10.^-9);

vd (i) =D(i)/(2.6*10.^-9);

%vdi (i)=(D(i)/(10E-11)).^0.5; %Galenko

%vdi (i)=(D(i)/26E-10); %Galenko

%vd(i)=D(i)/(26*10^-10); %from Kavousi

vabs(i)=D(i)*m0(i)*(k0(i)-1)*cwt(i)/(k0(i));

vc (i)=m0(i)*(k0(i)-1)*cwt(i)/(D(i)*k0(i));

vabssum=vabssum+vabs(i);

vcsum=vcsum+vc(i);

end

vabssum=vabssum/GT;

for j =1:length(V)

%Calculation of k as a function of velocity
```

```
for i = 1:5
    if V(j)>vd(i)
       k(j,i)=1;
    else
        k(j,i)= k0(i).^(1/((1+vd(i)*(A/vd(i))*(V(j)/vd(i)))/(1-(V(j)/vd(i)))));
    end
Pe(j,i)=(R0*V(j)/(2*D(i)));
%ivantsov solution
iv(j,i)=Pe(j,i)*exp(Pe(j,i))*expint(Pe(j,i));
    q=isnan(iv(j,i));
    w=isinf(iv(j,i));
    if q==true || w==true
       iv(j,i)=1;
    end
    if j==1
      c(j,i)=c0(i);
    end
 if j>1
 c(j,i)=c0(i)/(1-(1-k(j,i))*iv(j,i));
 end
%Calculation of m as a function of velocity
 if V(j)>vd(i)
       mv(j,i)=m0(i)*log(k0(i))/(k0(i)-1);
   else
        mv(j,i)=m0(i)*(1-k(j,i)+((k(j,i)+(1-k(j,i))*mco))*log(k(j,i)/k0(i)))/(1-k0(i));
   end
```

```
ctot(j,i)=c(i);
delT(j,i)=(mv(j,i)*ctot(j,i))/(1-(1-k(j,i)*iv(j,i)));
xi(j,i)=1-2*k(j,i)/((1+(2*3.1415/(Pe(j,i))).^2).^0.5-1+2*k(j,i));
KGTin(j,i)=(Pe(j,i)*mv(j,i)*c(j,i)*(1-k(j,i))*xi(j,i))/(1-((1-k(j,i))*iv(j,i)));
KGTsum=KGTsum+KGTin(j,i);
end
qz=0;
%Actual KGT model that iterates up to a number of times to find a stable value for R
while qz<200
    options = optimset('fminsearch');
    options.TolFun = 10.^-10; % Set the tolerance on the function value to 10^-12
    options.MaxFunEvals = 100; % Set the maximum number of function evaluations (adjust as needed)
    [minimizedRcheck,exitFlag] = fminsearch(@(Rcheck)
abs(((4*3.14159*3.14159*GT/(Rcheck.^2))+2*KGTsum/Rcheck+G)), 10^-8,options);
        result(j,1)=exitFlag;
        Rz(j)=minimizedRcheck;
        if Rz(j)>1
        Rz(j)=0.0010;
        end
         if abs(exitFlag)>0.1
            %Rz(j)=0.00007;%0
            Rz(j)=0.000003;
         end
        R0=Rz(j);
        KGTsum=0;
```

```
%resolving for the initial parameters such as Peclet number to resolve for the KGT function on the next
%cycle
  for n = 1:5
        if V(j)>vd(n)
          k(j,n)=1;
        else
          %k(j,n)= (k0(n)+V(j)/vd(n))/(1+V(j)/vd(n));
           k(j,n)= k0(n).^(1/((1+vd(n)*(A/vd(n))*(V(j)/vd(n)))/(1-(V(j)/vd(n)))));
          %k(j,n)=k0(n)^(1/(1+2.7*V(j)));
       % k(j,n)= k0(n).^(1/(1+V(j)*(A)/(vd(n)-V(j))));
        %k(j,n)=((1-(V(j)^2)/(vdi(n)^2))*(k0(n)+(1+k0(n))*c0(n))+V(j)/vdi(n))/(1-
(V(j)^2)/(vdi(n)^2)+V(j)/vdi(n));
        %k(j,n)=((k0(n)+(1+k0(n))*c0(n))+V(j)/vdi(n))/(1+V(j)/vdi(n));
        end
        Pe(j,n)=R0*V(j)/(2*D(n));
        iv(j,n)=Pe(j,n)*exp(Pe(j,n))*expint(Pe(j,n));
        q=isnan(iv(j,n));
        w=isinf(iv(j,n));
        if q==true || w==true
          iv(j,n)=1;
        end
        if j==1
          c(j,n)=c0(n);
        end
        if j>1
        c(j,n)=c0(n)/(1-(1-k(j,n))*iv(j,n));
```

```
            end
            if V(j)>vd(n)
               mv(j,n)=m0(n)*log(k0(n))/(k0(n)-1);
            else
               mv(j,n)=m0(n)*(1-k(j,n)+((k(j,n)+(1-k(j,n))*mco))*log(k(j,n)/k0(n)))/(1-k0(n));
            end
        ctot(j,n)=c(j,n);
        delT(j,n)=(mv(j,n)*c0(n))/(1-(1-k(j,n))*iv(j,n));
        xi(j,n)=1-2*k(j,n)/((1+(2*3.1415/(Pe(j,n))).^2).^.5-1+2*k(j,n));
        KGTin(j,n)=(Pe(j,n)*mv(j,n)*c(j,n)*(1-k(j,n))*xi(j,n))/(1-((1-k(j,n))*iv(j,n)));
        KGTsum=KGTsum+KGTin(j,n);
        Tsum=Tsum+delT(j,n);
        cL(j,n)=c0(n)/(1-(1-k(j,n))*iv(j,n));
        Ts=Ts+(mv(j,n)*c0(n))/k(j,n);
        Tl=Tl+mv(j,n)*c0(n);
        End
%calculation of solidus and liquidus temperature
        Tsv(j)=Tm+Ts-V(j)/mu;
        Tlv(j)= Tm+Tl-V(j)/mu;
        TipT(j)=Tm+Tsum-2*GT/Rz(j)-V(j)/mu;
        Tsum=0; Ts=0; Tl=0;
        qz=qz+1;
end
qz=0;
R0=Rz(j);
end
```

```
KGTsum=0;



RZZ=Rz';
loglog(V, Rz,'LineWidth',2,'color','g');
xlim([1E-7 100])
ylim([1E-8 1E-2])
%ylim([1820 1930])
%ylim([0 6]); xlim([1E-2 10])
hold on
%loglog(V, Tsv, 'LineWidth',2,'color','b');
%loglog(V, Tlv, 'LineWidth',2,'color','r');
xlabel('Velocity (m/s)');
ylabel('Tip Radius (m)');
hold off
```

A.2 Rosenthal Calculations

```
%S1 110 550    S2 140 750
%S3 150 860 -4mm   S4 150 860
%Ti64 was fit to 11.2, 27, and .48
T0=25;
V=.55; %m/s
alpha=10.2*10^-6; %m2/s (slezak)
z=[1*10^-6 5*10^-6 10*10^-6 25*10^-6 50*10^-6];
```

```
x=linspace(-1E-4,1E-3,1000);%
T=[];Gx=[];Gz=[]; Gavg=[];Vreal=[];CR=[];
P=110;
c=.48; %(Keller for liquid Ti64)
kt=30; %W/mk
beta=[];
time=[];
dtime=[];
for i = 1:length(z)
    for j = 1:length(x)
    R(j,i)=(x(j)^2+z(i)^2)^0.5;
   T(j, i)=T0+((c*P/(2*pi()*kt))*(exp(-1*V*(R(j,i)-x(j))/(2*alpha)))/(R(j,i)));
   %T(j, i)=T0+((c*P/(2*pi()*kt))*(exp(-1*V*(R(j,i))/(2*alpha))*(exp(-
1*V*x(j)/(2*alpha))))/(R(j,i)));
    %T(j,
i)=T0+((c*P/(2*pi()*kt))*(besselk(0,1*V*R(j,i)/(2*alpha),1)*(exp(1*V*x(j)/(2*alpha))))/(R(j,i))
);
    %T(j, i)=T0+((c*P/(2*pi()*kt))*(exp(-1*V*R(j,i)/(2*alpha))*(exp(-
1*V*x(j)/(2*alpha))))/(R(j,i)));
    %T(j, i)=T0+c*P/(2*3.14159*kt*R(j,i))*exp((-1*V*(R(j,i)-x(j))/2*alpha));
    %T(j, i)=T0+((c*P/(2*pi()*kt*R(j,i)))*exp(-1*V*(R(j,i)+x(j))/(2*alpha)));
```

```
    Gx(j,i)=(1+(x(j)/(R(j,i)))+2*alpha*x(j)/(V*(x(j)^2+z(i)^2)))*((-
1*c*P*V/(4*pi()*kt*alpha))*1/(R(j,i)))*exp((-1*V/(2*alpha))*(x(j)+R(j,i)));
    Gz(j,i)=(1+2*alpha/(V*R(j,i)))*((-1*c*P*V/(4*pi()*kt*alpha))*z(i)/(x(j)^2+z(i)^2))*exp((-
1*V/(2*alpha))*(x(j)+(R(j,i))));
    Gavg(j,i)=(Gx(j,i)^2+Gz(j,i)^2)^0.5;
    %dtime(j,i)=
(1+x(j)/R(j,i)+2*alpha*x(j)/(V*(x(j)^2+z(i)^2)))*((c*P*V^2)/(2*3.14159*kt*2*alpha*R(j,i)))*e
xp(-1*V/(2*alpha)*(x(j)+R(j,i)));
    beta=atan(Gz(j,i)/Gx(j,i));
    Vreal(j,i)=V*cos(beta);
    CR(j,i)=Gavg(j,i)*Vreal(j,i);
    time(j)=(x(j)-0)/V;
    end
end
    k=0;
    for k = 1:(length(T)-1)
    dtime(k)=(T(k+1,4)-T(k,4))/abs(time(k)-time(k+1));
    end
semilogy(x, T)
%lim([0 0.001]);
%xlim([600 2400])
```

APPENDIX B

OBSERVATIONS ON SPLAT QUENCHING

B.1 Necessary Background on Splat Quenching

This appendix is intended as a summary of the necessary fundamentals to understand the splat quenching technique in terms of literature and immediately applicable concepts that were not previously introduced in the dissertation. Splat quenching as a general term is a range of techniques that can generally be outlined as a molten droplet of material coming into contact with a substrate at an elevated velocity. This can be the form of twin hammer splat quenching such as what was used extensively in this dissertation where the substrates are fired at the droplet. There also techniques such as thermal spray or Duwez gun that fire molten droplets at stationary substrates. The benefit of twin hammer splat quenching is the higher momentum of the substrate pistons and the dual-sided nature of the collision. To generate the equivalent pressure in a melt driven collision the velocity has to be much larger and does not demonstrate the same benefits in terms of cooling rate such as in twin hammer splat quenching. The melt driven collision techniques are easily repeatable as droplets from a melt can be continuously dropped and accelerated resulting in thermal spray being used as a manufacturing technique. However, the twin hammer splat quenching technique is limited to one sample prior to needing to be reloaded, so the higher cooling rates come at the cost of being relegated to a research tool.

One of the first attempts to understand the cooling rates in a splat quench technique was in 1967 from R. Ruhl [1]. The approach was simple looking at splat quenching as a static processing without coupling the fluid flow. This approach was mimicked for use in Chapter 2 of

this dissertation. The immediate result of this study is that the use of a Biot number positions splat quenching in a difficult to immediately cooling where the assumptions of thermal gradient vs interface controlled cooling breakdown. This means that splat quenching thermal modeling would require the use of a numerical modeling such as the FLUENT simulations done in throughout this dissertation. The Biot number is laid out as the product of the half splat thickness and heat transfer coefficient divided by the thermal conductivity of the melt. The change as a function of heat transfer coefficient (h) and splat thickness can be seen in Figure X.X. To be interracially controlled heating a low h value and low splat thickness are required as can be seen where the zirconia substrate sample in Chapter 2, where the lower thickness and h value resulted in a fundamental shift in the solidification structure from the metallic substrate samples. The reverse is also true where ideal cooling that is limited by the thermal conductivity develops higher thermal gradients in the melt and would need high h value and thickness to develop the gradient needed.

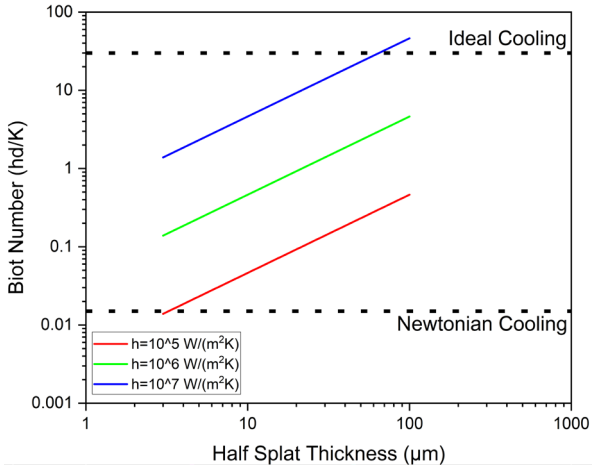

Figure B.1 Plotted graph of the calculated Biot number for a splat quench sample of Ti-5553 as a function of half splat thickness and heat transfer coefficient with labels for the regions of ideal and Newtonian cooling laid out according to Ruhl [1].

More complicated modeling attempts have also been conducted on the splat quenching technique such as by Miyazawa et al. in 1979 [2] that couple the deformation of the liquid into the model. These higher quality models attempt to predict splat thickness, contact pressure, and radial distribution of cooling. This approach is more robust than the previous static model that focused on the heat transfer only while also being much more complicated in terms of the intricate nature between material properties, fluid deformation, and interaction with the substrates. This model does directly predict a higher cooling rate in the edge of the splat quenched foil versus the center that was seen experimentally in Chapter 2. The model also captures the trend of velocity being a factor in the thickness of the splat quenched foil with the thickness varying significantly in the 2-5 m/s range while the variation in the 5-10 m/s range is much lower.

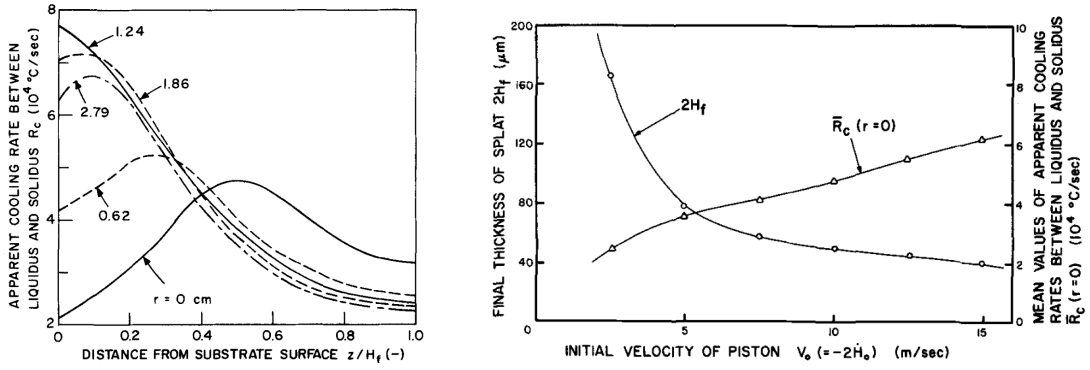

Figure B.2 Plots from Miyazawa et al. [2] that highlight the effect of (a) radial position on estimated cooling rate and (b) velocity on splat thickness.

In the models discussed, the heat transfer coefficient is the most difficult to parameter to estimate due to the connection between substrate interaction, fluid flow, and heat transfer. The model developed by Xue et al. [3] for thermal spray was used in Chapter 2 to provide both an estimate as well as provide relationships between the splat quench parameters and resulting thermal changes. While parameters such as contact pressure and thermal conductivity were seen

to be fairly accurate, the variation of surface roughness was difficult to investigate for several reasons that were not fully elaborated upon in Chapter 2. The first is that at higher substrate roughness there was found to be deformation to the substrate and melting of the copper asperities due to the splatting event. This serves as a limiting factor to the expected roughness due to the effective smoothing of the substrate. However, the largest variation was the presence of flow features that did not conform to the substrate. The flow lines have clear areas that are not in contact with the substrate likely due to argon gas being forces into these crevices as the droplet in being flattened. This complicates any immediate calculation of the surface roughness as now there are both flow based roughness that were seen to form more readily on a higher polished substrate as well as the roughness typical of the surface asperities. For this current dissertation, a value of asperity size of 1 μm was widely used and provided results that correlated well with literature estimations and empirical cooling rate models used on the SS316 cell spacing.

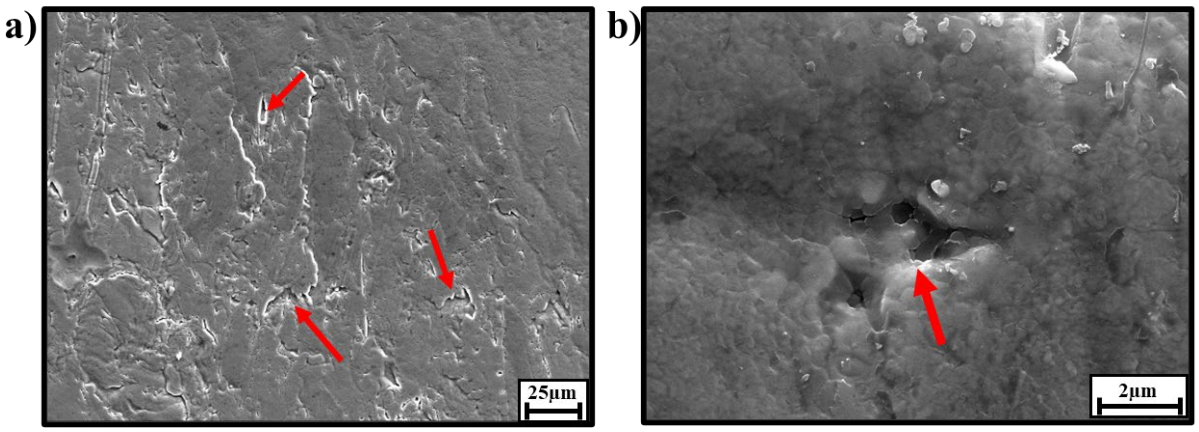

Figure B.3 SEM imaging of the surface of a splat quenched sample highlighting (a) the lack of uniformity in surface due to the flow behavior and (b) a higher magnification image of one of the valleys in the surface highlighting the material not coming into contact with the copper substrate

B.2 Alloy Selection for Splat Quenching

Through observation while testing a collection of alloys ranging from materials such as titanium, aluminum, steels, and even incomes alloys, there are several factors that make alloys easier or harder to splat quench than others. The first is the magnetic response of the alloy. The second is the size of the gap between the liquidus and solidus of the alloy. The final is density of the material. These properties couple with the inductive heating and levitation in interesting ways that will be qualitatively outlined with observations on why certain alloys are difficult to process while others are fairly easy to work with.

The magnetic response of the alloy is a key feature when investigating the ability to easily splat quench an alloy due to the levitation and heating being coupled together. If an alloy has sharp transitions in magnetic response such as a ferritic steel that transforms to austenite during heating the initial stability of the material can be compromised that requires manipulation of the current in or frequency to keep the sample levitating. For the current setup, the frequency applied to the coil is constant with the current being fluctuated and as such the user control is simplified at the cost of less total control of the operating conditions. The power absorbed as heat is related to the electrical resistivity and the surface area of the sample due to the eddy current generated largely in the skin depth of the material. The levitation is a function of both the electrical conductivity and the permeability meaning that an alloy like nickel with a higher permeability and lower conductivity than aluminum is much more stable during splat quenching.

An interesting but important observation is the sensitivity to freezing interval of an alloy and the ease of melting in the levitation coil. Due to the heating being limited to a thin skin depth of sample, a larger range of solid-liquid coexistence alloys for material away from the near

surface to melt and develop a convective flow that quickly spreads the heat throughout the sample. Pure elements can quite often form a thin layer of liquid on the surface that requires +100°C overheat prior to the bulk of the metal beginning to melt. For an alloys such as Inconel 718, the material easily melts at the melting temperature. This has a larger impact than purely on superheat needed to fully melt as the sudden transition from solid to liquid in the pure metal one melting begins has caused numerous issues with levitating stability as the shape change can be quite sudden. On the other hand, the smoother transition of an large freezing range alloy results in a more gradual and controlled transition that leads to a higher success rate of successful levitation than alloys such Ti-Mo binary that have a 10°C freezing range.

The final observation is merely to point out that the density of the material also plays a part in the amount of material that is needed for successful levitation if all other values are held constant. The amount of material in a sample to get the surface area needed for adequate heating has to be balanced by the force generated to levitate the sample that is a function of volume. As such the most stable sample size can fluctuate based on density, conductivity, and permeability of the material and may need to be dialed in either by calculation or experimental observation. With these three points made, the author does want to relay that materials such as pure aluminum that can still be processed but the difficulty is increased in comparison to other alloys.

B.3 Sample Creation

This section will outline the sample preparation and techniques used for creation of the splat quench samples for this dissertation. The initial step was feedstock preparation, and this came in the form of pre-alloyed material such as commercially available plate as well as arc melted buttons that were created by melting of pure elemental feedstock. The material in either

form was then machined into cubes on the order of 4-5 mm per side. The cubes were then cleaned and were then subsequently prepared for splat quenching.

The preparation of the feedstock is simple for a commercial alloy that can be purchased in a preprocessed for as it is ready for machining, however the arc melting of alloys is worth highlighting. The arc melting was done on in a chamber on water cooled copper hearth that was backfilled with argon after pumping down with a rotary pump three times. This provides a necessary oxygen-lean atmosphere to decrease interstitial contamination. The ultra-high purity argon is continued to flow during the melting process with the chamber pressure being held above atmosphere. Prior to each round of melting, a pure titanium getter (~5 g) was melted to lower the oxygen content even lower. The best approach was found to melt the higher melting temperature (molybdenum in the Ti-5553 alloy) elements together with the dominant element (titanium) in small batches to ensure dilution, necessary heating to melt, and lowering of melting temperature. The buttons made for Ti-5553 were generally 15-20 grams and the observation was that if the Ti-Mo was melted in one large button that the vast separation in melting temperatures resulted in molybdenum not melting or entering solution. Therefore, the creation of several smaller buttons was preferred to ensure full mixing of the higher temperature alloys. The smaller Ti-Mo buttons could then be combined with the other more sensitive solutes such as Cr and Al to create the final button. The buttons were flipped four times and remelted to increase the confidence of full melting and micing of the solute all while held under flowing ultra-high purity argon. This was found to be enough to ensure that the interstitial content was below ELI standards.

Following creation of the feedstock, the samples were cut using an EDM (electrical discharge machining). Slits 5mm wide were cut into the button prior to rotated 90° and the cuts

were repeated. This action resulted in a series of square cross sections cut into the button that could then be sliced into cubes for use in splat quenching or for specimen characterization. However, the ease of the EDM does have a drawback of creating a recast layer that did require surface preparation to ensure a clean sample. A belt sander was used to remove the recast layer off of each side, and the recast layer was easily removed. The sample was then cleaned with isopropyl alcohol and dried with air. The final shape is not critical for splat quenching, but the more symmetric the shape the higher the levitation stability during splat quenching.

The splat quenching process is of relative ease practically described here with the vacuum practice highlighted in Appendix C. Once at a desired atmosphere (0.6 atm of ultra-high purity argon) the sample is position on the alumina manipulator in the center of the induction coil. The sample is levitated and then the manipulator can be removed so the machine can be armed for the sample preparation. The sample should be placed around the midpoint of the coil; however, it is preferred to be higher in the coil than lower due to the ability for the cube to jump and become unstable if placed below the equilibrium levitation point. The placement of the coil is paramount to a successful splat quench as angular misorientation can cause the molten droplet to clip the coil itself or to miss the laser trip wire. Additionally, misalignment of the coil, unsymmetric sample geometry, or wobbling introduced by specimen placement in the coil all result in general stability issues with the melt having erratic movements that are hard to reduce. An aligned coil with a stable sample will resultingly have a high chance of splatting successfully and is therefore what should be desired though some alloys have higher stability than others.

References

[1] R.C. Ruhl, Cooling rates in splat cooling, Mater. Sci. Eng. 1 (1967) 313–320. https://doi.org/10.1016/0025-5416(67)90013-4.

[2] K. Miyazawa, J. Szekely, A mathematical model of the splat cooling process using the piston and anvil technique, Metall. Trans. B. 10 (1979) 349–358. https://doi.org/10.1007/BF02652505.

[3] M. Xue, Y. Heichal, S. Chandra, J. Mostaghimi, Modeling the impact of a molten metal droplet on a solid surface using variable interfacial thermal contact resistance, J. Mater. Sci. 42 (2007) 9–18. https://doi.org/10.1007/s10853-006-1129-x.

APPENDIX C

PRELIMINARY TITANIUM SPLAT QUENCH RESULTS

C.1 Cleanliness of Alloys

The cleanliness of titanium is a high priority both in industry as well as research. As such, the ability to arc melt and splat alloys without exceeding cleanliness standards was needed to be established. Cp Ti (grade 2) and Ti-6Al-4V feedstock was saw cut from 2.5mm thick plate. The Ti-5553 feedstock was cut from laser powder bed fusion samples provided by KCN-Honeywell. The 0.8 grams of feedstock material was cut into cube shape and sanded on all sides to remove burrs and roughness from the machining processes. Prior to insertion into the splat quencher, schematically shown in Figure C.1, the feedstock cubes were cleaned with isopropyl alcohol. Once in the splat quencher, the chamber was pumped down to $2.5x10^{-4}$ mbar prior to being backfilled with argon three times. The specimen are then magnetically levitated and inductively heated with the temperature measured by an overhead pyrometer until melted. The molten specimen is then dropped and interrupts a beam triggering copper platens to be electromagnetically shot towards the material resulting in compression of the material between the platens. For all three materials, inert gas analysis (IGA) was conducted on the feedstock and subsequent splat to quantify the interstitial element pickup from the process. The IGA process (ISO 22963:2008) is an impulse furnace technique that involves evaporation of the material in a graphite crucible. Any gas generated are released into a flowing inert gas stream with sensors to analyze the infrared profile to measure oxygen and thermal conductivity for measuring nitrogen and hydrogen. As the effect of oxygen and other interstitials are not clearly demarcated at low

wt%, the use of standards for Cp-Ti and Ti-64 were used as a gage of purity with Ti-6Al-4V extra low interstitial and Cp-Ti grade 4 used as metrics of resulting cleanliness for all splats.

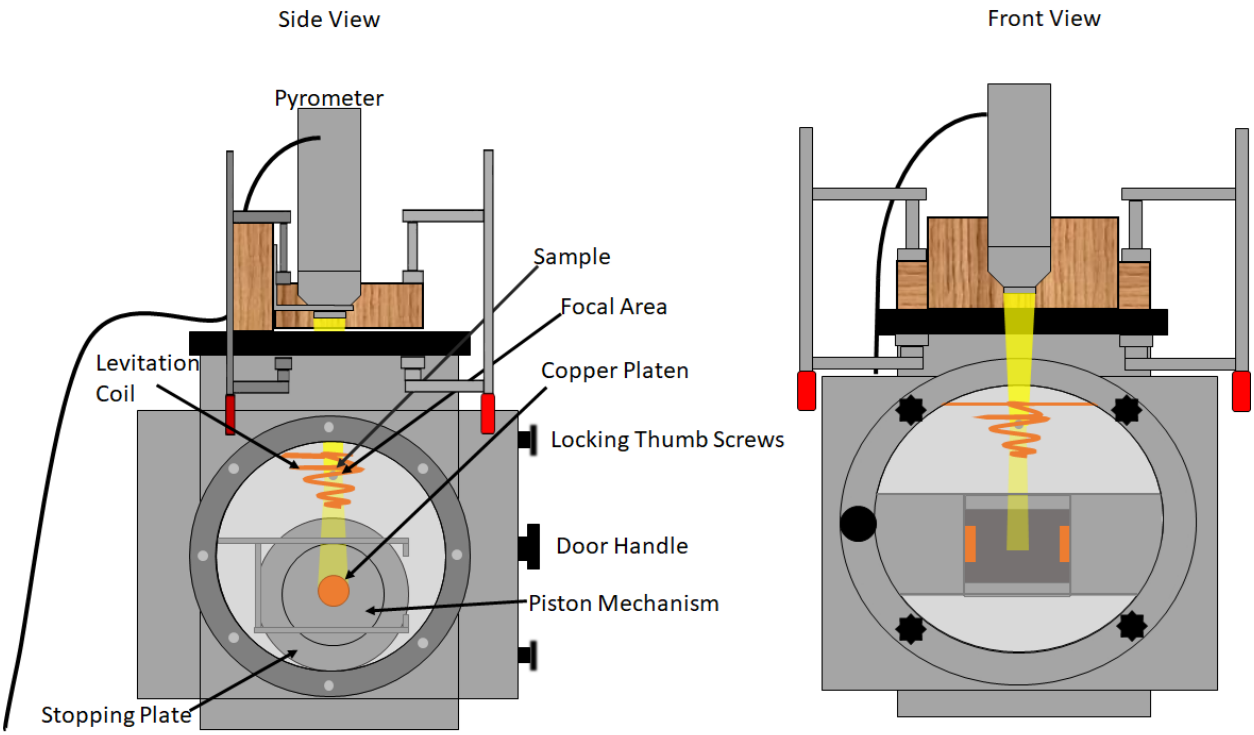

Figure C.1. Schematic of two-piston splat quenching chamber setup.

For all three commercial alloys tested, successful splats were able to be created. As demonstrated by this task, splat quenching of titanium is possible for numerous commercial alloys and has applicability to further study of the rapid solidification rate on titanium microstructure. IGA results for oxygen and nitrogen are shown in Figure C.2 with the limits for Ti-6Al-4V ELI (extra low interstitials) from ASTM F136 and CP Ti Grade 1 from ASTM B265 shown as references. As can be seen in the oxygen data, the Ti-6Al-4V and Ti5553 feedstock material already exceeded the Ti-6AL-4V ELI oxygen standard. In addition, the Ti5553 LBPF feedstock was also borderline the ELI spec for nitrogen content as well. The CP Ti feedstock has the lowest interstitial oxygen content and similar to the Ti-6Al-4V feedstock was well below the nitrogen standard. For the splats the average oxygen uptake from the SQ process was 0.04 wt%

for the Cp Ti and Ti-6Al-4V with the Ti5553 having a minor increase in oxygen with a 0.05wt% pickup. This increase pushed the CP Ti material over the Ti-6Al-4V ELI oxygen standard and the nitrogen pickup pushing the Ti5553 splat material over the standard as well. The IGA data demonstrates that the SQ process does result in a measurable increase in interstitial elements and that the quality of the initial feedstock needs to be high enough to ensure that the final oxygen level is below the desired cleanliness standards.

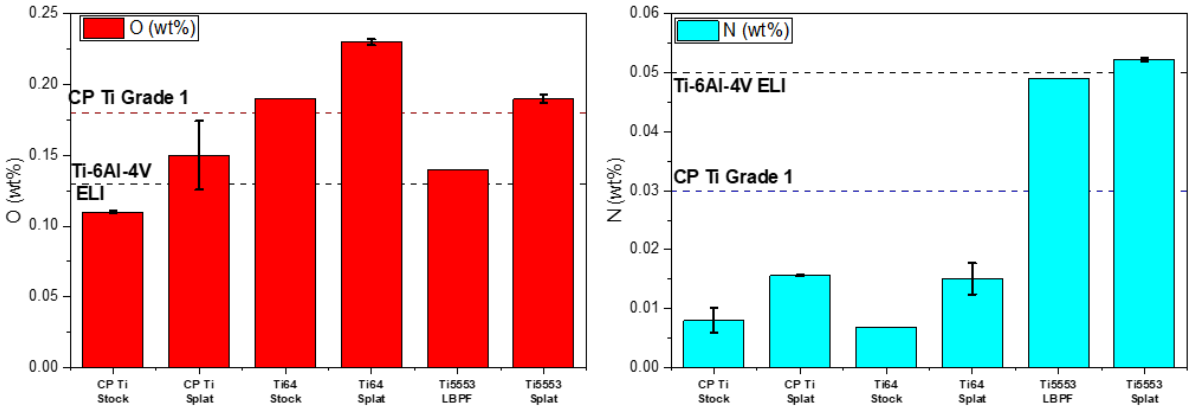

Figure C.2 (a) Oxygen and (b) Nitrogen weight percent values for the feedstock and splats tested by inert gas analysis. For comparison, ASTM F136 and ASTM B265 values for Ti-6Al-4V ELI and CP Ti Grade 1 respectively are presented as cleanliness comparison.

C.2 Ti-Mo Binary Alloy Study

Subsequently, three binary Ti-Mo alloys were created to evaluate the ability to manufacture titanium alloys of the cleanliness and repeatability necessary for further research. Pure elemental feedstock (Kurt J. Lesker) was obtained in pellet form for titanium and in powder form for molybdenum. The powdered molybdenum was pressed into a disk prior to arc melting to eliminate the potential for powder blow off due to the arc. The amounts of each were measured out to create three alloys of molybdenum weight percent of 5.4, 9.6, and 12%. The weighed

composition was then arc melted following three argon backfills in a water chilled copper crucible. The first set of buttons were rolled to a set thickness to allow for easier saw cutting into metallurgical specimen. Subsequently, the rolling process resulted in significant cracking in the Ti-5.4Mo and Ti-12Mo alloys that still allowed for specimen preparation. In contrast, the Ti-9.6Mo completely shattered even upon remelting and rolling at smaller increments. When creating a second batch of the alloy compositions for use in examining repeatability, the alloys were kept in their arc melted buttons and subsequently electrical discharge machined (EDM) into cubes allowing for the dimensions needed without cracking and failure of the feedstock material. Representative microstructural specimen were cut and polished to .05 μm for each binary feedstock to perform quantitative energy dispersive spectroscopy (QEDS) to evaluate the composition. The QEDS was performed on a JEOL 7000 SEM with an Oxford X-Max 80mm^2 EDS detector and analyzed with DTSAII to get quantitative composition measurements using pure elemental standards. Process time and scan time were both changed to try and optimize the scans to increase the counts and sharpen the peak shape needed to properly quantify the phases. Process time 4 and a five-minute scan were found to offer an acceptable number of counts and peak definition for the Mo Lα line that was used for quantification as they represented the best compromise between counts and time and with the process time created an optimum dead time of ~20%. In addition to QEDS, currently inductively coupled plasma (ICP) mass spectrometry is currently being conducted to have accurate composition data as well as evaluate the quality of the QEDS data.

To understand the phases present after arc melting of the binaries, x-ray diffraction (XRD) with a Philips X'Pert MPD using Cu Kα with 45kV and 40mA operating conditions. Five scans were repeated with over a 5° omega wobble. Post scan analysis and Rietveld refinement was

conducted using the HighScore Plus commercial software to match the phases present in the arc melted material as well as get lattice parameter information.

The Ti-Mo feedstock cubes were splat quenched following the same procedure as the commercially available material from Task 1 with the drop temperature estimated from Ti-Mo binary phase diagrams generated in ThermoCalc, displayed in Figure C.3 The splats were also analyzed for phase content using the same XRD configuration as described in Task 2. Electron back scatter diffraction (EBSD) was conducted on diameterly cut and polished splats to analyze the morphology and location the grains and phases present. EBSD scans were taken using a JEOL 7000 SEM, phosphor screen EBSD camera, and the Aztec software to process the collected Kikuchi patterns. Figure C.4 demonstrates the location where the EBSD maps were generally taken for a splat. While the EBSD technique is unable to properly resolve the athermal ω phase due to its small scale, the ability to evaluate the larger structures such ß grains and martensitic α" are highly valuable for microstructure characterization. Due to the unique nature of the orthorhombic α" lattice parameters changing to morph between HCP and BCC with different composition, the lattice parameters from the Rietveld refinement were used to create phases α" for the Ti-5.4Mo and Ti-9.6Mo.

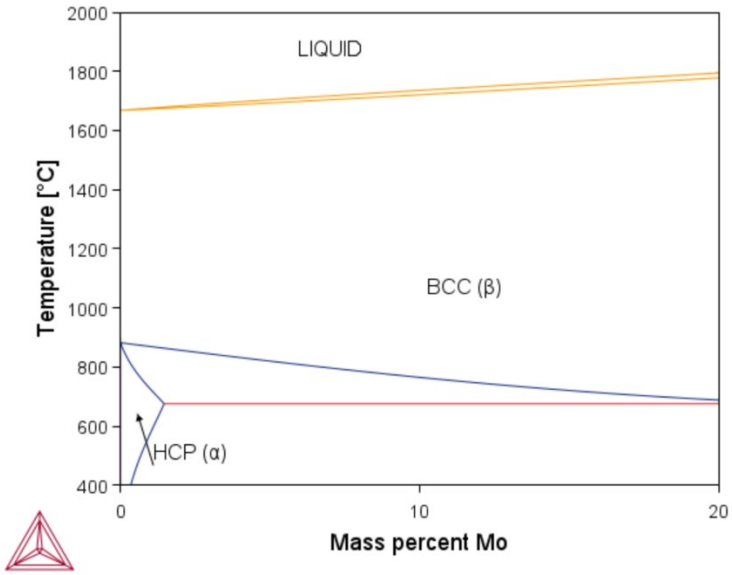

Figure C.3 Ti-Mo phase diagram generated in ThermoCalc.

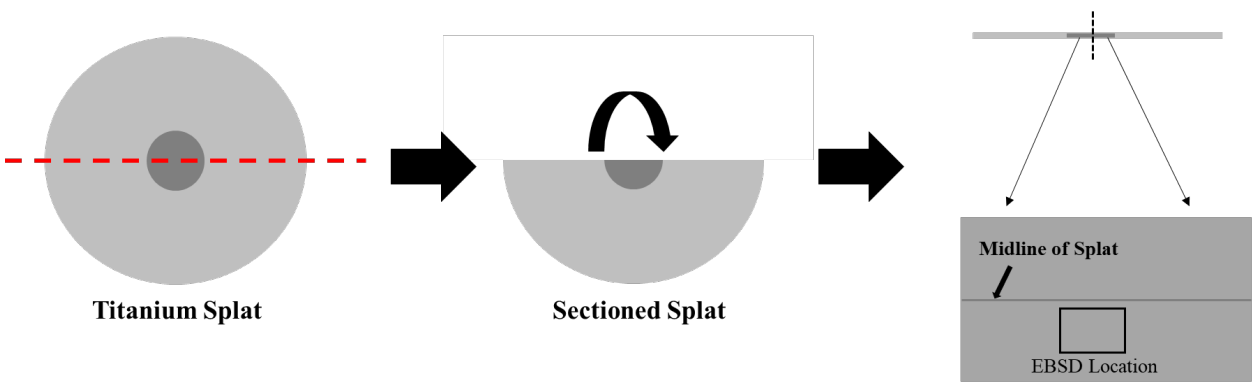

Figure C.4 A generalized representation of EBSD map locations taken for phase identification for the splats

Table C.1 QEDS quants for the three Ti-Mo binaries at multiple scan lengths

FS Specimen	Time	Ti (wt%)	Ti Stdev (wt%)	Mo (wt%)	Mo Stdev (wt%)	Sum (wt%)
Ti-5.4Mo-1	2 min	96.11	0.190	4.89	0.034	100.99
	5 min	95.80	0.073	4.89	0.022	100.69
Ti-9.6Mo-1	1 min	89.71	0.195	9.25	0.058	98.96
	2 min	89.52	0.268	9.26	0.066	98.78
	5 min	91.14	0.070	9.34	0.004	100.47
Ti-12Mo-1	1 min	88.49	0.059	11.51	0.054	101.07
	2 min	88.50	0.077	11.49	0.077	101.01
	5 min	88.37	0.210	11.62	0.210	101.13

The XRD scans for the binary feedstocks are presented in Figure C.5 with the phases and lattice parameters presented in Table 4. The unrolled feedstock Ti-5.4Mo and Ti-12Mo both were found to have a β+ω microstructure. The unrolled Ti-9.6Mo feedstock has an β +α"+ ω microstructure. This difference in the Ti-9.6Mo and the other binaries is potentially due to differences in cooling rate during arc melting as the Ti-9.6Mo was melted into a cigar shaped crucible with a smaller radius to allow for easier machining into cubes on the EDM. In the XRD of the rolled feedstocks, the Ti-5.4Mo and Ti-9.6Mo were determined to have β +α" while the Ti-12Mo retained its β+ω phase composition. This difference in the phases present in the rolled Ti-5.4Mo compared to unrolled is likely due to stress-induced martensite that occurred during the rolling processes.

Table C.2 Identified phases and lattice parameters for arc melted Ti-Mo binary alloys

		Lattice Parameters (Å)					
		β	α"			ω	
Alloy	Phases	a	a	b	c	a	c
Ti-5.4Mo	β+ω	3.261				4.608	2.818
Ti-9.6Mo	β+α"	3.272	3.12	4.773	4.639		
Ti-12Mo	β+ω	3.250				4.631	2.828

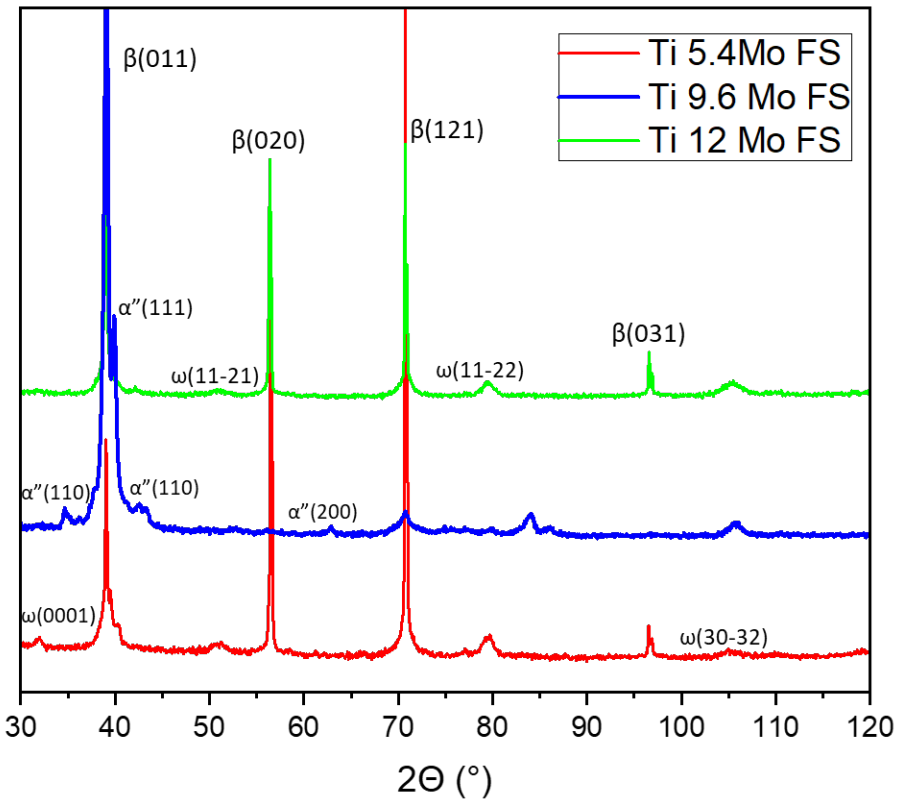

Figure C.5 XRD scans for the three unrolled binary Ti-Mo arc melted buttons. The Ti-12Mo and Ti-5.4Mo revealed identical phases present (β+ω) for the two composition, while the Ti-9.6Mo contained the orthorhombic martensitic (α") phase likely due to differences in cooling rate during the arc melting process.

IGA analysis of the splats for all three Ti-Mo binaries can be seen in Figure C.6 The average oxygen pickup was found to be .031 wt% oxygen with no splats exceeding the cleanliness standards. Nitrogen pickup had similar results that provide evidence that the UA arc melted samples and splat quenching can provide a low interstitial material for material characterization.

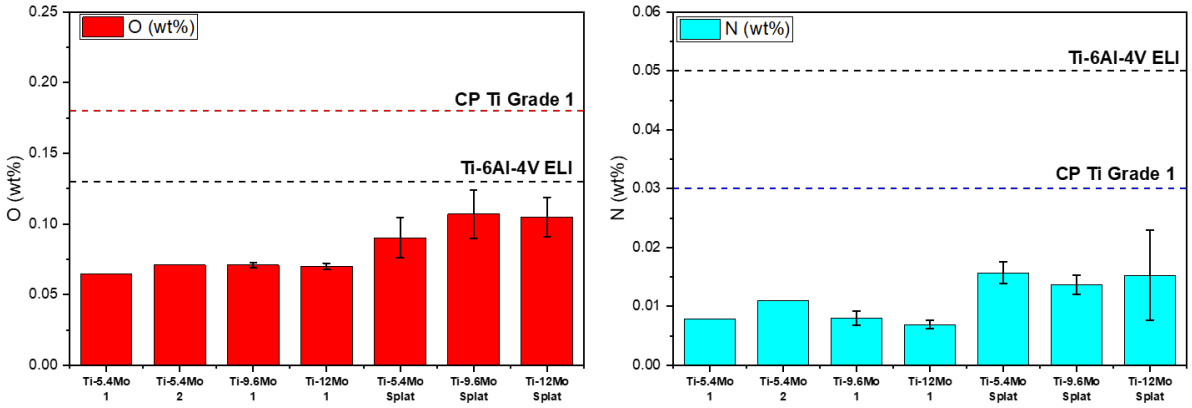

Figure C.6 IGA results comparing the UA arc melted samples with their post-splat quenched counter parts. Both the oxygen and nitrogen levels are below the Ti-6Al-4V ELI and Grade 1 CP Ti standards.

Comparison between the XRD spectra for the splat quenched Ti-Mo binaries with their arc melted counterparts exhibited a difference in phases present and as well as differences in lattice parameters for the orthorhombic α". The phases present and the associated lattice parameters are displayed in Table 5. The Ti-5.4Mo, Figure C.7a, was found to be fully martensitic due to the higher cooling rate imposed during splat quenching. Figure C.7b displays the XRD spectra for SQ and FS Ti-9.6Mo with both exhibiting α", while the feedstock also retained some β. The Ti-12Mo in Figure C.7c was found to have the same phases in both the arc melted button and splat quenched sample though the peak profile demonstrates some differences.

Table C.3 Phases and associated lattice parameters identified with XRD

			Lattice Parameters (Å)						
			β	α"			ω		
Conditon	Alloy	Phases	a	a	b	c	a	c	Notes
Feedstock	Ti-5.4Mo	β+ω	3.261				4.608	2.818	Change in arc melt hearth resulting in different cooling rate may be responsible for α" in Ti-9.6Mo
	Ti-9.6Mo	β+α"	3.272	3.12	4.773	4.639			
	Ti-12Mo	β+ω	3.250				4.631	2.828	
Splat Quenched Samples	Ti-5.4Mo	α"		2.965	5.097	4.678			
	Ti-9.6Mo	α"		3.019	4.954	4.628			
	Ti-12Mo	β+ω	3.263				4.598	2.822	

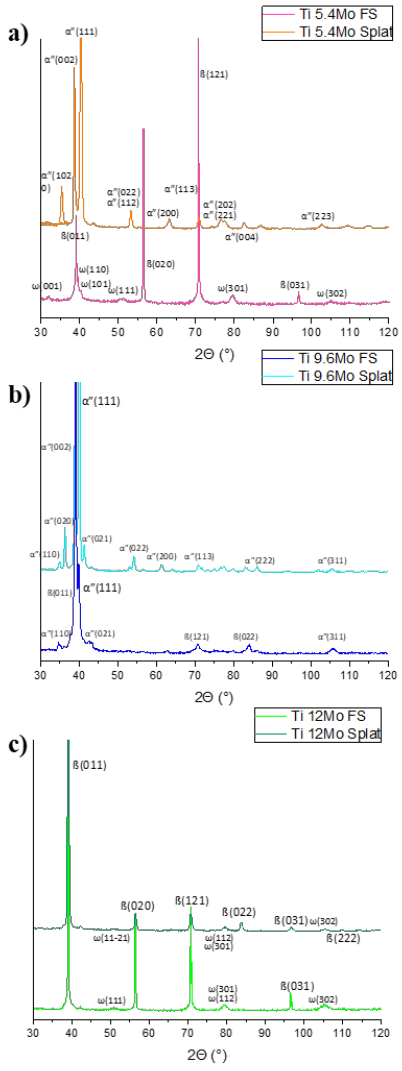

Figure C.7 XRD plots for the arc melted and splat quenched specimen for the Ti-5.4Mo (a), Ti-9.6Mo (b), and Ti-12Mo (c). Each spectra has several key peaks highlighted with the phase and plane.

Comparison can be made with the lattice parameters produced by the rapid solidification/cooling rate from splat quenching to water quenched samples from literature to attempt to understand if the processing route used for this study results in significant structural changes. Plotting the lattice parameters as a function of molybdenum content, shown in Figure C.8a and b, demonstrated overlap with literature data for both α" and omega seen in the splat quenched samples. The α" found in the Ti-9.6Mo arc melted sample does not match the literature data for that given composition potentially due to the slower cooling rates allowing for diffusion. Additionally, the arc melted sample exhibited both α" and the beta phase while the splat quenched samples were entirely α". Figure C.8c is a plot of b/a and c/for α" further establishing the relationship between the RS produced phase and literature data as well as demonstrating the gradual shape change between the α" and HCP phase (highlighted by red lines). This plot demonstrates the subtle changes in lattice parameters seen at Ti-5.4Mo with only a small distortion occurring between it and the HCP martensite.

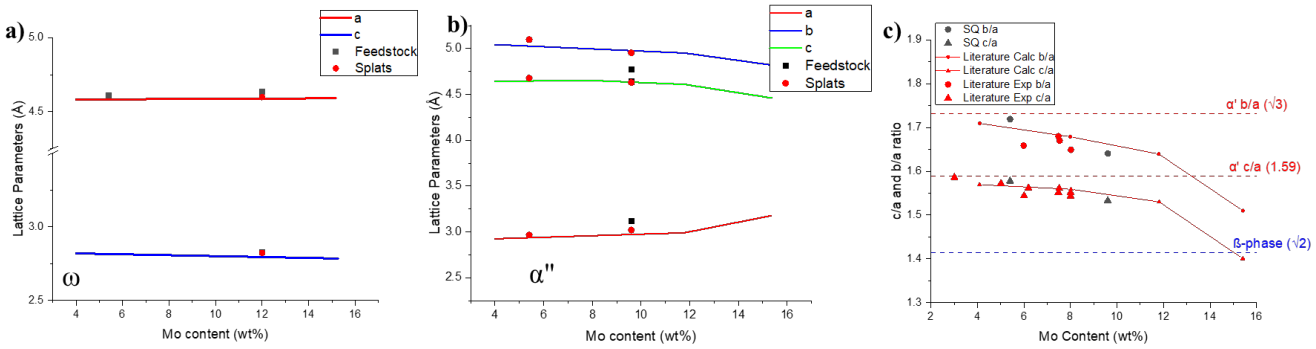

Figure C.8 Lattice parameters verses molybdenum content for both omega (a) and α" (b) compared to literature data. Additionally c/a and b/a ratios demonstrating the gradual change from in shape from HCP up to over 12% molybdenum [1].

Figure C.9 is the EBSD IPF maps of the three Ti-Mo binary splat quenched samples. The 5.4 wt% Mo appears a typical titanium martensitic structure that with no detectable BCC parent phase retained. The 9.6wt% Mo however demonstrates significantly different lathe structure with significant retention of the BCC parent phase. The 12wt% Mo alloy demonstrates a fully BCC structure with the omega phase detected in XRD too small to be discerned by EBSD.

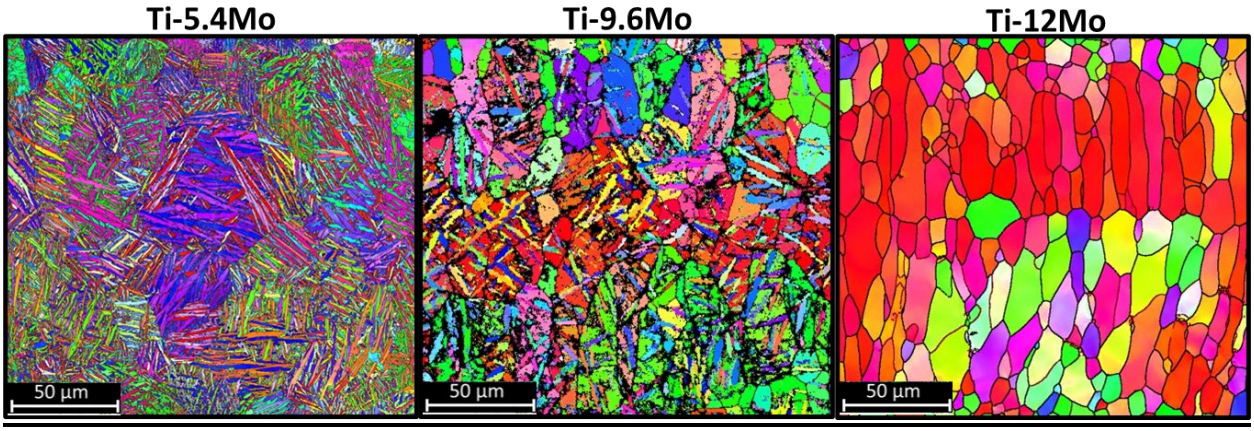

Figure C.9 EBSD IPF maps of Ti-Mo binaries (a) 5.4 Mo, (b) 9.6 Mo, and (c) 12 Mo.

In summary, this work demonstrates the ability to adapt the splat quench technique for titanium alloys as well as maintaining the cleanliness needed to minimize the interaction of oxygen on the microstructural development during splat quenching. XRD and EBSD have been used to establish the crystallography of phases present in the as-splatted and arc melted materials as well as the grain structure resulting from the SQ process. Rietveld refinement showed that the splat quenching did not considerably alter the lattice parameters of the phases identified compared to literature quenched values but did change the phases formed for the Ti-5.4Mo and Ti-9.6Mo compositions as compared to the arc melted feedstock. The techniques developed in processing and characterizing the splats can be further refined and used for further research into the effect of more complex solute additions as well as begin to correlate microstructure and cooling rate information.

References

[1] M. Li, X. Min, K. Yao, F. Ye, Novel insight into the formation of α″-martensite and ω-phase with cluster structure in metastable Ti-Mo alloys, Acta Mater. 164 (2019) 322–333. https://doi.org/10.1016/J.ACTAMAT.2018.10.048.